Optical properties of Ba122 iron-based superconductors

Yaomin Dai

THÈSE DE DOCTORAT CONJOINT ENTRE L'UNIVERSITÉ PIERRE ET MARIE CURIE ET IOP CAS

Spécialité: Physique de la matière condensée

Présentée par

Yaomin DAI

Pour obtenir le titre de docteur de l'Université Pierre et Marie Curie et IOP CAS

Sujet:

Étude des propriétés optiques du système supraconducteur Ba122 à base de fer par spectroscopie infrarouge

Rapporteurs:

Florence RULLIER-ALBENQUE	IRAMIS, CEA-Saclay
Xincheng XIE	Pékin Université

Soutenue le 8 décembre 2011 devant le jury composé de:

Pengcheng DAI	IOP, CAS, Pékin	Examinateur
Shiping FENG	Pékin Normal Université	Examinateur
Andrea GAUZZI	IMPMC, UPMC, Paris	Examinateur
Ricardo LOBO	LPEM, ESPCI, Paris	Directeur de thèse
Xianggang QIU	IOP, CAS, Pékin	Directeur de thèse
Dirk VAN DER MAREL	Université de Genève	Examinateur
Haihu WEN	Nanjing Université	Examinateur
Xincheng XIE	Pékin Université	Examinateur

Acknowledgements

The work presented in this thesis represents a collaborative scientific research between LPEM, Ecole Supérieure de Physique et de Chimie Industrielles de la ville de Paris, Université Pierre et Marie Curie, Paris, France and The Institute of Physics, Chinese Academy of Sciences, Beijing, China.

First and foremost I am deeply indebted to my advisors Prof. Ricardo Lobo (Paris, France) and Prof. Xianggang Qiu (Beijing, China). All the data in this thesis were collected in Paris with the help of Ricardo. He is very proficient in taming the spectrometers. Every time when the spectrometers in our lab are on strike, he can always get it back to work for me. Ricardo helped me to build the whole low temperature reflectivity measurement system for the ABB Bomen DA8 spectrometer in IOP, CAS, including the temperature controlling system, mechanical parts and the optics. He also gave me many opportunities to attend international conferences, taught me how to write a scientific paper, how to give a good presentation and guided me to write the thesis. He likes discussing with students and has infinite patience. He also has a keen scientific wit and a good sense of humor which made me spend a high quality and very interesting scientific research time in LPEM, ESPCI. Prof. Xianggang Qiu gave me lots of free and open space in scientific research. He always encourages me to play with the instruments as much as possible and provides everything I need in scientific research. He put great trust in me and gave me the opportunity to build a low temperature reflectivity measurement system in IOP, CAS, in Beijing. He also encourages me to talk with scientists from different fields, so I can always get innovative ideas. Prof. Xianggang Qiu's extensive scientific interests, kind mentoring and positive encouragement guided my research during my Ph.D study. Under the tutelage of Prof. Ricardo Lobo and Prof. Xianggang Qiu, I have grown as a real scientist and as a person.

The high-quality $Ba(Fe_{1-x}Co_x)_2As_2$ single crystals studied in this thesis were grown by A. Forget and D. Colson in IRAMIS, SPEC, CEA. and $Ba_{1-x}K_xFe_2As_2$

single crystals were grown by Bing Shen, Peng Cheng and Hui-Qian Luo in Hai-Hu Wen's group in IOP, CAS and Nanjing University. I gratefully acknowledge them for such clean, large and shinning single crystals. I also thank Pierre Toulemonde, Pengchang Dai, Changqing Jin and Chenglin Zhang for providing us high-quality samples. I thank Hai-Hu Wen for plentiful instructive suggestions. I also thank J. P. Carbotte and T. Timusk for helpful discussions.

I wish to thank Florence Rullier-Albenque and Xincheng Xie for writing the report for my thesis and giving many useful suggestions. Thank Pengcheng Dai, Shiping Feng, Andrea Gauzzi, Shiliang Li, Dirk Van der Marel, Haihu Wen, Tao Xiang, and Xincheng Xie for attending my thesis defence as members of the committee.

I would like to thank Philippe Monod, Arlette Trokiner, Xiangzhen Xu, Andrés Santander, Alexandre Zimmers, Benoît Fauqué and Renaud Schleck for teaching me French and their kind help during my stay in Paris. I wish to thank Alain Sacuto for the Condensed Matter Physics course, from which I learnt a lot. Thank Brigitte Leridon for teaching me how to use the PPMS. I also thank Ludovic Olanier for helping me with machine work. I express my thanks to the secretaries of LPEM Marie-Claude Theme, Josiane Racine, Sophie Demonchaux and Carole Grangier, they offered all kinds of help to make my Lab-life much easier. I wish to thank Kamran Behnia, Jerome Lesueur, Herve Aubin, Nicolas Bergeal etc. all the "chers collègues " in LPEM for sharing the Lab-time with me. I am going to graduate, but the time I spent in LPEM ESPCI will be treasured up in my heart.

I wish to thank all the members in my army, all my Chinese friends in Paris, Zengwei Zhu, Huan Yang, Zhaosheng Wang, Liping Wang, Binxin Wu, Yingxiong Wang, Yan Qiao, Peilin Lang, Qian Yu, Yu Wang, Limin Cui, Lin Wen, Haitao Peng et al. We spent most of the free time together, helped and encouraged each other in Paris.

I would like to express my gratitude to Jiyun Ma for teaching me how to use the ABB Bomen DA8 spectrometer. Thank Bing Xu for helping me to build the reflectivity measurement system and to collect the data in IOP, CAS. Thank

Nanlin Wang and his Ph.D Gang Li for answering me so many questions about optical spectroscopy. Thank Cong Ren and Lei Shan for their useful discussions and kind help in scientific research. Thank Bairu Zhao, Beiyi Zhu, Bo Xu, Lixin Cao, and the secretaries of NLSC Si Xu and Jin Chen for their kind help during my study in IOP, CAS. I also thank Kui Jin, Xu Fang, Huaying Zhao, Ye Han, Weiyong Li, Ming Li, Tao Zou, Shuai Zhang, Xiaohui Chao, Yueju Fu, Hong Xiao, Jing Han, Shikun He, Bohong Li, Weijun Zhang, Fei Cheng, Fengjin Xia, Xiaorui Zheng for sharing the lab, the office, and the free time in IOP, CAS. We worked together, played together, helped and encouraged each other, I really enjoyed working with you guys.

I would like to thank Jiwei Li, Haihong Ji and Yuhang Jiang for taking care of all the paperwork during my study and thesis defence in IOP, CAS.

I wish to acknowledge the financial support from the Science and Technology Service of the French Embassy in China. I express my gratitude to Juliette Jin and CROUS for managing my scholarship.

Finally, I am extremely grateful to my parents for their support all along. I especially offer great gratitude to my wife Yamin for her understanding and encouragement. She provided all kinds of help and never complained during the preparation of my thesis.

Résumé

Lors que des atomes sont assemblés dans un solide, des nouveaux phénomènes surgissent en raison de l'interaction forte entre noyaux et électrons. Par exemple, dans des matériaux anisotropes de faible dimension ou dans des métaux à forte densit'e d'états au niveau de Fermi, des de densité de spin (SDW) ou de charge (CDW) peuvent se former à basse température. La supraconductivité est présente dans certains matériaux quand il refroidit en dessous d'une température critique. Toutes ces phases peuvent apparaître d' une façon isolée ou coexister avec une autre. Et, dans ce cas, une interaction forte ou de la compétition peut exister entre ces phases. Le mécanisme de formation de ces phases et les relations entre elles sont toujours le centre d'intérêt quand elles sont découvertes dans un nouveau matériau.

$Ba_{1-x}K_xFe_2As_2$ et $Ba(Fe_{1-x}Co_x)_2As_2$ ont été découverts comme une nouvelle famille de supraconducteurs à haute T_c. C'est le système supraconducteur Ba122 à base de fer. Le composé parent de cette famille est $BaFe_2As_2$ qui a une transition d'onde de densité de spin à environ 138 K. Lorsque le dopage du composé parent est fait par des trous [$Ba_{1-x}K_xFe_2As_2$] ou par des électrons [$Ba(Fe_{1-x}Co_x)_2As_2$], le magnétisme est supprimé et la supraconductivité apparaît. Dans une gamme de dopage considérablement large, la phase SDW et la supraconductivité coexistent. Dans ce cas, la symétrie du gap supraconducteur les relations entre les ordres coexistants produisent des phénoènes et des comportements nouveaux.

Dans cette thèse, nous avons étudié les propriétés optiques des supraconducteurs à base de fer dopés trous [$Ba_{1-x}K_xFe_2As_2$] et électrons [$Ba(Fe_{1-x}Co_x)_2As_2$]. Dans les composés dopés optimalement par K ou Co, nous avons trouvé différentes réponses dans la conductivité optique de basse énergie. En comparant les propriétés optiques et les sites de dopage de ces deux échantillons dopés de façon optimale, nous avons fourni des preuves solides pour une symmétrie d'appariement $s_\pm$ dans le système Ba122. Dans le composés sous-dopé $Ba_{0.6}K_{0.4}Fe_2As_2$ nous

avons observé, en plus du gap SDW et de celui supraconducteur, un plus petit gap à plus faible énergie. Nous avons étudié la dépendance en température et dopage des trois gaps. Avec cela, combinée à une analyse de poids spectral, nous avons conclu que ce gap nouveau partage les mêmes états électroniques que le condensat supraconducteurs. Nous avons interprété ce gap par un scénario de précurseur de la phase supraconductrice. En revanche, la transition SDW diminue les états électroniques disponibles pour le condensat supraconducteur, agissant comme un ordre en compétition à la supraconductivité.

Mots-clés: supraconducteurs à base de Fer, Ba122, onde de densité de spin, symétries du gap supraconducteur, spectroscopie optique

Abstract

When a mass of atoms are brought together to form a solid state material, many and various novel phenomena arise in the material due to the strong interactions among nuclei and electrons. For example, spin-density-wave (SDW) or charge-density-wave (CDW) occurs at low temperature in anisotropic, low-dimensional materials or in metals with high density of states at the Fermi level. Superconductivity is exhibited by certain materials when cooling it down to a critical temperature. All these phases can dominate the material solitarily or coexist with each other in one material, indeed, strong coupling or competition may exist among these phases when coexisting with each other in one material. The driving mechanism of these phases and the relations between them are always the center of interest when they are discovered in a new material.

$Ba_{1-x}K_xFe_2As_2$ and $Ba(Fe_{1-x}Co_x)_2As_2$ were discovered as a new family of high-T_c superconductors, the Ba122 system iron-based superconductor. The parent compound of this family is $BaFe_2As_2$ which undergoes a spin-density-wave (SDW) transition at about 138 K. When doping the parent compound with holes [$Ba_{1-x}K_xFe_2As_2$] or electrons [$Ba(Fe_{1-x}Co_x)_2As_2$], the magnetism is suppressed and superconductivity emerges in this material. In a considerably large doping scale, the SDW phase and superconductivity coexist with each other. In this case, the superconducting paring symmetry and the relations between the coexistent orders in the Ba122 system materials are highly desired.

In this thesis, we studied the optical properties of the hole [$Ba_{1-x}K_xFe_2As_2$] and electron [$Ba(Fe_{1-x}Co_x)_2As_2$] doped Ba122 system iron-based superconductors. In the optimally K and Co doped samples, we found different low frequency optical response. By comparing the optical properties and the doping sites of these two optimally doped samples, we provided strong evidence for an $s_\pm$ pairing symmetry in Ba122 system iron-based superconductors. In the underdoped $Ba_{1-x}K_xFe_2As_2$ samples, we observed a smaller partial energy gap besides the SDW and superconducting gaps. We studied the temperature and doping

dependence of the three gaps, combined with a spectral weight analysis, we concluded that the smaller partial energy gap shares the same electronic states with superconducting condensate, a precursor scenario is preferred for the smaller partial gap. In contrast, the SDW transition depletes the electronic states available for superconducting condensate, acting as a competitive order to the superconductivity.

Keywords: iron-based superconductor, Ba122, spin-density-wave, pairing symmetry, optical spectroscopy

摘要

大量的原子凝聚在一起形成固体材料时，原子和原子之间，电子和电子之间以及原子和电子之间的各种关联和相互作用导致许多奇特的物理现象。比如，低温下，自旋密度波(SDW)和电荷密度波(CDW)现象经常发生在各向异性的低维材料或费米面附近电子浓度比较高的金属材料中。许多材料当降至某个特定温度以下时，会表现出超导电性。这些奇异的物理现象的出现，在物理学中被称为相变。在某种特定材料中，这些相可以单独存在，也可以多个相共存。当多个相共同存在于某种材料中时，这些相之间可以相互耦合或相互竞争。所以，当在某种新材料中发现这些相时，相变的机制以及这些相之间的相互关系便成为物理学家的兴趣焦点。

$Ba_{1-x}K_xFe_2As_2$和$Ba(Fe_{1-x}Co_x)_2As_2$是最近被发现的新型高温超导体中的一个体系：Ba122体系铁基超导体。这个体系的母体是$BaFe_2As_2$，该材料在大约138K时发生自旋密度波相变。对$BaFe_2As_2$进行空穴掺杂[$Ba_{1-x}K_xFe_2As_2$]或电子掺杂[$Ba(Fe_{1-x}Co_x)_2As_2$]，磁性会被明显的压制，同时导致超导电性的出现。对于Ba122体系的材料，在很宽的掺杂范围内，自旋密度波和超导电性是共同存在的。因此，在Ba122体系铁基超导体中，超导电性的配对机制，电子配对的对称性以及超导电性和自旋密度波的相互关系引起了科学家的广泛兴趣。

本论文研究了空穴掺杂[$Ba_{1-x}K_xFe_2As_2$]和电子掺杂[$Ba(Fe_{1-x}Co_x)_2As_2$]的Ba122体系铁基超导体的光学性质。在最佳K掺杂和Co掺杂的样品中，我们发现了明显不同的低频光学响应。通过比较两种掺杂对低频光学响应的影响，结合材料的晶体结构和掺杂位置，我们对铁基超导体序参量具有$s_{\pm}$对称性提供了有力证据。通过对最佳K掺杂样品的低频光电导的拟合分析，我们发现Ba122体系铁基超导体有明显的多带特征，不同带中的载流子散射率存在显著的不同，并且表现出极其不同的温度依赖。进入超导态后，多个带中均有能隙的打开。在欠掺杂的$Ba_{1-x}K_xFe_2As_2$样品中，除了自旋密度波和超导能隙外，我们还观察到一个小的部分能隙。通过研究这三个能隙的温度依赖和掺杂依赖，结合红外光电导的谱重分析，我们发现这个小的部分能隙与超导电性共享大部分电子态密度，具有相同的掺杂依赖，这个现象表明这个小的部分能隙

可能是超导的先驱所导致。相反，自旋密度波能隙的打开降低了和超导相关的电子态密度，表明在Ba122体系中，自旋密度波与超导电性存在相互竞争的关系。

关键字： 铁基超导体，Ba122体系，自旋密度波，超导电子配对对称性，红外光谱

Contents

List of Figures

List of Tables

Résumé Étendu

Le phénomène de la supraconductivité a été découvert il ya 100 ans par un physicien hollandais, Kamerlingh Onnes. Il a été la première personne à liquéfier l'hélium trois ans auparavant et il a entamé une série d'expériences pour mesurer la résistivité des métaux. Il a constaté que lorsque le mercure est refroidi à environ 4.2 K, il perd brusquement sa résistivité électrique dans une transition de phase vers un nouvel état de la matière, qu'il a nommé la supraconductivité. Ce phénomène a été expliqué théoriquement par Bardeen, Cooper et Schrieffer (BCS) dans les années 1950 [1, 2], dans une théorie fondée sur la formation de paires d'électrons (paires de Cooper), avec une énergie de liaison caractéristique, le gap supraconducteur . Au milieu des années 1980, Bednorz et Müler ont constaté que une céramique à base de La-Ba-Cu-O devenait supraconductrice en dessous d'une température critique (T_c) élevée de 35 K [3]. Plusieurs autres oxydes supraconducteurs à base de cuivre ont encore été découverts et il est aujourd'hui évident qu'ils ne suivent pas la théorie standard BCS. Dans le début des années 2000, la supraconductivité a été trouvé dans MgB_2 à 39 K [4]. Outre la haute température critique, MgB_2 est particulier puisqu'il a deux bandes au niveau de Fermi et les deux deviennent supraconductrices. Une autre percée dans la supraconductivité est venue avec la découverte des matériaux qui combinent le fer avec des pnictogènes (P, As) [5–8] ou chalcogènes (Se, Te) [9, 10]. Cette classe de matériaux, appelés génériquement pnictures de fer, ont une supraconductivité non conventionnelle (comme celui dans les cuprates) combinée avec la supraconductivité mutibande (tel que MgB_2). La supraconductivité sera traitée avec plus de détail sur le chapitre 2 et les pnictures de fer dans le chapitre 4. Pour la discussion suivante, nous avons besoin d'introduires certaines propriétés des supraconducteurs non conventionnels. Les cuprates et les pnictures de fer ont, le deux, un fort caractère structurel bi-dimensionnel. La physique des cuprates est dominé par des plans CuO_2 et celle des pnictures de fer par des plans FeAs. Les deux systèmes permettent de faire varier les propriétés supraconductrices (dont

T_c) en changeant le niveau de densité de charge dans les plans à travers le dopage (concentration en oxygène ou substitution de cationique). Le dopage qui produit la T_c maximales est appelé *optimal*. il définit des régions *sousdopées* (densité de charge plus faible) et *surdopée* (densité de charge plus large), où T_c diminue et finalement s'annule.

Cette thèse s'inscrit dans le cadre d'un projet de thèse en cotutelle entre l'Université Pierre et Marie Curie (Paris 6), Paris, France et l'Institut de Physique, Académie Chinoise des Sciences, Pékin, Chine. Selon le plan initial de ce projet, le sujet de ma thèse serait d'étudier les propriétés optiques (infrarouge, visible et ultra-violet) de La-Bi2201 ($Bi_2Sr_{2-x}La_xCuO_6$) à travers le diagramme de phases, travaillant 6 mois par an dans chaque institution. À Paris, mon travail expérimental était d'apprendre comment faire fonctionner les spectromètres et de mesurer les propriétés optiques des supraconducteurs. À Pékin, j'ai caractérisé les échantillons utilisés pour nos expériences et j'ai construit un système de mesure de réflectivité à basse température, similair à celui de Paris, pour le FTIR ABB Bomen DA8 à Pékin, y compris son système de contrôle de la température, l'optique et des pièces mécaniques. La partie instrumentation de ma thèse a parfaitement suivi le plan inital. A ce jour, à l'Institut de Physique de l'Académie chinoise de la physique, à Pékin, l'ensemble du système de mesure de réflectivité à basse température pour le spectromètre ABB Bomen DA8 est complètement mis en place. La réflectivité à basse température (de 5 à 300 K) peut être mesurée en utilisant une techinque d'évaporation d'or *in-situ*. Le principe et la configuration du système de mesure et de la techinque d'évaporation d'or *in-situ* seront discutés en détail dans le chapitre des méthodes expérimentales.

La spectroscopie optique est un outil très puissant pour étudier les supraconducteurs. Comme la conductivité optique est sensible aux porteurs de charge à basse énergie, elle est largement utilisée pour sonder les gaps de charge, en particulier le gap supraconducteur. Elle fournit également d'abondantes informations sur la symétrie de ce gap. Dans les milieux conducteurs, la spectroscopie optique mesure aussi l'énergie (la fréquence) du temps de vie (ou le libre parcours moyen) des porteurs de charge ainsi que leur masse effective. Les deux techniques les plus connues dans l'étude des supraconducteurs sont la spectroscopie de photoémission

à résolue en angle (ARPES) et la microscopie à effet tunnel (STM). ARPES est une technique expérimentale qui permet d'observer directement la densité d'excitations électroniques à une particule dans l'espace réciproque, et qui fournit des informations sur l'énergie et le moment d'un électron. Mais ARPES est une technique sensible à la surface et sa profondeur de pénétration est seulement de quelques angstroms. En outre, sa résolution en énergie n'est pas très élevé. STM a une meilleure résolution en énergie sondes la densité locale d'états électroniques. Elle mesure directement le gap supraconducteur dans l'espace réel. Cependant, c'est aussi une technique sensible à la surface. En contraste à l'ARPES et STM, la spectroscopie optique n'a pas une une résolution en moment et ne sonde pas la densité locale d'états électroniques. Mais elle a la meilleure résolution énergétique parmi ces trois techniques et sa profondeur de pénétration atteint quelques centaines de nanomètresm sondant ainsi le bulk.

Comme mentionné précédemment, l'objet initial de mon travail était d'étudier les propriétés électrodynamiques des supraconducteurs cuprates par spectroscopie infrarouge. En particulier, étudier le diagramme de phase optique de La-Bi2201 ($Bi_2Sr_{2-x}La_xCuO_6$). Outre la possibilité d'obtenir de gros monocristaux, ce système a de nombreuses avantages: (i) il a seulement un plan CuO_2 par maille, ce qui évite des effets de couplage interplan, (ii) la substitution de La par Sr introduit le plus bas effet de désordre dans les plans CuO_2 responsables de la supraconductivité, (iii) une plage de dopage très large est disponible dans ce système. Elle s'étend sur les concentrations de trous de l'extrêmement sous-dopé (non supraconducteur) au très surdopée, (iv) sa T_c pas trop élevé donne accès à une large région en température pour étudier les propriétés état normal à basse température, et (v) sa T_c pas trop faible permet de sonder l'état supraconducteur. A l'ESPCI, UPMC, Paris, nous avons mesuré les propriétés optiques de monocristaux de La-Bi2201 ($Bi_2Sr_{2-x}La_xCuO_6$) pour 7 dopages (x = 0,1, 0,2, 0,4, 0,6, 0,7, 0,8 et 1,0). Juste après avoir terminé les mesures de réflectivité infrarouge, de gros monocristaux des supraconducteurs à base de fer single sont devenus disponibles. Nous avons alors tourné notre attention vers ces pnictures de fer. Malgré nos nombreux de résultats sur La-Bi2201, les inclure dans ce manuscrit ne permettrait pas de rendre un texte clair. Donc nous

n'allons pas les discuter en détail dans cette thèse. Pour la petite histoire, notre analyse à ce jour sur ce système donne les résultats suivants: (i) nous avons constaté qu'un gap partiel dans l'état normal (pseudogap) peut être déterminée à partir de la dépendence en fréquence de la durée de vie des porteurs. Il est présent à tous les dopages mesurée, en particulier, en dans le régime surdopée, une propriété qui n'est pas partagée par la plupart des cuprates. (ii) La masse effective est constante à travers tout le diagramme de phase tandis que la densité de porteurs change d'un facteur de 10. Cela indique que la transition menant à une phase isolante à zéro dopage n'est pas gouvernée par une divergence de masse, mais plutôt par la diminution de la densité de charge. Cela indique que la réponse dynamique des quasiparticules dans $Bi_2Sr_{2-x}La_xCuO_6$ est locale et n'est pas fortement influencé par la transition de Mott à longue portée.

Le sujet que je vais traiter dans ma thèse est le electrondynamque des pnictures de fer supraconductrices. Un nombre important de questions existent dans cette nouvelle famille de supraconducteurs: Quelle est la symétrie du paramètre d'ordre? Est-ce qu'il change avec le dopage? Quelle est la colle des paires de Cooper? Quelle est la relation entre le magnétisme et la supraconductivité dans ces matériaux?

Les résultats dont je parle dans mon mémoire concernent notamment quatre échantillons: des cristaux du système Ba122 dopés trous $Ba_{1-x}K_xFe_2As_2$ (x = 0,4, 0,2 et 0,12) ou électrons $Ba(Fe_{1-x}Co_x)_2As_2$ (x = 0,08). Néanmoins, une grande partie de mon travail était de comprendre et de perfectioner la mesure de la réflectivité optique. Dans cette perspective, j'ai mesuré de nombreux autres échantillons à la fin de ma thèse, mais nous ne les comprenons pas assez pour inclure tous les résultats dans ce manuscrit. Ces échantillons sont des cristaux de Ba122 dopés électrons, $Ba(Fe_{1-x}Co_x)_2As_2$ (x = 0,015, 0,045, 0,12 et 0,15) et les chalcogenures $Fe_yTe_xSe_{1-x}$ pour 5 compositions différentes.

Dans cette thèse, nous présentons l'électrodynamique de Ba122. Nos mesures optiques ont été réalisées sur des spectromètres Bruker IFS113 et IFS66v à Paris et le visible et l'UV avec un spectromètre à fibre optique AvaSpec-2048×14. Dans $Ba_{1-x}K_xFe_2As_2$ (x = 0,4), optimalement dopé, en dessous de T_c, la con-

ductivité optique disparaît en dessous d'un seuil d'absorption, et aucune conductivité résiduelle apparaît aux basses fréquences dans l'état supraconducteur. Cela représente un gap supraconducteur bien défini, complètement ouvert. En revanche, dans $Ba(Fe_{1-x}Co_x)_2As_2$ (x = 0,08), aussi optimalement dopé, une conductivité résiduelle importante à basse énergie, qui représente des quasiparticules non appariés, est observée dans l'état supraconducteur. Cette différence frappante dans la réponse basse fréquence optique entre échantillons dopés par du K et par du Co est une preuve d'une symétrie d'appariement $s_{\pm}$ dans les supraconducteurs Ba122. La symétrie $s_{\pm}$ signifie que, dans un supraconducteur multibandes, des différentes bandes ont un gap isotrope (s) avec des phases opposées ($\pm$). Dans ce cas, la diffusion interbandes mélange des états de trous et d'électrons ayant des phases opposées et, par conséquent, brise des paires de Cooper. Comme le dopage par K se passe en dehors des plans FeAs, qui dominent la structure de bandes, on ne s'attend pas à une diffusion interbandes forte. Inversement, le dopage avec Co va directement dans les plans FeAs. Le Co va alors agir comme des centres de diffusion. Nous associons cette diffusion à la brisure de paires de Cooper qui va créer la conductivité optique résiduelle à basse énergie. La différence de la conducitivité otique dans ces deux sytèmes est illustrée dans la Fig. 1. Nous avons également étudié les spectres optiques de $Ba_{1-x}K_xFe_2As_2$ (x = 0,2 et 0,12) sousdopé. L'ouverture du gap supraconducteur et de celui d'onde de densité de spin sont clairement observés. En plus, nous avons également observé l'ouverture d'un petit gap partiel en dessous d'environ 75 K. Une analyse quantitative montre que le petit gap transfère du poids spectral des basses aux hautes fréquences, mais quand la supraconductivité est établi, cette partie du poids spectral rejoint le condensat supraconducteur. En revanche, le gap d'onde de densité de spin diminue le poids spectral à faible énergie disponible pour supraconducteurs condensat. Ces observations suggèrent que le petit gap est un ordre précurseur de la supraconductivité tandis que celui d'onde de densité de spin agit comme un ordre en compétition avec la supraconductivité. La dépendance en dopage des gaps est également favorable à ce scénario.

Cette thèse est divisée en six parties (chapitre 2 à 7). Le chapitre 2 donne une brève introduction à la supraconductivité. Dans le chapitre 3, nous introduisons

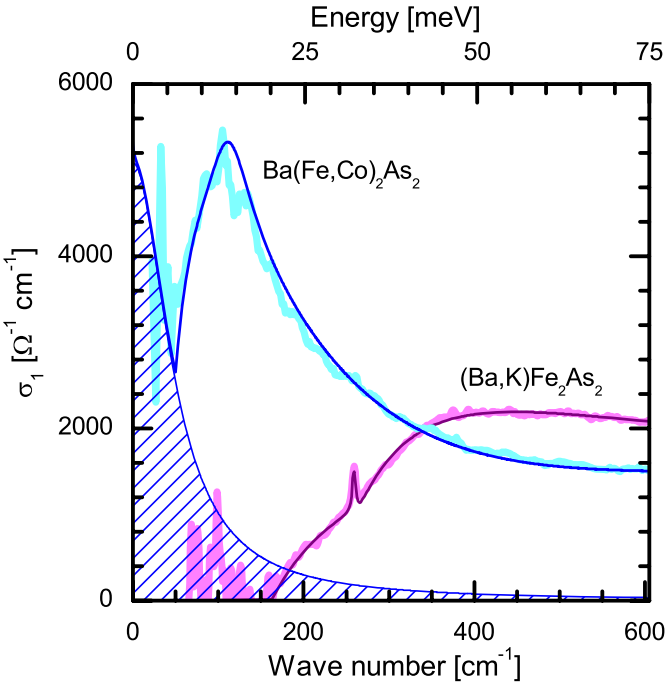

Figure 1: La conductivité optique pour $Ba(Fe_{0.92}Co_{0.08})_2As_2$ et $Ba_{0.6}K_{0.4}Fe_2As_2$ à 5 K.

quelques principes fondamentaux de la spectroscopie infrarouge, et expliquons comment nous avons extrait les constantes optiques de la réflectivité mesuré et comment nous modélisons nos données. Le chapitre 4 présente la découverte et les propriétés de base des pnictures de fer à haute T_c. Le chapitre 5 décrit notre technique expérimentale, y compris la préparation des échantillons. Dans le chapitre 6, nous présentons nos données optiques ainsi que l'analyse de nos résultats expérimentaux. Le chapitre 7 fournit un résumé global de ce travail.

Chapter 1

Introduction

The phenomenon of superconductivity was discovered 100 years ago by a Dutch physicist, Kamerlingh Onnes. He was the first person to liquefy helium three years before and he went on a series of experiments to measure the resistivity of metals. He found that when mercury is cooled down to about 4.2 K, it loses abruptly its electrical resistivity in a phase transition to a new state of matter, which he named superconductivity. This phenomenon was explained theoretically by Bardeen, Cooper and Schrieffer (BCS) in the late 1950s [1, 2], in a theory based on the formation of pairs of electrons (Cooper pairs) with a characteristic binding energy, the superconducting gap. In the mid-1980s, Bednorz and Mueller found that a La-Ba-Cu-O ceramic became superconducting below an unprecedented high critical temperature (T_c) of 35 K [3]. Several other copper oxide based superconductors were further discovered and it is nowadays clear that they do not follow the standard BCS theory. In the early 2000s, superconductivity was found in MgB_2 at 39 K [4]. Besides the high critical temperature, MgB_2 is characterized by the property of having two bands at the Fermi level, both becoming superconducting. Another breakthrough in superconductivity came with the discovery of the phenomenon in materials that combine iron with pnictogens (P, As) [5–8] or chalcogens (Se, Te) [9, 10]. This class of materials, generically called iron-pnictides, shows unconventional superconductivity (such as the one in cuprates) combined with mutiband superconductivity (such as MgB_2). Superconductivity will be discussed in more detail in Chapter 2 and iron-pnictides in Chapter 4. For the following discussion, we need to introduce some properties of unconventional superconductors. Both cuprates and iron-pnictides have a strong two dimensional structural character. The physics of cuprates is strongly dominated by CuO_2 planes and that of iron-pnitides by FeAs planes. Both systems

allow to vary the superconducting properties (and T_c) by changing the charge density level in the planes through doping (oxygen concentration or cation substitution). The doping that produces the maximum T_c is called *optimal*. It defines *underdoped* (smaller charge density) and *overdoped* (larger charge density) regions where T_c decreases, and eventually vanishes. This sets the initial stage for this thesis work.

This thesis is part of a joint Ph.D project between the Université Pierre et Marie Curie (Paris 6), Paris, France and the Institute of the Physics, Chinese Academy of Sciences, Beijing, China. According to the initial plan of this project, the subject of my thesis would be to study the optical (infrared, visible and ultra-violet) properties of La-Bi2201 ($Bi_2Sr_{2-x}La_xCuO_6$) throughout the phase diagram working 6 months per year on each side. In Paris, my experimental work was to learn how to operate the spectrometers and to measure the optical properties of superconductors. In Beijing, I characterized the samples used for our experiment and build a low temperature reflectivity measurement system similar to the one in Paris for the ABB Bomen DA8 FTIR spectrometer, including its temperature controlling system, optics and mechanical parts. The instrumentation portion of my thesis followed the initial plan perfectly. At this time, in the Institute of Physics, Chinese Academy of Physics, Beijing, the whole low temperature reflectivity measurement system for the ABB Bomen DA8 FTIR spectrometer is completely set up. Reflectivity at low temperatures (from 5 K to 300 K) can be measured using the *in situ* gold overfilling technique in this measurement system. The principle and setup of the measurement system and the *in situ* gold overfilling technique will be discussed in detail in the experimental methods chapter. As for the systems studied, the situation evolved significantly.

Let's first make a parenthesis to talk about the experimental technique chosen for our work. Optical spectroscopy is a very powerful tool to investigate superconductors. Since the optical conductivity is sensitive to charge carriers at low energies, it is widely used to probe charge gaps, in particular the superconducting gap. It also provides abundant information on the symmetry of this gap. In conducting media, optical spectroscopy also measures the energy (frequency) dependent charge carriers lifetime (or mean free path) and effective

mass. The two fore front techniques to study superconductors are angle-resolved photoemission spectroscopy (ARPES) and scanning tunneling microscopy spectroscopy (STM). ARPES is a direct experimental technique to observe the density of single-particle electronic excitations in the k space of solids, and it provides information on both the energy and momentum of an electron. But ARPES is a surface sensitive technique and its penetration depth is only several unit cell, in addition, its energy resolution is not very high. STM has a better energy resolution and it probes the local electronic density of states directly measuring the superconducting gap in real space. However, it's also a surface sensitive technique. In contrast with ARPES and STM, optical spectroscopy has neither momentum resolution nor probes the local electronic density of states, but it has the highest energy resolution among these three techniques and its penetration depth reaches a few hundred nanometers, certainly representing a bulk sensitive experimental technique.

As I mentioned earlier, the initial subject of my work was to investigate the electrodynamic properties of copper oxide superconductors with infrared spectroscopy. In particular, to study the optical phase diagram of La-Bi2201 ($Bi_2Sr_{2-x}La_xCuO_6$). Besides the possibility of obtaining large single crystals, this system has many and various other advantages: (i) It has only one single CuO_2 plane per unit cell, which avoids effects of interplane coupling; (ii) the substitution of La for Sr atoms introduces the lowest influence of disorder into the CuO_2 planes responsible for the superconductivity; (iii) large doping range is available in this system. It spans hole concentrations from extreme underdoped (non superconducting) to highly overdoped samples; (iv) its not too high T_c gives enough region in temperature for studying the normal state properties at low temperatures; and (v) its not too low T_c allows to probe into the superconducting state. At ESPCI, UPMC, Paris, we measured the optical properties of La-Bi2201 ($Bi_2Sr_{2-x}La_xCuO_6$) single crystals for 7 dopings (x = 0.1, 0.2, 0.4, 0.6, 0.7, 0.8 and 1.0) which spans hole concentrations from extremely underdoped (non superconducting) to highly overdoped samples. Just after we finished theses infrared reflectivity measurements, large single crystals became available on the newly discovered iron-based superconductors, hence we turned our atten-

tion to these iron-pnictide superconductors. Despite the large body of results on La-Bi2201 single crystals, including them in the manuscript would not help to make a clear text. So we are not going to discuss it at length in this thesis. For the record, our analysis so far on this system gives the following outcome: (i) we found that a partial gap in the normal state (pseudogap) can be determined from the frequency dependent carrier lifetime. It is present at all measured dopings, in particular deep into the overdoped regime, a property not shared by most cuprates. (ii) The optical effective mass enhancement is constant throughout the phase diagram while the charge density changes by a factor of 10. This indicates that the transition leading to an insulating phase at zero doping is not governed by a mass divergence, but rather by a charge density alone. This indicates that the dynamical response of quasiparticles in $Bi_2Sr_{2-x}La_xCuO_6$ is local and not strongly influenced by the long range Mott transition.

The subject I will treat in my thesis is the electrondynamics of iron-pnictides superconductors. A sizeable number of questions exist in this new family of superconductors: What is the symmetry of the order parameter? Does it change with doping? What is the glue of the Cooper pairs? What is the relation between the magnetism and the superconductivity in these materials?

The results I am discussing in my thesis concern particularly four samples: hole doped Ba122 system single crystals, $Ba_{1-x}K_xFe_2As_2$ (x = 0.4, 0.2 and 0.12) and and electron doped $Ba(Fe_{1-x}Co_x)_2As_2$ (x = 0.08). Nevertheless, a large body of my work was to understand and perfectionate the optical reflectivity measurement. In that perspective, I measured many other samples at the end of my thesis and we do not understand them enough to include all the results in the manuscript. These samples are electron doped Ba122 system single crystals, $Ba(Fe_{1-x}Co_x)_2As_2$ (x = 0.015, 0.045, 0.12 and 0.15); and $Fe_yTe_xSe_{1-x}$ single crystals for 5 different compositions.

In this thesis, we present the electrodynamics of the hole and electron doped Ba122 system iron-based superconductors. Our infrared optical measurement was performed on Bruker IFS113v and IFS66v/s spectrometers in Paris. The visible and UV range was measured with an AvaSpec-2048 $\times$ 14 model fiber op-

tic spectrometer. In optimally doped $Ba_{1-x}K_xFe_2As_2$ (x = 0.4), below T_c, the optical conductivity vanishes below an absorption edge, and no residual conductivity appears at low frequencies in the superconducting state. This represents a well defined fully open superconducting gap. In contrast, in optimally doped $Ba(Fe_{1-x}Co_x)_2As_2$ (x = 0.08), a large residual conductivity at low energies, representing unpaired quasiparticles, is observed in the superconducting state. This striking difference in low frequency optical response between the K and Co doped samples is an evidence for an $s_\pm$ pairing symmetry in Ba122 iron-based superconductors. The $s_\pm$ symmetry means that, in a multiband superconductor, different bands have isotropic (s) gaps with opposite phases ($\pm$). In this case, interband scattering mixes states with opposing phases and is, therefore, pair breaking. As K doping goes out of the FeAs plane, which dominates the band structure, one does not expect strong interband scattering. Conversely, Co doping goes directly into the FeAs plane and acts as impurity scattering centers. We associate this scattering with the pair breaking leading to the residual low frequency optical conductivity. We also investigated the optical spectra of the underdoped $Ba_{1-x}K_xFe_2As_2$ (x = 0.2 and 0.12) samples. The opening of the superconducting and a normal state spin density wave (SDW) gaps were clearly observed. In addition, we also observed a small partial gap opening below about 75 K. A spectral weight analysis shows that the small partial gap transfers the low frequency spectral weight to high frequencies, but when superconductivity is established in the material, this part of spectral weight joints the superconducting condensate. In contrast, the SDW gap depletes the low energy spectral weight available for superconducting condensate. These observations suggest that the small partial gap originates in a precursor order to superconductivity while the SDW acts as a competitive order to the superconductivity. The doping dependence of the gaps in these materials is also supportive of this scenario.

This thesis is divided into six parts (Chapter 2 to 7). Chapter 2 gives a brief introduction to superconductivity. In Chapter 3 we introduce some fundamentals of infrared spectroscopy, and explain how we extract the optical constants from the measured reflectivity and how we describe our data with models. Chapter 4 introduces the discovery and basic properties of iron-based high-T_c supercon-

ductors including an extensive literature review. Chapter 5 describes our experimental technique including the sample preparation. In Chapter 6 we present our optical data and give the analysis of our experimental results. Chapter 7 provides an overall summary of our work.

Chapter 2

Fundamentals of superconductivity

2.1 The basic phenomena of superconductivity

2.1.1 The discovery of zero resistance

In 1908, a Dutch physicist H. Kamerlingh Onnes achieved the lowest temperature (4.2 K by then) all over the world by liquifying the helium in his laboratory at Leiden and initiated the field of low-temperature physics. Three years later, Kamerlingh Onnes measured the resistance of mercury down to liquid helium temperature, a novel phenomenon surprised him: at about 4.2 K, the resistance of Mercury abruptly disappeared, as shown in Fig. 2.1. He immediately realized

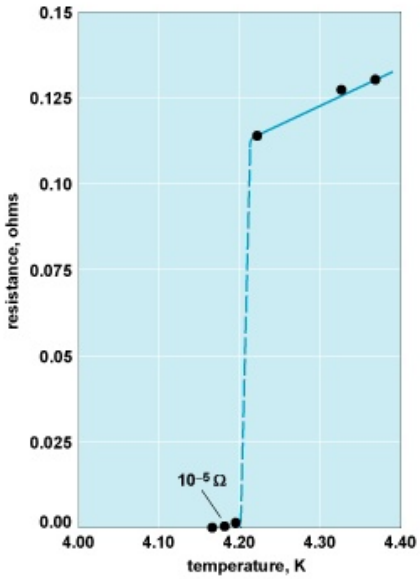

Figure 2.1: The resistance of Hg as a function of temperature measured by Kamerlingh Onnes.

the significance of this discovery and claimed that “Mercury has passed into a

new state, which on account of its extraordinary electrical properties may be called the superconductive state". The temperature, at which the resistance disappears, is called the critical temperature T_c. Indeed, superconductivity is not peculiar to mercury. More than 20 metallic elements in the periodic table can become superconductors.

2.1.2 Meissner effect

In 1933, German scientists Meissner and Ochsenfeld studied the magnetic properties of the superconducting state. They found that if a normal metal in a magnetic field (not too strong) is cooled below its superconducting critical temperature, the magnetic flux is abruptly excluded from the interior of the material, namely, a magnetic field can not penetrate into the interior of a superconductor. This phenomenon is know as perfect diamagnetism and also referred to as the "Meissner effect".

Note that this is quite different from a perfect conductor. If a perfect conductor is moved from a zero magnetic field region to a magnetic field, according to the Faraday's induction law, eddy currents should be induced to cancel the magnetic field in the interior. However, if a magnetic field were initially established in a perfect conductor, when moved to a field free region, induced eddy currents arise to maintain the magnetic field. Hence, the magnetic field in the interior of a perfect conductor depends on the history of external field. In a superconductor, the field is always zero, completely ignoring the history of external magnetic field.

2.1.3 Critical Temperature, Field and Current

As we discussed above, superconductivity is associated with a critical temperature T_c, below which the superconducting properties are displayed. But above T_c, the material is completely normal. Actually, not only the temperature, but also a magnetic field can destroy superconductivity. Consider a superconductor at a temperature T below its critical temperature T_c, if a magnetic field H applied to the superconductor is strong enough, superconductivity is destroyed

and the material turns back to the normal state. The magnetic field driving a superconductor back to the normal state is defined as the critical field H_c of the superconductor. The critical field H_c is a function of temperature. At zero temperature, H_c reaches the maximum $H_c(0)$, and monotonously decreases to zero at T_c. Fig. 2.2 shows the temperature dependence of the critical field.

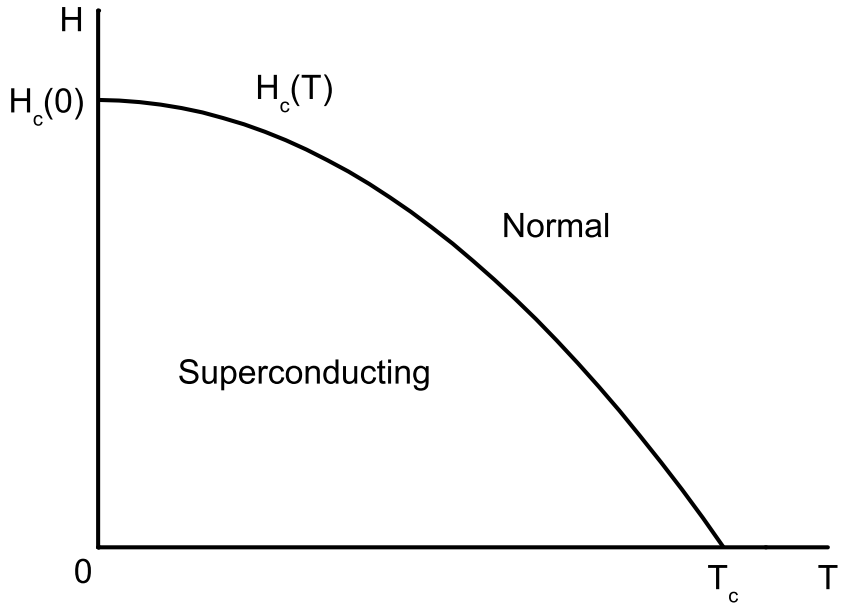

Figure 2.2: The temperature dependence of the critical magnetic field.

According to their magnetic properties, superconductors are classified into Type I and Type II. The magnetic properties of Type I superconductors are dominated by only one critical field H_c. The left panel of Fig. 2.3 shows the magnetization curve of Type I superconductors. Below H_c, $-M = H$, no magnetic flux penetrates into the superconductor (perfect diamagnetism). If the applied magnetic field exceeds the critical filed, the entire material is driven back to the normal state and completely penetrated by magnetic field. The right panel of Fig. 2.3 shows the magnetization curve of Type II superconductors. It's characterized by two critical fields, H_{c1} and H_{c2}. Below the lower critical field H_{c1}, the magnetization curve exhibits the same behavior as the one of Type I superconductors, $-M = H$, there is no penetration of flux. When the applied field exceeds the lower critical filed, $H > H_{c1}$, M starts to fall smoothly, indicating

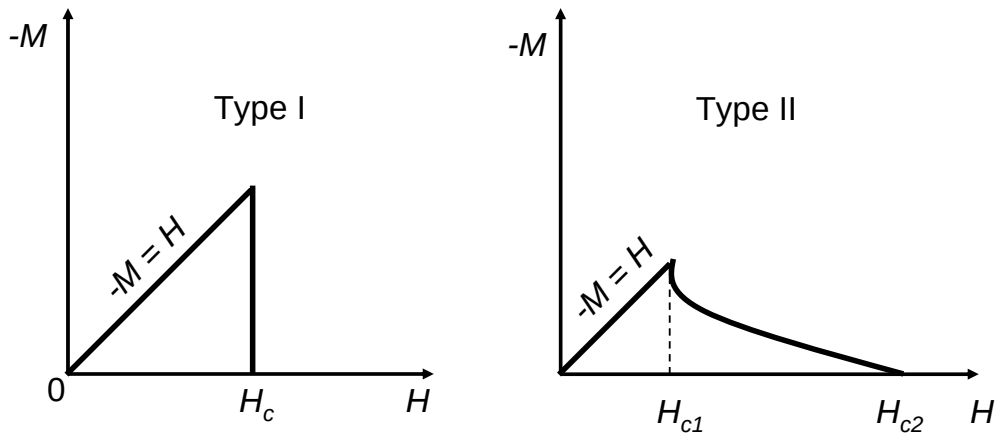

Figure 2.3: Magnetization curves of superconductors. Left panel: type I; Right panel: type II.

that magnetic flux starts to penetrate into the superconductor, the material enters a complicated state with both normal and superconducting regions, known as the mixed state, but the material still shows zero resistance. As the applied magnetic field increases, more and more flux penetrates into the superconductor and superconducting regions continuously shrink. When the applied magnetic field reaches H_{c2}, called the upper critical field, the magnetization falls to zero, the entire material reverts to the normal state and magnetic field penetrates perfectly.

Equivalent to a magnetic field, a sufficiently strong current applied to a superconductor can also cause its resistance to return to the normal state value, this current is called critical current I_c.

From these basic properties of superconductors, it's easy to infer that there is a characteristic energy for the forming of superconducting state. When an external energy, such as temperature, magnetic field or current, applied to the superconductor is sufficiently high, superconductivity is destroyed.

2.2 Cooper pairs

Since the discovery of superconductivity in 1911, a lot of effort had gone into understanding the origin and mechanism of this amazing phenomenon. One of the most historic steps leading to the successful formulation of the microscopic theory of superconductivity was the model calculation performed by Cooper in 1956 [11]. He showed that if a weak attractive interaction exists, regardless of how weak it is, electrons can be bound into pairs, the normal ground state of an electron gas is unstable against the formation of at least one bound pair. To see how this instability comes, we consider two electrons added to a Fermi sea at the ground state $T = 0$, the Fermi sea is not affected by these two electrons and the only effect of the Fermi sea is to exclude these two electrons from occupying all the states for $k < k_F$ due to the Pauli exclusion principle. Thus, a many-body problem is converted into a two-body problem. In order to have the lowest-energy state, we assume that the two electrons have equal and opposite momentum, so the orbital wavefunction of the two electrons, having coordinates $\mathbf{r}_1$ and $\mathbf{r}_2$ can be written in the form

$$\psi_0(\mathbf{r}_1, \mathbf{r}_2) = \sum_k g_k e^{i\mathbf{k}\cdot\mathbf{r}_1} e^{-i\mathbf{k}\cdot\mathbf{r}_2} = \sum_k g_k e^{i\mathbf{k}\cdot(\mathbf{r}_1-\mathbf{r}_2)} \tag{2.1}$$

all the states are occupied for $k < k_F$, so we get

$$g(k) = 0, \quad \text{for} \quad k < k_F \tag{2.2}$$

considering the antisymmetry of the total wavefunction with respect to exchange of the two electrons, we write it as

$$\psi_0(\mathbf{r}_1 - \mathbf{r}_2) = \left[\sum_{k>k_F} g_k \cos\mathbf{k}\cdot(\mathbf{r}_1 - \mathbf{r}_2)\right](S_{+\frac{1}{2}}S_{-\frac{1}{2}} - S_{-\frac{1}{2}}S_{+\frac{1}{2}}) \tag{2.3}$$

The Schrödinger equation of the two electrons system is

$$-\frac{\hbar^2}{2m}(\nabla_1^2 + \nabla_2^2)\psi_0 + V(\mathbf{r}_1 - \mathbf{r}_2)\psi_0 = E\psi_0 \tag{2.4}$$

where $V(\mathbf{r}_1 - \mathbf{r}_2)$ represents the interaction potential of the two electrons. By inserting Eq. 2.3 into the Schrödinger equation Eq. 2.4, we obtain

$$(E - 2\epsilon_k)g_k = \sum_{k'>k_F} V_{kk'}g_{k'} \tag{2.5}$$

where $\epsilon_k = \frac{\hbar^2 k^2}{2m}$, and $V_{kk'}$ are the matrix elements of the interaction potential. This $V_{kk'}$ represents the strength of the potential for scattering a pair of electrons with momentum (k', -k') to a momentum (k, -k). It's very difficult to analyze this situation for general $V_{kk'}$, in order to simplify the problem, Cooper introduced a serviceable approximation

$$V_{kk'} = \begin{cases} -V, & \text{for} \quad E_F \leq \epsilon_k \leq E_F + \hbar\omega_c \\ & \quad E_F \leq \epsilon_{k'} \leq E_F + \hbar\omega_c \\ 0, & \text{Otherwise} \end{cases} \tag{2.6}$$

where ω_c is a cut-off frequency. This approximation means that the attractive interaction between the two electrons only happens for states out to a cut-off frequency energy $\hbar\omega_c$ away from the Fermi energy. Then by inserting the Eq. 2.6 into Eq. 2.5, we obtain

$$(E - 2\epsilon_k) g_k = -V \sum_{k' > k_F} g_{k'} \tag{2.7}$$

or we can write it as

$$g_k = V \frac{\sum g_{k'}}{2\epsilon_k - E} \tag{2.8}$$

Summing both sides and canceling the common factor, we have

$$\frac{1}{V} = \sum_{k > k_F} (2\epsilon_k - E)^{-1} \tag{2.9}$$

When replacing the summation by an integration, the above equation becomes

$$\frac{1}{V} = N(0) \int_{E_F}^{E_F + \hbar\omega_c} \frac{d\epsilon}{2\epsilon - E} = \frac{1}{2} N(0) \ln \frac{2E_F - E + 2\hbar\omega_c}{2E_F - E} \tag{2.10}$$

where $N(0)$ represents the density of states at the Fermi level for electrons of one spin orientation. For most conventional superconductors, $N(0)V < 0.3$ which is in the so-called weak-coupling limit, defined by $N(0)V \ll 1$. Therefore, the solution of Eq. 2.10 can be written as

$$E \approx 2E_F - 2\hbar\omega_c e^{-2/N(0)V} \tag{2.11}$$

This remarkable result tells us that the pair state we constructed with two electrons having $k > k_F$ will always have a lower energy than twice the normal

ground state Fermi energy ($2E_F$), no matter how weak the attractive interaction (V) is. This is why we say the normal ground state of an electron gas is unstable with respect to the formation of at least one bound pair. Cooper suggested that this instability is related to the formation of the superconducting state.

In conventional superconductors, the attractive interaction between the electrons has been demonstrated to originate from electron-phonon coupling [12–14].

2.3 BCS theory

We have shown that if an attractive interaction exists, regardless of how weak it is, the ground state Fermi sea exhibits instability against the formation of as least one bound pair. Clearly a new equilibrium point characterized by the condensation of numerous electron pairs is expected. When the ground state Fermi sea is greatly changed and the binding energy for an additional pair goes to zero, this new equilibrium point can be reached, and a new phase dominates the ground state of the system. However, the number of electrons involved in the phase transition is so large that it would be very difficult to deal with such a complicated state.

An essential step to describe this state is to seek a wavefunction. The theory proposed by Bardeen, Cooper and Schrieffer [1, 2] constructed a ground state in which all electrons are bound into pairs. In order to describe these pair states, the BCS theory introduced a "pair creation operator":

$$b_{\mathbf{k}}^{*} = c_{\mathbf{k}\uparrow}^{*} c_{-\mathbf{k}\downarrow}^{*} \tag{2.12}$$

and corresponding "pair annihilation operator":

$$b_{\mathbf{k}} = c_{-\mathbf{k}\downarrow} c_{\mathbf{k}\uparrow} \tag{2.13}$$

where $c_{\mathbf{k}\uparrow}^{*}$ is the electron "creation operator" which creates an electron of momentum $\mathbf{k}$ and spin up. The electron "annihilation operator" $c_{\mathbf{k}\uparrow}$ empties the corresponding state.

The BCS theory argued that with so many particles involved, it would be a good approximation to use a Hartree self-consistent field or mean-field approach,

in which the occupancy of each pair state $\mathbf{k}$ depends only on the average occupancy of other states. Then the ground state BCS wave function can be written as

$$\psi_{BCS} = \prod_{\mathbf{k}} (u_{\mathbf{k}} + v_{\mathbf{k}} b^*_{\mathbf{k}}) \phi_0 \tag{2.14}$$

where ϕ_0 is the vacuum state with no particle present. $|u_{\mathbf{k}}|^2 + |v_{\mathbf{k}}|^2 = 1$ indicates that the probability of the pair $(\mathbf{k}\uparrow, -\mathbf{k}\downarrow)$ being occupied is $|v_{\mathbf{k}}|^2$, whereas the probability that it is unoccupied is $|u_{\mathbf{k}}|^2 = 1 - |v_{\mathbf{k}}|^2$.

The BCS also considered a reduced Hamiltonian

$$H_{red} = 2 \sum_{k>k_F} \xi_k b^*_k b_k + 2 \sum_{k<k_F} |\xi_k| b_k b^*_k - \sum_{kk'} V_{kk'} b^*_{k'} b_k \tag{2.15}$$

where $\xi_k = \epsilon_k - E_F$, representing the Bloch energy relative to the Fermi energy. The first two terms correspond to the kinetic energy while the third term to the interaction energy.

The ground state energy relative to the energy of the Fermi sea is given by

$$W = \langle \psi_{BCS} | H_{red} | \psi_{BCS} \rangle \tag{2.16}$$

and let

$$v_k^2 = h_k \tag{2.17}$$

then

$$u_k^2 = 1 - h_k \tag{2.18}$$

Therefore, we can obtain

$$W = 2 \sum_{k>k_F} \xi_k h_k + 2 \sum_{k<k_F} |\xi_k|(1 - h_k) - \sum_{k,k'} [h_k(1 - h_k) h_{k'}(1 - h_{k'})]^{\frac{1}{2}} V_{kk'} \tag{2.19}$$

by minimizing W with respect to h_k we can get

$$v_k^2 = h_k = \frac{1}{2} \left[1 - \frac{\xi_k}{(\Delta_k^2 + \xi_k^2)^{\frac{1}{2}}} \right] \tag{2.20}$$

and

$$u_k^2 = 1 - h_k = \frac{1}{2} \left[1 + \frac{\xi_k}{(\Delta_k^2 + \xi_k^2)^{\frac{1}{2}}} \right] \tag{2.21}$$

where

$$\Delta_k = \sum_{k'} V_{kk'}[h_{k'}(1-h_{k'})]^{\frac{1}{2}} \tag{2.22}$$

Δ_k is the minimum excitation energy, or energy gap. It will also become the order parameter in the phenomenological theory, having a phase factor $e^{i\varphi}$, where φ is the relative phase of u_k and v_k. If we neglect anisotropic effects and assume the the matrix element $V_{kk'}$ can be replaced by a constant average matrix element V for pairs in the region $-\hbar\omega_c < \epsilon < \hbar\omega_c$ and by zero outside this region, Eq. 2.22 becomes

$$\Delta = V \sum_{k'} [h_{k'}(1-h_{k'})]^{\frac{1}{2}} \tag{2.23}$$

By substituting Eq. 2.20 and Eq. 2.21 into Eq. 2.23, we obtain

$$\frac{\Delta}{V} = \sum_{k'} \frac{\Delta_{k'}}{2\sqrt{\xi_{k'}^2 + \Delta_{k'}^2}} \tag{2.24}$$

here since $\Delta_k = \Delta$ for $|\xi| < \hbar\omega_c$ and $\Delta_k = 0$ for $|\xi| > \hbar\omega_c$, this equation can be simplified

$$\frac{1}{V} = \sum_{k'} \frac{1}{2\sqrt{\xi_{k'}^2 + \Delta^2}} \tag{2.25}$$

replacing the summation by an integration, the above equation becomes

$$\frac{1}{N(0)V} = \int_0^{\hbar\omega_c} \frac{d\xi}{\sqrt{\xi^2 + \Delta^2}} \tag{2.26}$$

consequently, we get

$$\Delta = \frac{\hbar\omega_c}{\sinh[\frac{1}{N(0)V}]} \approx 2\hbar\omega_c e^{-\frac{1}{N(0)V}} \tag{2.27}$$

The last step in the above equation is obtained in the weak-coupling limit, i.e. $N(0)V \ll 1$.

The BCS theory deduces several consequences, for example, the critical temperature is given by

$$k_B T_c = 1.13\hbar\omega_c e^{-\frac{1}{N(0)V}} \tag{2.28}$$

The exponential dependence explains the very low superconducting critical temperatures. $\hbar\omega_c$ is of order $k_B\Theta_D$, where Θ_D is the Debye temperature. But the

critical temperature is one to three orders of magnitude below the Debye temperature. The ratio of Eq. 2.27 to Eq. 2.28 yields a fundamental formula independent of the phenomenological parameters:

$$\frac{\Delta}{k_B T_c} = 1.76 \tag{2.29}$$

This result holds for a large number of superconductors to within about 10 percent. But it fails for lead, mercury and high-T_c superconductors, implying that these superconductors go beyond the weak-coupling limit.

2.4 The superconducting gap

In the superconducting state, there is no zero excitation energy. If we create a single particle excitation state at $k \uparrow$ in the superconducting state, the excitation energy is demonstrated to be

$$E_k = \sqrt{\xi_k^2 + \Delta^2} \tag{2.30}$$

where $\xi_k = \epsilon_k - E_F$ is the single-particle energy relative to the Fermi energy. Δ plays the role of an energy gap and is always referred to as the superconducting gap. It denotes the minimum excitation energy in the superconducting state, even at the Fermi surface, $\xi_k = 0$, $E_k = \Delta > 0$.

We can calculate the density of states for excited quasiparticles. Let $N(0)$ be the density of states at the Fermi level for electrons. The number of electronic states in the energy interval from ξ to $\xi + d\xi$ near the Fermi surface is given by $N(0)d\xi$. Hence the number of excited quasiparticles in the energy interval from E to $E + dE$ can be calculated as

$$\rho(E)dE = N(0)\frac{d\xi}{dE}dE = \frac{N(0)}{dE/d\xi}dE \tag{2.31}$$

combined with Eq. 2.30, we obtain

$$\rho(E)dE = N(0)\frac{E}{\sqrt{E^2 - \Delta^2}}dE \quad (E \geq \Delta) \tag{2.32}$$

Figure 2.4 shows the density of states for excited quasiparticles.

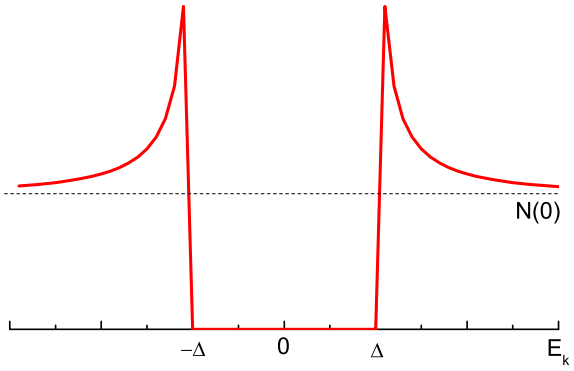

Figure 2.4: Density of states for BCS excited quasiparticles.

In the superconducting state, to break a Cooper pair and create two excitation states at k_i and k_j, one needs an excitation energy given by

$$E = \sqrt{\xi_{k_i}^2 + \Delta^2} + \sqrt{\xi_{k_j}^2 + \Delta^2} \tag{2.33}$$

when $\xi_{k_i} = \xi_{k_j} = 0$, the above equation yields the minimum excitation energy 2Δ. This result indicates that the minimum energy that can break a Cooper pair is 2Δ.

As we have discussed in previous sections, superconductivity is characterized by critical temperature, field and current. This means that Cooper pairs in a superconductor can be broken with thermal, magnetic and electrical energies. Certainly, Cooper pairs can also be broken with electromagnetic radiation. When the energy of the electromagnetic radiation is lower than 2Δ, Cooper pairs in a superconductor are not broken, thus no absorption can be observed. Once the energy of the electromagnetic radiation exceeds 2Δ, an absorption edge is present at 2Δ, indicating that Cooper pairs are broken. The magnitude of the superconducting gap is of a few meV, falling into the infrared frequency range of the optical spectrum. Therefore, the superconducting gap can be measured with infrared optical spectroscopy.

In the above paragraphs, we have discussed the superconducting gap in the BCS ground state ($T = 0$). Indeed, the superconducting gap exhibits strong temperature dependence. When finite temperatures are taken into account, the

generic gap equation becomes

$$\Delta_k = -\sum_{k'} V_{kk'} \frac{\Delta_{k'}}{2E_{k'}} \tanh \frac{E_{k'}}{2k_B T} \tag{2.34}$$

This generic equation will be very important when we discuss the pairing symmetry in unconventional superconductors (Section 2.7). For now, let's consider the BCS isotropic approximation, Eq. 2.34 reduces to

$$\frac{1}{N(0)V} = \int_0^{\hbar\omega_c} \frac{\tanh \frac{1}{2}\beta\sqrt{\xi^2+\Delta^2}}{\sqrt{\xi^2+\Delta^2}} d\xi \tag{2.35}$$

where $\beta = \frac{1}{k_B T}$. Using this equation, the gap value as a function of temperature $\Delta(T)$ can be computed numerically. For weak-coupling superconductors, $\Delta(T)$ decreases monotonously from $\Delta(0)$ at $T = 0$ to zero at T_c with increasing temperature. Figure 2.5 shows the calculated temperature dependence of the

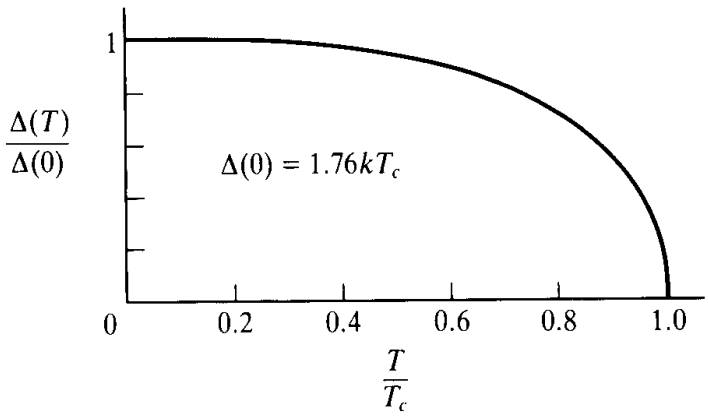

Figure 2.5: Temperature dependence of the superconducting gap in BCS theory. Adopted from Ref. [15].

superconducting gap. Below $\sim T_c/2$, $\Delta(T)$ decreases slowly as the temperature increases. When approaching T_c, the gap value falls steeply approximately as

$$\frac{\Delta(T)}{\Delta(0)} \approx 1.74(1 - \frac{T}{T_c})^{\frac{1}{2}} \quad \text{for} \quad T \approx T_c \tag{2.36}$$

2.5 Two-band superconductivity

The BCS theory successfully formulated the microscopic mechanism of the single band superconductivity. Suhl et al. extended the BCS theory to the case where two bands with more or less itinerant electrons overlap [16]. In the BCS theory, a net attractive interaction between two electrons can bind these two electrons into pair (Cooper pair), and the condensate of these Cooper pairs is responsible for the superconductivity. In a two-band system, considering Band 1 and Band 2. The interaction between electrons may happen in two ways: (i) intraband interaction, which means that the two electrons interact within the same band; (ii) interband interaction, signifying that the two electrons interacting are in different bands (one is in Band 1, the other is in Band 2).

The part of the Hamiltonian which connects pairs with zero net momentum takes the form

$$\begin{aligned} H = & 2\sum_{k}\xi_{k1}b_k^*b_k + 2\sum_{k}\xi_{k2}d_k^*d_k \\ & - V_{11}\sum_{kk'}b_k^*b_{k'} - V_{22}\sum_{kk'}d_k^*d_{k'} - V_{12}\sum_{kk'}(b_k^*d_{k'} + d_k^*b_{k'}) + \text{C.C.} \end{aligned} \tag{2.37}$$

where ξ_{k1} and ξ_{k2} are the Bloch energies in the two bands measured relative to the Fermi energy E_F. b_k, b_k^*, d_k, and d_k^* are the corresponding pair creation and annihilation operators. V_{11} (V_{22}) denotes the averaged interaction energy between two electrons those are both in Band 1 (Band 2). V_{12} is the averaged interaction energy between two electrons which are separately in Band 1 and Bang 2. Comparing this Hamiltonian to the BCS case, one can notice that we have two independent BCS Hamiltonians, one for each band, and one extra term to account for interband interaction. Within the framework of this theory, the transition temperature is found to be

$$k_BT_c = 1.14\hbar\omega_c\exp\Big\{-\Big[\frac{[\frac{V_{12}^2}{N_1N_2} + \frac{1}{4}(\frac{V_{22}}{N_1} - \frac{V_{11}}{N_2})^2]^{\frac{1}{2}}}{V_{12}^2 - V_{11}V_{22}} - \frac{\frac{1}{2}(\frac{V_{22}}{N_1} + \frac{V_{11}}{N_2})}{V_{12}^2 - V_{11}V_{22}}\Big]\Big\} \tag{2.38}$$

When $V_{12} = 0$, the interaction occurs between electrons in the same band, no interband pairing comes about. The two bands dominate the entire system

separately. Hence, there are two transition temperatures and two superconducting gaps. Each gap has its own value and closes at its corresponding transition temperature. The two solid parallel curves in Fig. 2.6 illustrate this case. When

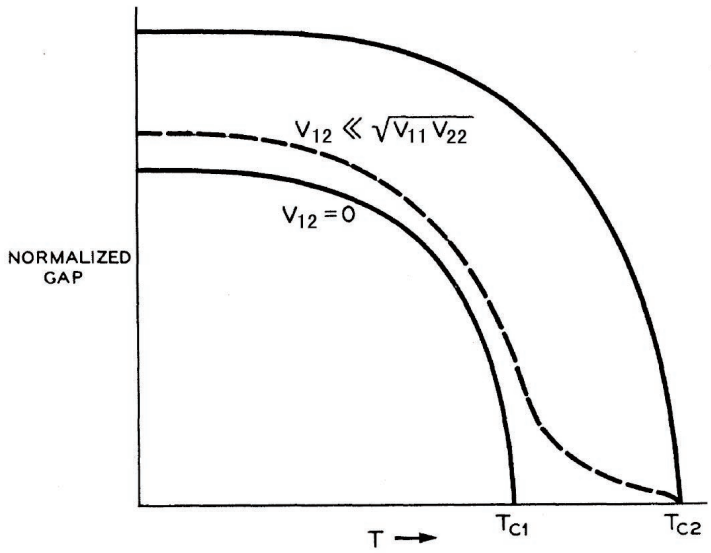

Figure 2.6: Temperature dependence of the superconducting gaps for two-gap superconductivity. Adopted from Ref. [16].

V_{12} is finite but much less than $\sqrt{V_{11}V_{22}}$, interband pairing arises. The small gap is lift up, and the lower transition temperature joins the higher, shown as the dashed curve in Fig. 2.6. Both bands have the same T_c.

Another effective limit is the case where $V_{11} = V_{22} = 0$, and $V_{12} \neq 0$. It represents the case of interband pairing only, and one can get superconductivity even without pairing in each individual band. The interband pairing only superconductivity exhibits the same transition temperature as BCS, with a density of states $(N_1N_2)^{1/2}$. Figure 2.7 shows the calculated temperature dependence of the superconducting gaps in this limit. One can see that there are still two gaps, closing at the same transition temperature.

2.6 Effects of impurities on superconductivity

In the superconducting state, Cooper pairs dominate the physical properties of a superconductor. Here we consider a superconductor containing impurities.

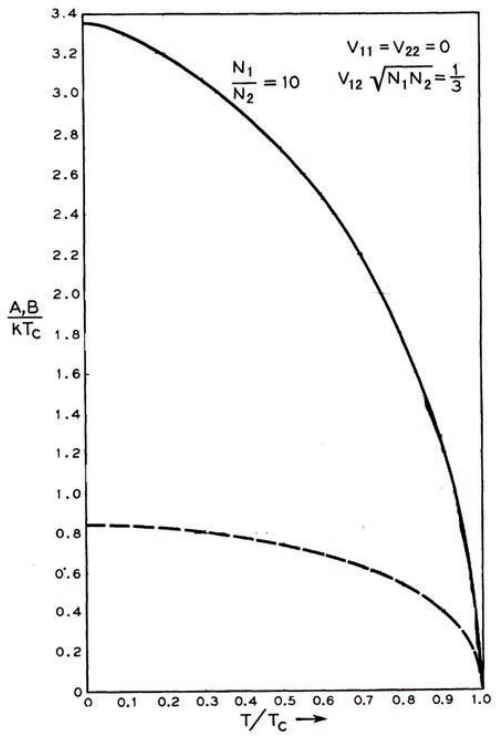

Figure 2.7: Calculated temperature dependence of the superconducting gaps for strong interband pairing case, using $V_{11} = V_{22} = 0$, $V_{12}\sqrt{N_1N_2} = \frac{1}{3}$, $N_1/N_2 = 10$. Adopted from Ref. [16].

Generally, impurities act only on the electric charge and scatter both electrons of a Cooper pair identically. This does not break the Cooper pair apart. However, magnetic impurities have a significant effect on superconductivity. As they can not only scatter the electron as ordinary impurities but also flip the electron spin. When scattered by an magnetic impurity, the Cooper pair can pass to a state with parallel spins (triplet state). The BCS theory requires that the electrons which are bound into pair have the antisymmetric singlet spin wave function, therefore, the pair is broken up.

Abrikosov and Gorkov investigated the effects of magnetic impurities on the superconducting transition temperature and energy gap [17]. They demonstrated that the presence of magnetic impurities in superconductors can significantly suppress the transition temperature. At low impurity concentration, T_c is given

by

$$T_c \approx T_{c0} - \frac{\pi\hbar}{4\tau_s} \tag{2.39}$$

where T_{c0} is the transition temperature of a pure superconductor. $1/\tau_s$ represents the scattering rate associated only with the exchange interaction and it is proportional to the concentration of the magnetic atoms. From this equation we see that, at low impurity concentrations the transition temperature decreases proportionally to the concentration. Obviously, one can find a critical concentration at $\hbar\tau_s^{-1} \sim T_{c0}$, where the transition temperature vanishes, indicating that the superconductivity is killed by magnetic impurities.

The properties of the superconducting gap is also severely affected by magnetic impurities. The most prominent character is that the superconducting gap vanishes at a critical concentration n'_m which is given by

$$n'_m \approx 0.91 n_{mc} \tag{2.40}$$

where n_{mc} is the critical concentration at which $T_c = 0$. Clearly, the critical magnetic impurity concentration that annihilates the superconducting gap is lower than the one killing the transition temperature. This fact indicates the existence of gapless superconductivity in the concentration range

$$0.91 n_{mc} < n'_m < n_{mc} \tag{2.41}$$

which is also supported by experimental results [18].

2.7 Pairing symmetry

A crucial issue in the mechanism of superconductivity is understanding the properties of the superconducting gap(s). All experimental and theoretical studies so far have confirmed that in the superconducting state, the excited levels are separated from the ground state by an energy 2Δ. It means that an energy gap opens centered about the Fermi energy. This energy gap is as the magnitude of the order parameter of the superconducting phase transition and shows remarkably different properties in different classes of superconductors. Figure 2.8 shows a schematic picture of the superconducting order parameter in different cases.

In conventional BCS superconductors, such as aluminium, only one band crosses the Fermi level and participates the superconducting condensation. Upon entering the superconducting state, an isotropic gap opens near the Fermi surface which means that the gap value and the sign are invariable at every point of the Fermi surface. This is the case of an s-wave gap as shown in panel (a) of Fig. 2.8. Here the two-dimensional Fermi surface is approximated by one circle.

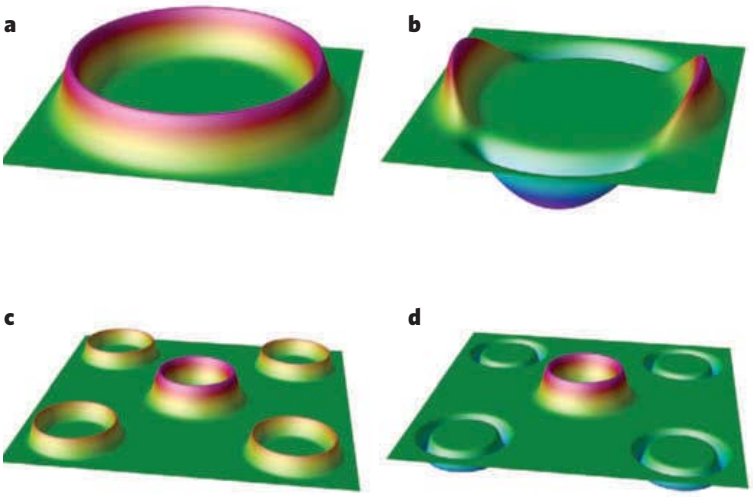

Figure 2.8: A schematic representation of the superconducting order parameter in different cases from Ref. [19]. (a) an s-wave in conventional superconductors; (b) a d-wave, as is the case in copper oxides; (c) a two-band s-wave with the same sigh, as in MgB_2; (d) an $s_{\pm}$ wave, as is proposed to be the case in iron-based superconductors. In all cases, the height of the "rubber sheet" is proportional to the magnitude of the order parameter (including its sign).

In the BCS approximation, by definition, the superconducting gap and the interaction potential are isotropic, i.e. they do not depend on k. Interesting possibilities arrive when this approximation is not made. Taking the full temperature dependent gap equation (Eq. 2.34), one can see that pairing can occur even if the interaction potential $V_{kk'}$ is not attractive, i.e. $V_{kk'} > 0$. In that case, the self consistent gap equation still has a solution as far as the gap can change sign, which means that Δ_k and $\Delta_{k'}$ have different signs for significant portions

of the k space. This is particularly important as it allows for an "all electronic" pairing mechanisms such as spin fluctuations. Examples of sign changing order parameters are the $d_{x^2-y^2}$ symmetry observed in cuprates and the $s_{\pm}$ symmetry proposed for pnictides.

In the case of a d-wave symmetry order parameter, found in the copper oxide superconductors [20], the gap function for pair state can be written as $\Delta(k) = \Delta_0(\cos k_x - \cos k_y)$, where Δ_0 is the maximum gap value, k_x and k_y are the wave-vector components along the principal axes in the two-dimensional k space. As indicated by the d-wave gap function, in the (π, 0) direction of the two-dimensional k space, the gap value reaches a maximum, and nodes exist in the (π, π) direction, moreover, the sign of the order parameter changes at the nodes. See panel (b) in Fig. 2.8.

In contrast to the conventional superconductors and the copper oxides, MgB_2 has a more complex electronic structure, featuring two distinctively different groups of electrons. These two groups of electrons form two kinds of electronic band, which give rise to two separate sets of Fermi surfaces [21]. Hence, MgB_2 is referred to as two-band superconductors. The order parameter in each band has an s-wave symmetry and the same sign. A schematic picture of this case can be seen in panel (c) of Fig. 2.8, and the Fermi surface is approximated by a small circle in the center (the first band) surrounded by four larger circles (the second band).

The case of the newly discovered iron-based superconductors is unlike any of the preceding ones. Electronic structure calculations predict that up to five bands at the Fermi level participate in the formation of the superconducting condensate [22, 23], leading to multigap superconductivity. Mazin et al. [24] suggested an antiferromagnetic spin fluctuation mediated superconductivity in these materials resulting in a possible sign reversal between the order parameters in different Fermi surface sheets, in the so-called $s_{\pm}$ pairing symmetry shown in panel (d) of Fig. 2.8. In other words, each band would have an isotropic gap (such as in MgB_2), but their relative phases would be opposite. Additionally, in a process similar to pair breaking by magnetic impurities in a BCS superconductor

(see Sec. 2.6), pairs can be broken by *non-magnetic* impurity scattering in the $s_{\pm}$ symmetry. Such scattering mixes states with opposite phases, and Cooper pairs are annihilated. An excess of unpaired quasiparticles will thus appear in the superconducting state [25, 26].

2.8 High-T_c superconductors

This thesis is not about cuprates. However, many of the relevant points observed in pnictides have a close relation to the response of cuprates. Here we present a brief overview of copper oxide based superconductivity.

More than 20 years ago, superconductivity with a transition temperature of 35 K was discovered by Bednorz and Mueller in a lanthanum-based cuprate material (Ba-La-Cu-O) [3]. Soon after their discovery, a large number of compounds with similar structure were found to exhibit superconductivity. The superconducting transition temperature was raised above the boiling point of liquid nitrogen (77 K) by this class of superconductors. For example, Y-Ba-Cu-O shows a transition temperature of 92 K [27], and the T_c of the Hg-Ba-Ca-Cu-O system can reach $\sim$ 133 K [28] which can be pushed over 150 K under extremely high pressure [29, 30]. The cuprate superconductors are always referred to as "High-T_c superconductors" on account of their relatively high transition temperatures compared to the BCS superconductors. This class of superconductors are highly structurally and electronically anisotropic compounds and have the perovskite structure. Copper oxide planes characterize the cuprate superconductors and are responsible for superconductivity.

The undoped materials are called parent compounds of the family. Superconductivity arises from doping the parent compounds with holes or electrons. Figure 2.9 shows the schematic electronic phase diagram of the copper oxide superconductors. At zero doping fraction, although the energy band of the parent compounds is half-filled, the strong Coulomb repulsion prevents electrons from hoping between nearest Cu atoms. Consequently, these materials are antiferromagnetic insulators (Mott insulators) in the ground state instead of half-filled metals. When doping the parent compounds with holes or electrons, the long-range magnetic order is completely suppressed and then superconductivity

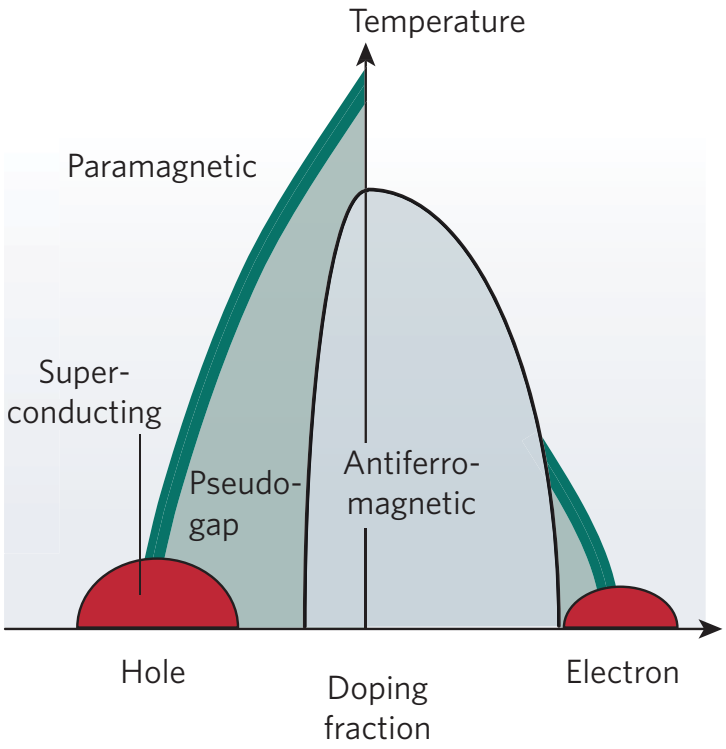

Figure 2.9: Schematic phase diagram of copper oxide superconductors. Adopted from Ref. [19]

emerges, shown as the red domes on both the hole and electron doping sides. In the T vs doping diagram for each family of superconductors, the compounds having the highest T_c are named "optimally doped", which is represented by the apex of the superconducting domes in the phase diagram. The compounds with carrier concentrations lower (higher) than the optimally doped ones are named underdoped (overdoped) compounds.

The copper oxide superconductors exhibit numerous unconventional properties that can not be explained by the BCS theory. For instance: (i) The transition temperature exceeds ~ 30 K, the maximum T_c predicted by BCS theory; (ii) Electron-phonon coupling fails in accounting for the pairing mechanism; (iii) The weak-coupling approximation is not valid. (iv) the superconducting gap shows

an unconventional *d*-wave symmetry; (v) A resonant spin excitation, localized in both energy and wavevector, is universally observed within superconducting phase [31–34]. Cooper pairs might be mediated by spin fluctuation.

At low doping fractions (underdoped region), the cuprates furthermore exhibit a second energy scale, characterized by a depletion of electronic and spin density of states at the Fermi level, which is observed at temperatures much higher than the superconducting transition temperature, the so-called pseudogap [35]. This pseudogap feature was first observed by nuclear magnetic resonance [36] and then was confirmed by a variety of techniques like angle resolved photoemission spectroscopy (ARPES) [37, 38], *c*-axis tunneling [39], and far infrared spectroscopy [40, 41]. However, the origin of the pseudogap phase in the cuprates and its relation with the superconductivity is still under heavy debate. The central issue is whether the pseudogap phase is intimately related to the superconducting gap like a precursor of pairing [42–47] or a competitive order that has no direct bearing on superconductivity [48–53].

Chapter 3

Infrared spectroscopy

This thesis relies heavily on the measurement and analysis of the optical properties of pnictide superconductors. Before dwelling into the physics of pnictides, let's set the ground to what the optical conductivity is sensitive to.

3.1 The interaction of radiation with matter

The beautiful colors of gemstones have been valued in all societies, and metals have been used for making mirrors for thousands of years. However, the scientific explanations for these phenomena have only been given in relatively recent times. Light, electromagnetic radiation having a vast spectrum from radiowaves via infrared, visible, ultraviolet, and x-rays to γ-rays, interacts with solids in many different ways. It can be absorbed or reflected by materials. Light propagating in medium may have different physical processes like refraction, scattering, interference and diffraction, then color arises. Besides, light shining onto a material may excite some of the electrons to energies sufficiently high, so these electrons can escape from the material. This process is called the photoelectric effect.

In a solid, a large number of atoms at the supramolecular and macromolecular scale interact strongly and adhere to each other. Many and various mysterious properties appear due to the multiple interactions in a many-body system. For instance, superconductivity exists in certain materials at low temperatures; spin-density-wave and charge-density-wave are exhibited as low-energy ordered states in anisotropic, low-dimensional materials. To describe and explain these properties in a condensed matter phase, energy band theory [54] and the collective excitations are introduced into condensed matter physics. The characteristic energy of the collective excitations in a solid locates in the energy interval from

several meV to several eV. For example, the energy of superconducting gaps is usually several meV; the phonon excitation energy is dozens to hundreds of meV; the band gap of semiconductors is about several eV. Light scattering is therefore an important tool to probe excitations in solids. Figure 3.1 illustrates some

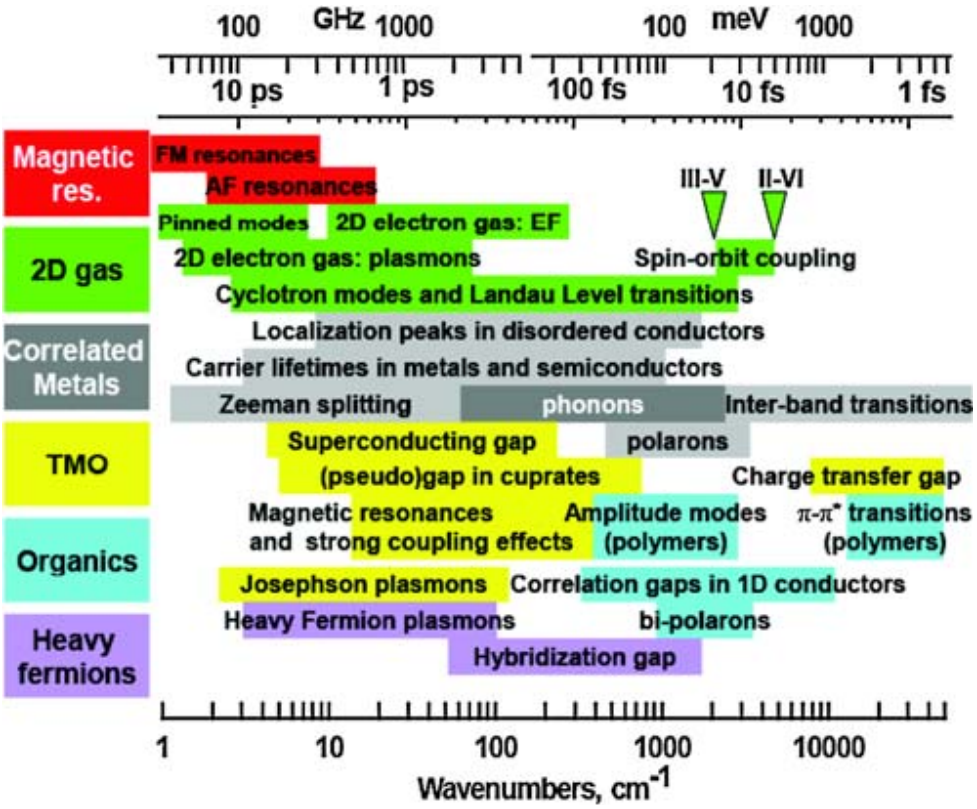

Figure 3.1: Schematic representation of characteristic energy scales in correlated electron systems. Adopted from Ref. [55].

characteristic energy scales in solids.

For some historical reasons, in infrared spectroscopy, we use wavenumber as the measurement of energy. Wavenumber (in unit cm^{-1}) is defined as $1/\lambda$, where λ is the wavelength. One can convert cm^{-1} into other units via the relations as

follows

$$8\ \mathrm{cm}^{-1} = 1\ \mathrm{meV}$$
$$33\ \mathrm{cm}^{-1} = 1\ \mathrm{THz}$$
$$100\ \mathrm{cm}^{-1} = 100\ \mu\mathrm{m}$$

With optical conductivity, one can probe electronic structure and excitations in the frequency range from $\sim 20\ \mathrm{cm}^{-1}$ to at least $55000\ \mathrm{cm}^{-1}$ corresponding to 2.5 meV to 6.9 eV. In this range, the far-infrared region is of the utmost importance to superconductivity, since it covers both the superconducting gap and the energies of the excitations believed to be relevant to the formation of the superconducting condensation.

Compared to other techniques, infrared spectroscopy has its own characteristics: (i) The frequency of the outgoing light does not shift with respect to the incident light. Only the phase shift and attenuation of the light are recorded. So infrared spectroscopy is referred to as elastic light scattering probe. This is opposite to Raman spectroscopy which is a widely known inelastic light scattering technique. (ii) It's a momentum averaged technique. Unlike the ARPES (angle-resolved photoemission spectroscopy) or neutron scattering, infrared spectroscopy does not have momentum resolution, thus can not provide information on k dependence. (iii) It has a penetration depth of a few hundred nanometers, much longer than ARPES (several unit cells) and STM, representing a bulk sensitive probe. (iv) The electric field dominates the interaction between the light and materials.

3.2 Electrodynamics

3.2.1 Maxwell's equations

The theoretical description of the interaction of electromagnetic radiation with matter and the analysis of the experimental results are based on Maxwell's equations written as:

$$\nabla \cdot \mathbf{D} = \rho \tag{3.1}$$

$$\nabla \times \mathbf{H} - \frac{\partial \mathbf{D}}{\partial t} = \mathbf{J} \tag{3.2}$$

$$\nabla \times \mathbf{E} + \frac{\partial \mathbf{B}}{\partial t} = 0 \tag{3.3}$$

$$\nabla \cdot \mathbf{B} = 0 \tag{3.4}$$

D Electric displacement vector
H Magnetic field vector
E Electric field
B Magnetic induction
J Current density
ρ Charge density

3.2.2 Solution of Maxwell's equations in vacuum

In a vacuum and in the absence of free current and external charge ($\mathbf{J} = 0$ and $\rho = 0$), $\mathbf{D} = \epsilon_0\ \mathbf{E}$ and $\mathbf{B} = \mu_0\ \mathbf{H}$. The two equations Eq. 3.1 and Eq. 3.2 becomes:

$$\nabla \cdot \mathbf{E} = 0 \tag{3.5}$$

$$\nabla \times \mathbf{B} - \frac{1}{c^2}\frac{\partial \mathbf{E}}{\partial t} = 0 \tag{3.6}$$

The combination of Eq. 3.3 and Eq. 3.6 yields:

$$\nabla^2 \mathbf{E} - \frac{1}{c^2}\frac{\partial^2 \mathbf{E}}{\partial t^2} = 0 \tag{3.7}$$

This is a wave equation in its simplest form without dissipation, and the second spatial derivative is equal to the second derivative in time with the square of the velocity as proportionality factor. One possible solution of this differential equation is given by a harmonic wave:

$$\mathbf{E}(\mathbf{r}, t) = \mathbf{E}_0 e^{-i(\mathbf{k}\cdot\mathbf{r} - \omega t)} \tag{3.8}$$

where **k** is the wavevector. The corresponding wave equation for **H** can easily be derived from Maxwell's equations:

$$\nabla^2 \mathbf{H} - \frac{1}{c^2}\frac{\partial^2 \mathbf{H}}{\partial t^2} = 0 \tag{3.9}$$

and has the same form of solution:

$$\mathbf{H}(\mathbf{r},t) = \mathbf{H}_0 e^{-i(\mathbf{k}\cdot\mathbf{r}-\omega t-\phi)} \tag{3.10}$$

A phase factor ϕ is included to indicate that the electric and magnetic fields may be shifted in phase with respect to each other.

3.2.3 Propagation of electromagnetic wave in the medium

Because we are interested in the optical properties of solids, we now have to discuss the influence of matter on the propagation of the electromagnetic wave. First it's always a good start to define some material parameters and see how they enter Maxwell's equations.

The presence of a medium in electric and magnetic fields may lead to electric dipoles and magnetic moments; polarization charges, and induced current. To differentiate these effects, we artificially separate the electrons into bound electrons and free electrons in the system. we assume that there is no external current present: $\mathbf{J}_{ext} = 0$. Then the total current density $\mathbf{J}_{total}$ entering Maxwell's equation consists of a contribution from the motion of free electrons in the presence of an electric field ($\mathbf{J}_{cond}$) and of a contribution $\mathbf{J}_{bound}$ arising from the redistribution of bound charges:

$$\mathbf{J}_{total} = \mathbf{J}_{cond} + \mathbf{J}_{bound} \tag{3.11}$$

Another complication in dealing with the interaction of electromagnetic wave with matter is that the electric and magnetic fields will not be uniform within the material but fluctuate from point to point reflecting the periodicity of the atomic lattice. However, for wavelengths appreciably longer than (i) the atomic distance and (ii) the mean free path of the free electrons, we can nevertheless consider an average value of the electric and magnetic fields (local approximation). Furthermore, we consider that the luminous flux used for experiment is very weak, then the response of the system is proportional to the perturbation. This method is referred to as the linear approximation. Based on these approximations, it's reasonable to describe the effects of the electromagnetic radiation on a medium

as follows:

$$\mathbf{P} = \chi_e^b \epsilon_0 \mathbf{E} \tag{3.12}$$

$$\mathbf{M} = \chi_m \mu_0 \mathbf{H} \tag{3.13}$$

$$\mathbf{J}_{cond} = \sigma_1^f \mathbf{E} \tag{3.14}$$

$$\rho_{total} = \rho_{ext} + \rho_{pol} \tag{3.15}$$

where ϵ_0 and μ_0 are the permittivity and permeability of free space respectively, and c is the speed of light in vacuum which is equal to $1/\sqrt{\epsilon_0 \mu_0}$.
$\mathbf{P}$ is the electric polarization density (the dipole moment per unit volume);
$\mathbf{M}$ is the magnetization (the magnetic moment density);
$\mathbf{J}_{cond}$ is the current density contribution from the free electrons;
σ_1^f is the conductivity of the free electrons;
ρ_{ext} is an external charge density;
ρ_{pol} is the charge density due to the spatially varying polarization;
χ_e is the dielectric susceptibility;
χ_m is the magnetic susceptibility.

In the absence of external charge $\rho_{ext} = 0$. For a homogeneous polarization, the positive and negative charges cancel everywhere inside the material, leading to no net charge ρ_{pol} in the condition of the long wavelength limit. The electric field $\mathbf{E}$ and the electric displacement vector (or electric flux density) $\mathbf{D}$ are connected by:

$$\mathbf{D} = \epsilon_0 \mathbf{E} + \mathbf{P} = (1 + \chi_e^b)\epsilon_0 \mathbf{E} \equiv \epsilon^b \epsilon_0 \mathbf{E} \tag{3.16}$$

where ϵ^b is dielectric function of the bound electrons.

The magnetic field $\mathbf{H}$ and the the magnetic induction $\mathbf{B}$ are connected by:

$$\mathbf{B} = \mu_0 \mathbf{H} + \mathbf{M} = (1 + \chi_m)\mu_0 \mathbf{H} \equiv \mu \mu_0 \mathbf{H} \tag{3.17}$$

where μ is the magnetic permeability.

The quantities χ_e^b, ϵ^b, χ_m, and μ which connect the fields are unitless. The magnetic susceptibility χ_m is typically four to five orders of magnitude smaller (except in the case of ferromagnetism) than the dielectric susceptibility χ_e which

is of the order of unity. For this reason, when electromagnetic waves pass through a medium, the dia- and para-magnetic properties can in general be neglected compared to the dielectric properties. Since we are not going to discuss the properties of magnetic materials, we suppose $\mu = 1$ in this thesis.

With these definitions above, we can rewrite Maxwell's equations Eq. 3.1 - Eq. 3.4 in the presence of matter:

$$\nabla \cdot (\epsilon^b \epsilon_0 \mathbf{E}) = 0 \tag{3.18}$$

$$\nabla \times \mathbf{H} = \frac{\partial(\epsilon^b \epsilon_0 \mathbf{E})}{\partial t} + \sigma^f \mathbf{E} \tag{3.19}$$

$$\nabla \times \mathbf{E} = -\frac{\partial(\mu_0 \mathbf{H})}{\partial t} \tag{3.20}$$

$$\nabla \cdot (\mu_0 \mathbf{H}) = 0 \tag{3.21}$$

We consider an infinite medium to avoid boundary and edge effects. As we did in the case of vacuum, the solution can be written as:

$$\mathbf{E}(\mathbf{r}, t) = \mathbf{E}_0(\mathbf{r}, \omega) e^{-i\omega t} \tag{3.22}$$

$$\mathbf{H}(\mathbf{r}, t) = \mathbf{H}_0(\mathbf{r}, \omega) e^{-i\omega t - \phi} \tag{3.23}$$

(i) We can calculate the rotation ($\nabla\times$) of the two terms of Eq. 3.20:

$$\nabla \times (\nabla \times \mathbf{E}) = \nabla \times (-\frac{\partial(\mu_0 \mathbf{H})}{\partial t}) \tag{3.24}$$

$$\nabla(\nabla \cdot \mathbf{E}) - \nabla^2 \mathbf{E} = i\omega \nabla \times \mathbf{H} \tag{3.25}$$

Note that $\nabla \cdot \mathbf{E} = 0$ ($\epsilon^b \neq 0$) in Eq. 3.18, the equation 3.25 is then equal to:

$$-\nabla^2 \mathbf{E} = i\omega \nabla \times \mathbf{H} \tag{3.26}$$

(ii) We calculate the derivative with respect to time ($\frac{\partial}{\partial t}$) of the two terms in the equation 3.19:

$$i\omega \nabla \times \mathbf{H} = i\omega\mu_0(\sigma^f \mathbf{E} - i\omega\epsilon^b \epsilon_0 \mathbf{E}) \tag{3.27}$$

By comparing Eq. 3.26 and Eq. 3.27, we obtain:

$$-\nabla^2 \mathbf{E} = \frac{\omega^2}{c^2} \mathbf{E}[\epsilon^b + \frac{i\sigma^f(\omega)}{\epsilon_0 \omega}] = \frac{n^2 \omega^2}{c^2} \mathbf{E} = \mathbf{k}^2 \mathbf{E} \tag{3.28}$$

This equation has the general form of a wave equation. If we define the complex dielectric function ($\epsilon(\omega)$) as:

$$\epsilon(\omega) = [\epsilon^b + \frac{i\sigma^f(\omega)}{\epsilon_0\omega}] \tag{3.29}$$

This complex dielectric function $\epsilon(\omega)$ can characterize the optical response of all the charges in the system, including the free and bound charges. In this case, we can redefine $\epsilon^b \to \epsilon^b + \delta\epsilon^b$ on condition that we redefine $\sigma^b \to \sigma^b + i\omega\delta\epsilon_0\epsilon^b$. Finally we obtain:

$$\epsilon(\omega) = 1 + i\frac{\sigma(\omega)}{\epsilon_0\omega} \tag{3.30}$$

We choose the complex dielectric function $[\epsilon(\omega) = \epsilon_1 + i\epsilon_2]$ to describe the optical response of the material. However, it's intimately related to other optical functions; therefore all other complex optical functions consists of the same information.

3.3 Optical constants

The complex refractive index is defined as:

$$\hat{N} = n + ik = \sqrt{\epsilon(\omega)} \tag{3.31}$$

which can be decomposed into the real part:

$$n(\omega) = \sqrt{\frac{\sqrt{\epsilon_1^2(\omega) + \epsilon_2^2(\omega)} + \epsilon_1(\omega)}{2}} \tag{3.32}$$

and the imaginary part (the extinction coefficient):

$$k(\omega) = \sqrt{\frac{\sqrt{\epsilon_1^2(\omega) + \epsilon_2^2(\omega)} - \epsilon_1(\omega)}{2}} \tag{3.33}$$

If we consider the case of the normal incidence, the wavevector is perpendicular to the surface while **E** and **H** point in the x and y directions, respectively. At the interface between the two different media 1 and 2, the complex reflection coefficient (r) can be written as:

$$r_{12} = \sqrt{R_{12}}e^{i\phi_r} = \frac{\hat{N}_1 - \hat{N}_2}{\hat{N}_1 + \hat{N}_2} \tag{3.34}$$

where R_{12} is the reflectivity and ϕ_r is the phase shift of the reflected to incident wave. The transmission coefficient (t) is:

$$t_{12} = \sqrt{T_{12}} e^{i\phi_t} = \frac{2\hat{N}_1}{\hat{N}_1 + \hat{N}_2} \tag{3.35}$$

where T_{12} is the transmission with a phase change ϕ_t.

In this thesis, we discuss the optical properties of solids in vacuum where $\hat{N}$ = 1, hence the complex reflection coefficient (r) of the material is simplified as:

$$r = \sqrt{R(\omega)} e^{i\phi(\omega)} = \frac{1 - \hat{N}}{1 + \hat{N}} = \frac{1 - n(\omega) - ik(\omega)}{1 + n(\omega) + ik(\omega)} \tag{3.36}$$

where $n(\omega)$ and $k(\omega)$ are the index of refraction and the extinction coefficient of the material, respectively.

The complex optical conductivity $\sigma(\omega)$ can be derived from Eq. 3.30:

$$\sigma(\omega) = \sigma_1(\omega) + i\sigma_2(\omega) = i\epsilon_0\omega[1 - \epsilon(\omega)] \tag{3.37}$$

In the system of units of optical spectroscopy ($[\omega] = \mathrm{cm}^{-1}$ and $[\sigma_1] = \Omega^{-1}cm^{-1}$), the real part and the imaginary part of the optical conductivity are written as:

$$\sigma_1(\omega) = \frac{2\pi}{Z_0}\omega\epsilon_2(\omega) \tag{3.38}$$

$$\sigma_2 = \frac{2\pi}{Z_0}\omega[1 - \epsilon_1(\omega)] \tag{3.39}$$

where $Z_0 = \sqrt{\mu_0/\epsilon_0}$ is the vacuum impedance which equals 377 Ω.

Now we have introduced four pairs of optical constants, [$\epsilon_1(\omega)$, $\epsilon_2(\omega)$], [$n(\omega)$, $k(\omega)$], [$\sigma_1(\omega)$, $\sigma_2(\omega)$], and [$R(\omega)$, $\phi(\omega)$]. The complex dielectric constant [$\epsilon_1(\omega)$, $\epsilon_2(\omega)$] and the complex conductivity [$\sigma_1(\omega)$, $\sigma_2(\omega)$] can be regarded as the prime response functions of the material describing the electric polarization and current induced in response to the applied electric field. All the so-called optical constants introduced here are not constants, but generally depend on frequency ω. The frequency dependence of the response is called dispersion. Furthermore, all these quantities can be used as parameters for describing a material in interaction with light and can be deduced reciprocally from one pair to others via simple algebra.

3.4 Kramers-Kronig relations and sum rules

The various material parameters and optical constants introduced in the previous section describe the response of the medium to applied electromagnetic radiation within the framework of linear response theory. They are all complex response functions consisting of a real part (or amplitude) and an imaginary part (or phase). For example, the electromagnetic wave which is transmitted through an interface or reflected off a boundary of two materials is characterized by both the amplitude and the phase shifts (ϕ_t or ϕ_r); both components constitute a response function. Kramers and Kronig investigated the relations between the real and imaginary parts of the optical constants, and found that they are not independent. Causality can be used to derive important relations between the real and imaginary parts of the complex response functions. The relations first given by Kramers and Kronig were called Kramers-Kronig relations, KK relations for short. The Kramers-Kronig relations play an important role in experimental physics. They allow for the evaluation of the components of the complex dielectric constant or conductivity when only one optical parameter such as the reflected or absorbed power is measured. For instance, with $R(\omega)$ obtained over a broad frequency range, the KK relations can be utilized to evaluate $\phi_r(\omega)$.

These KK relations together with physical arguments about the behavior of the response in certain limits can also be used to derive sum rules.

3.4.1 Kramers-Kronig relations

The Kramers-Kronig relations are based on the principle of causality which means that a effect can only happen after rather than precede its cause. Under the action of an external stimulus, a system responds in its own characteristic way. The relationship of the response to the stimulus is given by a response function.

Considering a general linear response to an external perturbation given in the form of

$$\hat{X}(\mathbf{r},t) = \int\int_{-\infty}^{\infty} \hat{G}(\mathbf{r},\mathbf{r}',t,t')\hat{f}(\mathbf{r}',t')d\mathbf{r}'dt' \tag{3.40}$$

This equation describes the response $\hat{X}(\mathbf{r},t)$ of the system at location $\mathbf{r}$ and time t to an external stimulus $\hat{f}(\mathbf{r}',t')$ acting at all times t' and places $\mathbf{r}'$. The function $\hat{G}(\mathbf{r},\mathbf{r}',t,t')$ is called the response function.

Here the stimulus of interest will generally be an electromagnetic wave. We consider the situation in the long wave length limit and neglect the spatial dependence of the external perturbation as in the local approximation. We also assume that the medium is isotropic and homogeneous, and thus $\hat{G}$ is a scalar. With these assumptions, Eq. 3.40 becomes:

$$\hat{X}(t) = \int_{-\infty}^{\infty} \hat{G}(t-t')\hat{f}(t')dt' \tag{3.41}$$

If we include the additional requirement that the system be causal, indicating that there is no response prior the stimulus, then

$$\hat{G}(t-t') = 0 \quad \text{for} \quad t < t' \tag{3.42}$$

For further analysis, it is more convenient to make a Fourier transformation which can be written as

$$\hat{f}(\omega) = \int \hat{f}(t)\exp(i\omega t)dt \tag{3.43}$$

$$\hat{X}(\omega) = \int \hat{X}(t)\exp(i\omega t)dt \tag{3.44}$$

$$\hat{G}(\omega) = \int \hat{G}(t-t')\exp[i\omega(t-t')]dt \tag{3.45}$$

From Eq. 3.41 and Eq. 3.44, we get

$$\begin{aligned} \hat{X}(\omega) &= \int dt\exp(i\omega t)[\int \hat{G}(t-t')\hat{f}(t')dt'] \\ &= \int dt'\hat{f}(t')[\int \hat{G}(t-t')\exp(i\omega t)dt] \\ = \int dt'\hat{f}(t')\exp(i\omega t')\int \hat{G}(t-t')\exp[i\omega(t-t')]dt \end{aligned} \tag{3.46}$$

Substituting Eq. 3.43 and Eq. 3.45 for the right side of the above equation, we obtain

$$\hat{X}(\omega) = \hat{G}(\omega)\hat{f}(\omega) \tag{3.47}$$

Assuming that the frequency in the previous equations is complex, $\hat{\omega} = \omega_1 + i\omega_2$, then Eq. 3.45 becomes

$$\hat{G}(\hat{\omega}) = \int \hat{G}(t-t')\exp[i\omega_1(t-t')]\exp[-\omega_2(t-t')]dt \tag{3.48}$$

The second exponential term is bounded in the upper half of the complex plane for $t-t' > 0$ and in the lower half plane for $t-t' < 0$. Causality requires $\hat{G}(t-t')$ $= 0$ for $t - t' < 0$, hence $\hat{G}(\hat{\omega})$ is limited to the upper half of the $\hat{\omega}$ plane. We

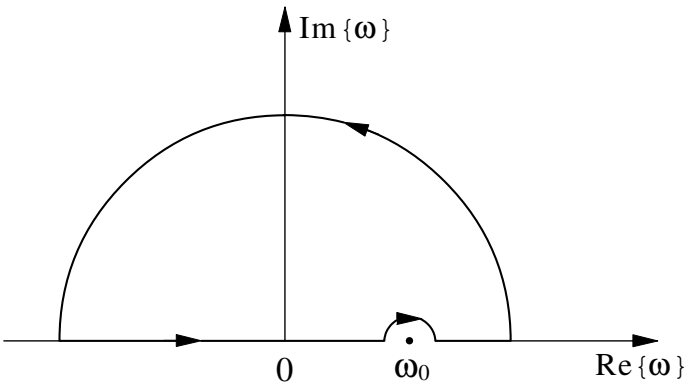

Figure 3.2: Integral contour in the complex frequency plane. The radius of the large semicircle is $|\hat{\omega}|$ and the small semicircle radius is η.

consider a integration contour shown in Fig. 3.2 with a small indentation near the frequency ω_0. Cauchy integral formula gives:

$$\oint \frac{\hat{G}(\hat{\omega}')}{\hat{\omega}' - \hat{\omega}_0} d\hat{\omega}' = 0 \tag{3.49}$$

If $\hat{G}(\hat{\omega}) \to 0$ when $|\hat{\omega}| \to \infty$, the integral over the large semicircle vanishes, only the integral along the real axis from $-\infty$ to ∞ remains, then

$$\int_{-\infty}^{\omega_0-\eta} \frac{\hat{G}(\omega')}{\omega' - \omega_0} d\omega' + \int_{\omega_0+\eta}^{\infty} \frac{\hat{G}(\omega')}{\omega' - \omega_0} d\omega' + \int_{\pi}^{0} \frac{\hat{G}(\omega_0 + \eta e^{i\phi})}{\eta e^{i\phi}} d(\omega_0 + \eta e^{i\phi}) = 0 \tag{3.50}$$

For $\eta \to 0$

$$\hat{G}(\omega) = \frac{1}{i\pi} \mathbf{P} \int_{-\infty}^{\infty} \frac{\hat{G}(\omega')}{\omega' - \omega} d\omega' \tag{3.51}$$

where **P** is the principal value. The complex response function $\hat{G}(\omega)$ can be written in terms of the real part and the imaginary part as $\hat{G}(\omega) = G_1(\omega) + iG_2(\omega)$, so the relations between the real and imaginary parts of the response function are obtained:

$$G_1(\omega) = \frac{1}{\pi}\mathbf{P}\int_{-\infty}^{\infty}\frac{G_2(\omega')}{\omega' - \omega}d\omega' \tag{3.52}$$

$$G_2(\omega) = -\frac{1}{\pi}\mathbf{P}\int_{-\infty}^{\infty}\frac{G_1(\omega')}{\omega' - \omega}d\omega' \tag{3.53}$$

From Eq. 3.45 we can see that $\hat{G}(-\omega) = \hat{G}^*(\omega)$, hence $G_1(\omega)$ is even and $G_2(\omega)$ is odd, then Eq. 3.52 and Eq. 3.53 can be written as

$$G_1(\omega) = \frac{2}{\pi}\mathbf{P}\int_{0}^{\infty}\frac{\omega' G_2(\omega')}{\omega'^2 - \omega^2}d\omega' \tag{3.54}$$

$$G_2(\omega) = -\frac{2\omega}{\pi}\mathbf{P}\int_{0}^{\infty}\frac{\omega' G_1(\omega')}{\omega'^2 - \omega^2}d\omega' \tag{3.55}$$

Using these general relations we can derive various expressions connecting the real and imaginary parts of different optical constants introduced in the previous section. For example, applying these relations to the complex optical conductivity $\hat{\sigma}(\omega) = \sigma_1(\omega) + i\sigma_2(\omega)$ yields:

$$\sigma_1(\omega) = \frac{2}{\pi}\mathbf{P}\int_{0}^{\infty}\frac{\omega' \sigma_2(\omega')}{\omega'^2 - \omega^2}d\omega' \tag{3.56}$$

$$\sigma_2(\omega) = -\frac{2\omega}{\pi}\mathbf{P}\int_{0}^{\infty}\frac{\omega' \sigma_1(\omega')}{\omega'^2 - \omega^2}d\omega' \tag{3.57}$$

We can also derive the Kramers-Kronig relations connecting the real and imaginary parts for the complex dielectric function, the complex refractive index and the complex reflective coefficient. More detailed calculations are discussed in Ref. [56–58].

The most important Kramers-Kronig relation for optical investigations is the one between the reflectivity ($R(\omega)$) and the phase shift ($\phi_r(\omega)$)

$$\phi_r(\omega) = -\frac{2\omega}{\pi}\mathbf{P}\int_{0}^{\infty}\frac{ln|\hat{r}(\omega')|}{\omega'^2 - \omega^2}d\omega' = -\frac{\omega}{\pi}\mathbf{P}\int_{0}^{\infty}\frac{lnR(\omega')}{\omega'^2 - \omega^2}d\omega' \tag{3.58}$$

This equation indicates that, to obtain the phase shift, one need to measure

Low frequency	Hagen-Rubens	$1 - R(\omega) \propto \omega^{1/2}$
	Marginal Fermi Liquid	$1 - R(\omega) \propto \omega$
	Two Fluid	$1 - R(\omega) \propto \omega^2$
	Superconductor	$1 - R(\omega) \propto \omega^4$
High frequency	interband transition	$R(\omega) \propto \omega^{1/2}$
	Free electron	$R(\omega) \propto \omega^4$

Table 3.1: Low and High frequency limit extrapolations for Kramers-Kronig analysis.

the normal incident reflectivity to zero on the low frequency side and to infinite on the high frequency side. This is experimentally impossible. In order to use the Kramers-Kronig analysis, we measure the reflectivity over a broad frequency range, from very far-infrared (20 cm^{-1}) to visible, even ultraviolet range (55000 cm^{-1}). Then, we choose proper extrapolations for the low and high frequency limits. Choosing a proper extrapolation is very important in Kramers-Kronig analysis. For example, a good metal exhibits high reflectivity which approaches unity at low frequencies. The Hagen-Rubens frequency response $[1-R(\omega) \propto \sqrt{\omega}]$ can describe the metallic behavior at low frequencies quite well. Figure 3.3 shows the Hagen-Rubens frequency response and the low frequency reflectivity of gold. Note that the Hagen-Rubens frequency response matches the reflectivity of gold perfectly well at low frequencies and can be used as the low frequency limit extrapolation for a good metal. For an insulator, we usually use a constant for the low frequency limit extrapolation. For a superconductor, we can use the two fluid model or superconductor frequency response for the low frequency limit extrapolation. Some useful low frequency limit extrapolations are listed in Table 3.1. On the high frequency side, we use either a constant or an interband transition frequency response followed by a free electron behavior as the high frequency limit extrapolation, since at sufficiently high frequencies, all the electrons can be considered free. The high frequency limit extrapolations are also listed in Table 3.1. By combining the measured data over a broad frequency range and proper low and high frequency limit extrapolations, we can use the Kramers-Kronig

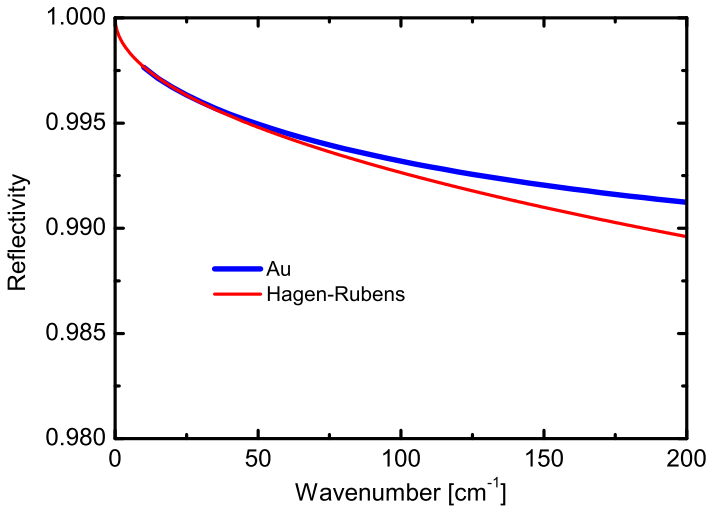

Figure 3.3: The Hagen-Rubens frequency response and the low frequency reflectivity of gold.

analysis to calculate the phase shift and further other optical constants using the formulas listed in Table 3.2.

3.4.2 Sum rules

By combining the Kramers-Kronig relations with physical arguments about the behavior of the real and imaginary parts of the response function, we can establish a set of sum rules for various optical parameters. For instance, the real

Index of refraction	$n(\omega) = \frac{1-R(\omega)}{1+R(\omega)-2\sqrt{R(\omega)}\cos\phi(\omega)}$
Extinction coefficient	$k(\omega) = \frac{2\sqrt{R(\omega)}\sin\phi(\omega)}{1+R(\omega)-2\sqrt{R(\omega)}\cos\phi(\omega)}$
Real part of the dielectric constant	$\epsilon_1(\omega) = n^2(\omega) - k^2(\omega)$
Imaginary part of the dielectric constant	$\epsilon_2(\omega) = 2n(\omega)k(\omega)$
Real part of the optical conductivity	$\sigma_1(\omega) = \frac{2\pi}{Z_0}\omega\epsilon_2(\omega)$
Imaginary part of the optical conductivity	$\sigma_2(\omega) = \frac{2\pi}{Z_0}\omega[1 - \epsilon_1(\omega)]$

Table 3.2: Formulas for calculating the optical constants.

part of the dielectric function can be written as

$$\begin{aligned}\epsilon_1(\omega) - 1 &= \frac{2}{\pi}\mathbf{P}\int_0^\infty \frac{\omega'\epsilon_2(\omega')}{\omega'^2 - \omega^2}d\omega' \\ &= \frac{2}{\pi}\mathbf{P}\int_0^{\omega_c} \frac{\omega'\epsilon_2(\omega')}{\omega'^2 - \omega^2}d\omega' + \frac{2}{\pi}\mathbf{P}\int_{\omega_c}^\infty \frac{\omega'\epsilon_2(\omega')}{\omega'^2 - \omega^2}d\omega'\end{aligned} \tag{3.59}$$

where ω_c is a cutoff frequency above which there is no absorption, i.e. $\epsilon_2(\omega) = 0$ for $\omega > \omega_c$, hence the second integral is zero. For $\omega \gg \omega_c$, Eq. 3.59 becomes

$$\epsilon_1(\omega) - 1 = -\frac{2}{\pi\omega^2}\int_0^{\omega_c} \omega'\epsilon_2(\omega')d\omega' \tag{3.60}$$

At sufficiently high frequencies, all the electrons can be considered free and the real dielectric function is given by the following equation which will be shown in the Drude model (Sec. 3.5)

$$\epsilon_1(\omega) = 1 - \frac{\Omega_p^2}{\omega^2} \tag{3.61}$$

where Ω_p is the plasma frequency defined as

$$\Omega_p^2 = \frac{Z_0 n e^2}{2\pi m} \tag{3.62}$$

Comparison of Eq. 3.60 and Eq. 3.61 yields

$$\int_0^\infty \omega\epsilon_2(\omega)d\omega = \frac{\pi}{2}\Omega_p^2 \tag{3.63}$$

where the upper limit of the integral has been extended to ∞ because $\epsilon_2(\omega) = 0$ for $\omega > \omega_c$. From the relation between $\epsilon_2(\omega)$ and $\sigma_1(\omega)$, we can get

$$\int_0^\infty \sigma_1(\omega)d\omega = \frac{\pi^2}{Z_0}\Omega_p^2 = \frac{\pi n e^2}{2m} \tag{3.64}$$

Since n refers to the total number of electrons and m to the bare electron mass, the above equation indicates that the total spectral weight integral of $\sigma_1(\omega)$ is finite and conserved, and proportional to n/m.

The optical conductivity is a linear response function, the total optical conductivity is a simple sum of the conductivity for different excitations. If these excitations are decoupled, the sum rule is fulfilled separately for each kind of excitation. In this case, for conduction electrons limited to one band, one can define a partial sum rule by replacing the upper limit in the integration of Eq. 3.64 with a cut-off frequency representative of the band width. Now, n and m refer to the conduction electron density and their effective mass.

3.5 The Drude model and the Lorentz model

3.5.1 Drude model

Drude model is used to describe the response of free charge carriers. In Drude's theory, we assume that (i) when atoms of a metallic element are brought together to form a metal, the valence electrons become detached and wander freely through the metal, while the metallic ions remain intact and play the role of the immobile positive particles. This is known as the *free electron approximation*; (ii) between collisions we neglect the interaction of a given electron both with others and with ions, which is known as the *independent electron approximation*; (iii) an electron experiences a collision with a probability per unit time $1/\tau$. So an average relaxation time τ exists and governs the relaxation of the system to equilibrium. In the absence of an external field $\mathbf{E}$, the rate equation is

$$\frac{d\langle \mathbf{p} \rangle}{dt} = -\frac{\langle \mathbf{p} \rangle}{\tau} \tag{3.65}$$

Upon the application of an external electric field $\mathbf{E}$, the equation of motion becomes

$$\frac{d}{dt}\langle \mathbf{p} \rangle = -\frac{\langle \mathbf{p} \rangle}{\tau} - e\mathbf{E} \tag{3.66}$$

For a DC field, $d\langle \mathbf{p} \rangle/dt = 0$ resulting in a DC conductivity

$$\sigma_{dc} = \frac{ne^2\tau}{m} \tag{3.67}$$

Considering that the time-dependent electric field has a form

$$\mathbf{E}(t) = \mathbf{E}_0 \exp(-i\omega t) \tag{3.68}$$

the solution of the equation of motion

$$m\frac{d^2\mathbf{r}}{dt^2} + \frac{m}{\tau}\frac{d\mathbf{r}}{dt} = -e\mathbf{E}(t) \tag{3.69}$$

gives a complex, frequency dependent conductivity

$$\hat{\sigma}(\omega) = \sigma_1(\omega) + i\sigma_2(\omega) = \frac{ne^2\tau}{m}\frac{1}{1 - i\omega\tau} \tag{3.70}$$

which can be decomposed into the real $[\sigma_1(\omega)]$ and imaginary $[\sigma_2(\omega)]$ parts

$$\sigma_1(\omega) = \frac{ne^2\tau}{m}\frac{1}{1+\omega^2\tau^2} = \frac{2\pi\Omega_p^2\tau}{Z_0}\frac{1}{1+\omega^2\tau^2} = \frac{\sigma_{dc}}{1+\omega^2\tau^2} \tag{3.71}$$

$$\sigma_2(\omega) = \frac{ne^2\tau}{m}\frac{\omega\tau}{1+\omega^2\tau^2} = \frac{2\pi\Omega_p^2\tau}{Z_0}\frac{\omega\tau}{1+\omega^2\tau^2} \tag{3.72}$$

At zero frequency $\omega = 0$, Eq. 3.71 becomes

$$\sigma_1(\omega = 0) = \frac{ne^2\tau}{m} = \sigma_{dc} \tag{3.73}$$

representing the DC conductivity. Assuming $\sigma_1(\omega) = \sigma_{dc}/2$, we obtain $\omega = 1/\tau$, indicating that the width of the Drude line shape at half height gives the scattering rate $(1/\tau)$ of the free carriers.

Moreover, the sum rules can be easily achieved from the Drude model by direct integration

$$\int_0^\infty \sigma_1(\omega)d\omega = \frac{ne^2}{m}\int_0^\infty \frac{\tau d\omega}{1+\omega^2\tau^2} = \frac{\pi ne^2}{2m} = \frac{\pi^2}{Z_0}\Omega_p^2 \tag{3.74}$$

Within the framework of the Drude model, all the optical constants can be derived from the complex optical conductivity utilizing the general relations listed in Table 3.2. For example, the frequency dependence of the complex dielectric constant is

$$\hat{\epsilon}(\omega) = \epsilon_1(\omega) + i\epsilon_2(\omega) = 1 + \frac{iZ_0\hat{\sigma}(\omega)}{2\pi\omega} = 1 - \frac{\Omega_p^2}{\omega^2 - i\omega/\tau} \tag{3.75}$$

with the real and imaginary parts

$$\epsilon_1(\omega) = 1 - \frac{\Omega_p^2}{\omega^2 + \tau^{-2}} \tag{3.76}$$

$$\epsilon_2(\omega) = \frac{1}{\omega\tau}\frac{\Omega_p^2}{\omega^2 + \tau^{-2}} \tag{3.77}$$

Here, we can see that at sufficiently high frequencies $\omega \gg 1/\tau$, the real part of the dielectric constant can be written as

$$\epsilon_1(\omega) = 1 - \frac{\Omega_p^2}{\omega^2} \tag{3.78}$$

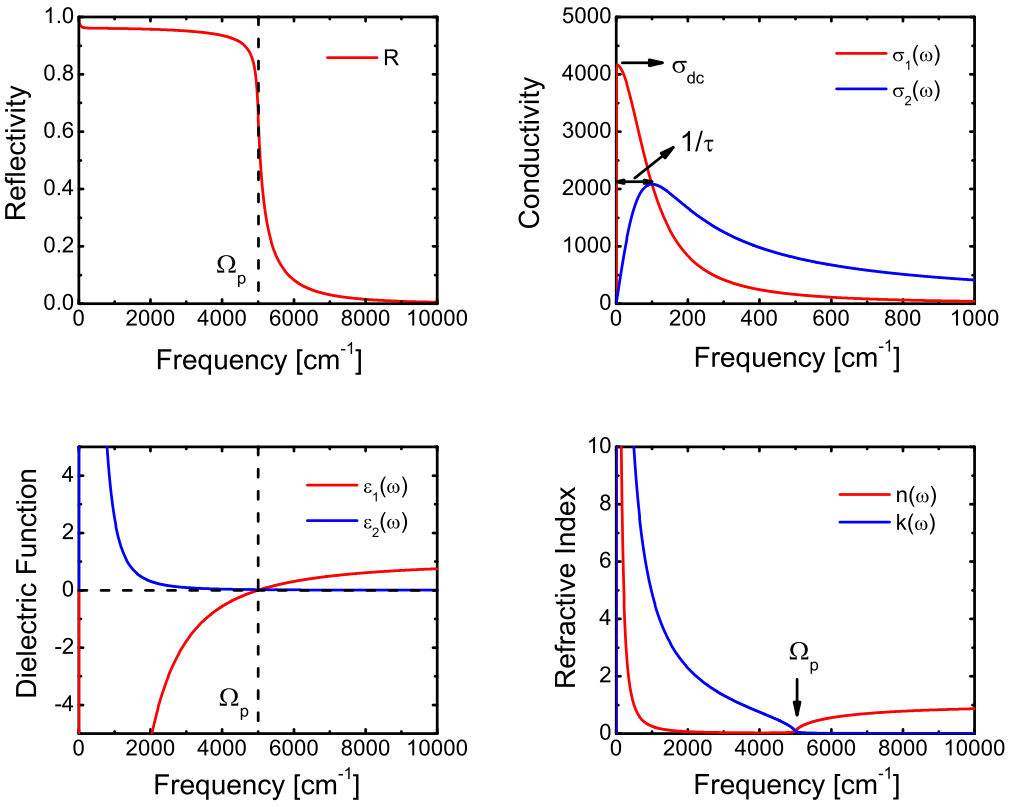

Figure 3.4: Calculated frequency dependent optical constants within the framework of Drude model. $\Omega_p = 5000$ cm^{-1}, $1/\tau = 100$ cm^{-1}.

This equation was used to derive the sum rules in previous section.

In the Drude model, all the various optical parameters are fully characterized by two frequencies: the plasma frequency Ω_p and the scattering rate $1/\tau$. A calculation of the frequency dependent optical constants within the framework of the Drude model is shown in Fig. 3.4. $\Omega_p = 5000$cm^{-1} and $1/\tau = 100$ cm^{-1} are used for the calculations. At the plasma frequency Ω_p, the reflectivity drops drastically from near unity to almost zero and the material becomes transparent. The real part $[\sigma_1(\omega)]$ of the optical conductivity shows a peak centered at zero frequency with $\sigma_1(0) = \sigma_{dc}$, and the width at half height represents $1/\tau$; the imaginary part $[\sigma_2(\omega)]$ peaks at $1/\tau$ where $\sigma_1 = \sigma_2 = \sigma_{dc}/2$. The real part of the dielectric constant $\epsilon_1(\omega)$ crosses zero at Ω_p and becomes negative at low frequencies; the imaginary part $\epsilon_2(\omega)$ stays always positive, and decreases monotonically

with increasing frequency, but changes slope at the plasma frequency. Below Ω_p, we have $k > n$, and they cross over at the plasma frequency. Above the plasma frequency, the metal becomes transparent, thus k drops to about zero; the real part of the refractive index n increases and approaches to 1 when $\omega \to \infty$.

The Drude model achieved a great success in describing the low frequency optical response of simple metals, e.g. gold and silver, which have a very high reflectivity followed by a sharp plasma edge. Even for a superconductor in the normal state, the Drude model can give a good description of the optical response of the unpaired carriers. Figure 3.5 shows the reflectivity of gold. It has a well

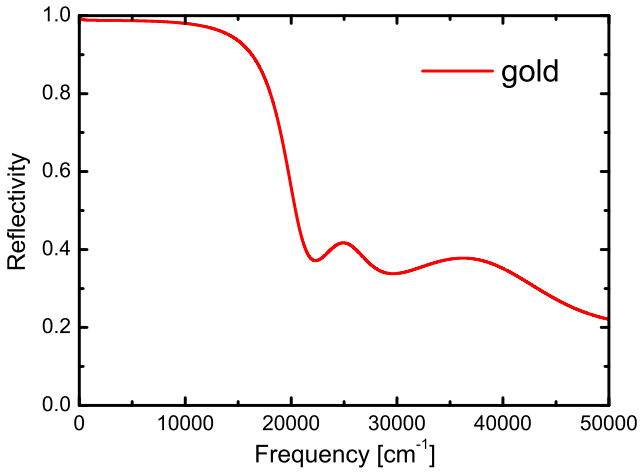

Figure 3.5: Reflectivity of gold which is characterized by the high reflectivity followed by a sharp plasma edge at about 19000 cm^{-1}.

defined plasma edge at about 19000 cm^{-1}, and the two peaks at about 25000 cm^{-1} and 37000 cm^{-1} are due to the interband transitions.

3.5.2 Lorentz model

In the previous section, we discussed the Drude model to describe the response of free electrons. In this section, we introduce another important model the Lorentz model used to account for the behavior of bound carriers like the situation in an insulator.

We consider the interaction between the electromagnetic wave and a bound carrier with effective charge e and a single resonant frequency ω_0, in much the same way as a carrier is bound by a spring (like a harmonic oscillator). The motion of the bound carrier can be described by

$$m\frac{d^2\mathbf{r}}{dt^2} + \frac{m}{\tau}\frac{d\mathbf{r}}{dt} + m\omega_0^2\mathbf{r} = e\mathbf{E} \tag{3.79}$$

Where m is the mass of the carrier; e is the effective charge of the carrier; τ takes into account damping effects, and $\mathbf{E}$ is the local electric field acting on the electron as a driving force. When the local electric field $\mathbf{E}$ has an $\exp(i\omega t)$ time dependence, the solution to Eq. 3.79 is

$$\hat{\mathbf{r}}(\omega) = \frac{e\mathbf{E}/m}{(\omega_0^2 - \omega^2) - i\omega/\tau} \tag{3.80}$$

and for the induced dipole moment $\hat{\mathbf{p}}(\omega) = e\hat{\mathbf{r}}(\omega)$ we obtain

$$\hat{\mathbf{p}}(\omega) = \frac{e^2\mathbf{E}}{m}\frac{1}{(\omega_0^2 - \omega^2) - i\omega/\tau} \tag{3.81}$$

The polarization of the system can be written as

$$\mathbf{P} = n\langle\hat{\mathbf{p}}\rangle = \epsilon_0\hat{\chi_e}\mathbf{E} \tag{3.82}$$

where $\hat{\chi_e}$ is the dielectric susceptibility. Since the dielectric constant is related to the dielectric susceptibility via $\hat{\epsilon}(\omega) = 1 + \hat{\chi_e}(\omega)$, the frequency dependent complex dielectric constant follows:

$$\hat{\epsilon}(\omega) = 1 + \frac{ne^2}{\epsilon_0 m}\frac{1}{(\omega_0^2 - \omega^2) - i\omega/\tau} = 1 + \frac{\Omega_p^2}{(\omega_0^2 - \omega^2) - i\omega/\tau} \tag{3.83}$$

with the real and imaginary parts

$$\epsilon_1(\omega) = 1 + \frac{\Omega_p^2(\omega_0^2 - \omega^2)}{(\omega_0^2 - \omega^2)^2 + \omega^2/\tau^2} \tag{3.84}$$

$$\epsilon_2(\omega) = \frac{\Omega_p^2\omega/\tau}{(\omega_0^2 - \omega^2)^2 + \omega^2/\tau^2} \tag{3.85}$$

where Ω_p is the plasma frequency defined as

$$\Omega_p^2 = \frac{ne^2}{\epsilon_0 m} \tag{3.86}$$

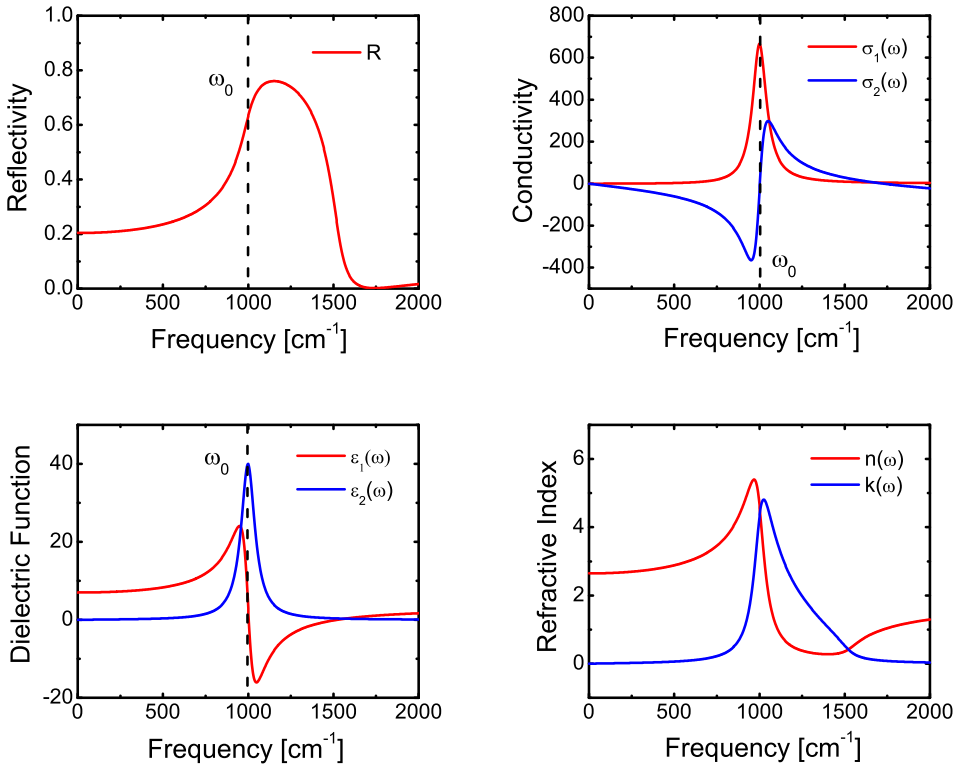

Figure 3.6: Calculated frequency dependent optical constants within the framework of Lorentz model using $\omega_0 = 1000$ cm^{-1}, $\Omega_p = 2000$ cm^{-1}, and $1/\tau = 100$ cm^{-1}.

As we did for the Drude model in the previous section, we can derive all other complex optical constants from the frequency dependent complex dielectric constant using the relations in Table 3.2. Figure 3.6 shows the calculations of the frequency dependent optical parameters within the framework of the Lorentz model.

The Lorentz model shows remarkably different properties from the Drude model. The Lorentz response is characterized by three frequencies: a resonance frequency ω_0, a plasma frequency Ω_p, and a scattering rate $1/\tau$. The reflectivity shows a strong increase at the resonance frequency (ω_0) of the oscillator as displayed in the Reflectivity panel of Fig. 3.6. The real part of the optical con-

ductivity peaks at ω_0 with a width representing the scattering rate $1/\tau$ while the imaginary part crosses zero at about the resonance frequency. $\epsilon_1(\omega)$ and $\epsilon_2(\omega)$ exhibit a similar behavior to $\sigma_2(\omega)$ and $\sigma_1(\omega)$ respectively.

The Lorentz model describes well the optical response of an insulator which is dominated by phonons at low frequencies. As shown in Fig. 3.7, the dashed

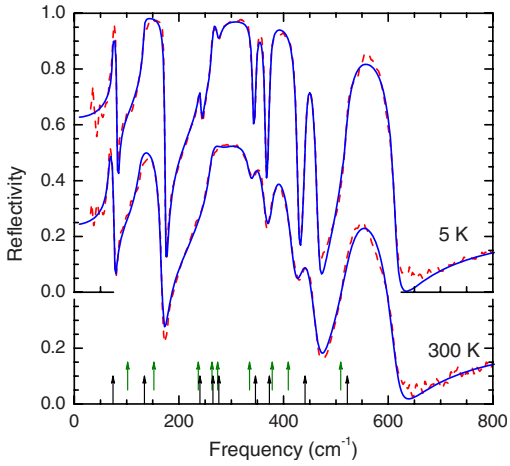

Figure 3.7: In-plane infrared reflectivity of a $BiFeO_3$ single crystal at 5 K and 300 K, adopted from Ref. [59]. The dashed lines represent the experimental data and the solid lines are fits utilizing Lorentz model.

lines are the in-plane infrared reflectivity of a $BiFeO_3$ single crystal (an insulator) at 5 and 300 K measured on a Fourier Transform Infrared Spectrometer [59]. The solid lines are fits using the Lorentz model dielectric function. We can see that the Lorentz model reproduces the experimental data quit well. This model can also be used to describe the optical response of the interband transitions which happens at relatively high frequencies in both metals and semiconductors.

3.6 Optical response of energy gaps

We have mentioned that, in a many-body system, the electron-electron and electron-phonon interactions play an important role. These interactions may result in a variety of low-energy ordered states, so-called broken symmetry ground

states, of which the density waves (spin density wave and charge density wave) and the superconducting ground states are the best known and most studied. All these states occur at low temperature in anisotropic, low-dimensional materials or in metals that have high density of states at the Fermi level. The transition to the ordered states is characterized by the opening of an energy gap centered about the Fermi level, which separates the single-particle excitations from the ground state by 2Δ. However, the optical properties of the density waves and the superconducting order states are remarkably different.

3.6.1 Density wave gaps

A density wave phase transition is accompanied by the opening of an energy gap near the Fermi surface which produces a depletion of low energy states. Since the real part of the optical conductivity $\sigma_1(\omega)$ is proportional to the joint density of states, a depletion of low lying states certainly suppresses the low frequency $\sigma_1(\omega)$ spectra. Figure 3.8 shows $\sigma_1(\omega)$ of $P_4W_{14}O_{50}$, which has a

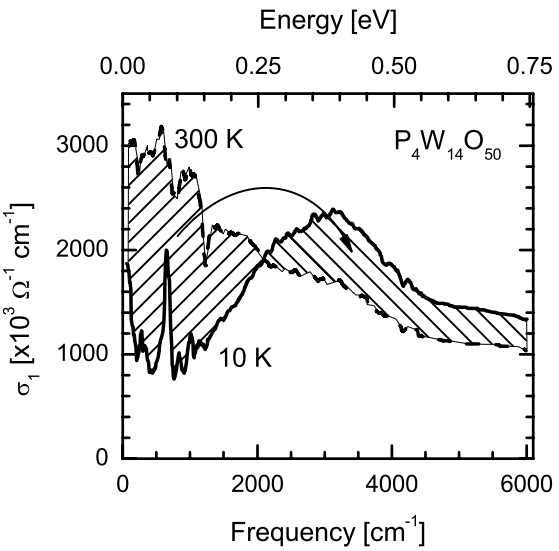

Figure 3.8: The real part of the optical conductivity for $P_4W_{14}O_{50}$ at 300 K and 10 K, adapted from Ref. [60]. The arrow shows the spectral weight transfer from low to high energies due to the opening of the CDW gap.

charge density wave (CDW) transition at 60 K [60]. At 300 K, the spectra shows a metallic response characterized by a Drude peak centered at zero frequency. At 10 K, when the CDW gap is fully open, $\sigma_1(\omega)$ below 2000 cm^{-1} is drastically suppressed. Simultaneously, $\sigma_1(\omega)$ increases at higher frequencies. The sum rule requires that the integral of $\sigma_1(\omega)$ from zero to infinity, the total area under $\sigma_1(\omega)$, should be conserved. This implies that the spectral weight lost below the gap value is exactly equal to the spectral weight gained above the gap value. The same optical response can be observed for an spin density wave (SDW) gap [61, 62]. Therefore, the typical behavior of a density wave gap is the transfer of low energy spectral weight to high energies.

3.6.2 Superconducting gaps

The electrodynamics of the superconducting state is different from the density waves. Figure 3.9 shows the optical conductivity of the conventional superconductor NbN with a transition temperature of 16.5 K [63]. Above T_c (at 18 K), the Drude-like metallic response dominates the low frequency optical conductivity. In the superconducting state (at 9 K), the strong suppression in optical conductivity at low frequencies is due to the opening of the superconducting gap, but contrary to a density wave gap, no spectral weight is transferred to high frequencies. Yet, the sum rule must be fulfilled. Note that the DC resistivity in superconducting state is zero, i.e. it has infinite DC conductivity which is represented by a $\delta(\omega)$ function at zero frequency. The spectral weight lost from finite frequencies due to the superconducting transition is fully recovered by this $\delta(\omega)$ function. This is referred to as the Ferrell-Glover-Tinkham (FGT) sum rule [15, 64]. In contrast with the density wave gap, the typical behavior of a superconducting gap is the transfer of spectral weight from finite frequencies to a $\delta(\omega)$ function at zero frequency representing the infinite DC conductivity.

The optical properties of the superconducting state can be described by the Mattis-Bardeen formalism which is derived from the BCS theory in the impure limit ($\tau \ll \hbar/2\Delta$) [65]. Within the Mattis-Bardeen formalism, the complex conductivity in the superconducting state $\hat{\sigma}(\omega, T)$ normalized to the conductivity

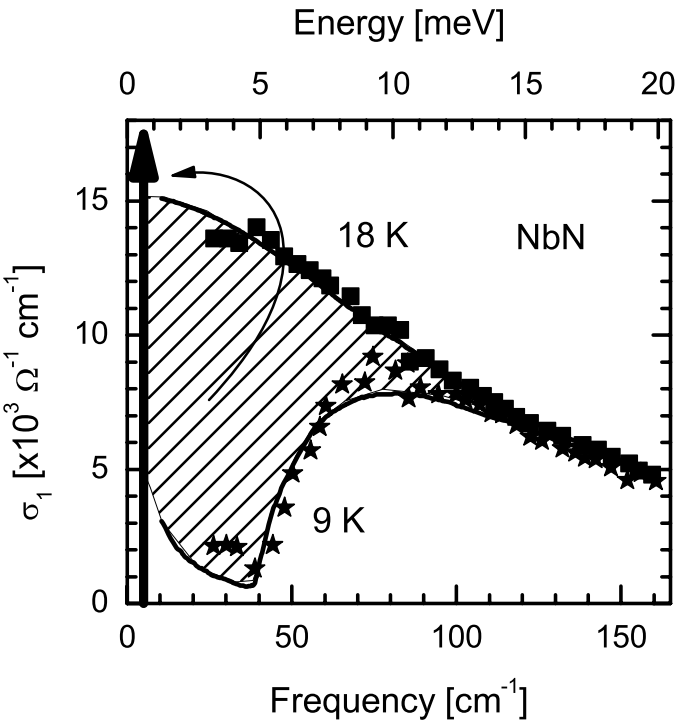

Figure 3.9: The real part of optical conductivity of NbN (T_c = 16.5 K) above and below the superconducting transition temperature, adapted from Ref. [63]. The large vertical arrow is the zero frequency $\delta(\omega)$ function representing the superfluid condensate.

in the normal state $\hat{\sigma}(\omega, T > T_c)$ can be written as

$$\frac{\sigma_1(\omega,T)}{\sigma_1(\omega,T>T_c)} = \frac{2}{\hbar\omega}\int_{\Delta}^{\infty}\frac{[f(\varepsilon)-f(\varepsilon+\hbar\omega)](\varepsilon^2+\Delta^2+\hbar\omega\varepsilon)}{(\varepsilon^2-\Delta^2)^{1/2}[(\varepsilon+\hbar\omega)^2-\Delta^2]^{1/2}}d\varepsilon + \frac{1}{\hbar\omega}\int_{\Delta-\hbar\omega}^{-\Delta}\frac{[1-2f(\varepsilon+\hbar\omega)](\varepsilon^2+\Delta^2+\hbar\omega\varepsilon)}{(\varepsilon^2-\Delta^2)^{1/2}[(\varepsilon+\hbar\omega)^2-\Delta^2]^{1/2}}d\varepsilon \tag{3.87}$$

$$\frac{\sigma_2(\omega,T)}{\sigma_2(\omega,T>T_c)} = \frac{1}{\hbar\omega}\int_{\Delta-\hbar\omega,-\Delta}^{\Delta}\frac{[1-2f(\varepsilon+\hbar\omega)](\varepsilon^2+\Delta^2+\hbar\omega\varepsilon)}{(\varepsilon^2-\Delta^2)^{1/2}[(\varepsilon+\hbar\omega)^2-\Delta^2]^{1/2}}d\varepsilon \tag{3.88}$$

Zimmermann et.al extended the Mattis-Bardeen formulism to superconductors with arbitrary purity [66]. Figure 3.10 shows the calculation for frequency dependence of the real part of the optical conductivity and the reflectivity in the

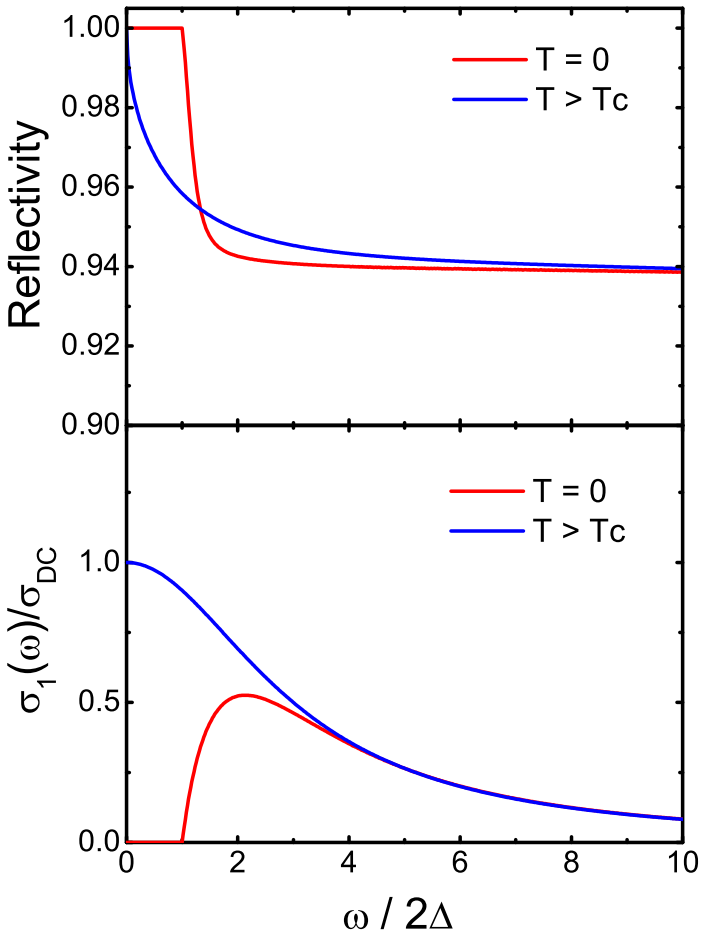

Figure 3.10: Calculated frequency dependence of the reflectivity and the real part of the optical conductivity in the normal and superconducting states.

normal and superconducting states. The normal state spectra are calculated from a Drude model with $\Omega_p = 5000$ cm^{-1} and $1/\tau = 300$ cm^{-1}, and the superconducting state curves are calculated from the Mattis-Bardeen formalism with the same plasma frequency and scattering rate as the Drude model in the normal state. At zero temperature, the reflectivity reaches a flat unity response for frequencies below the gap energy indicating that superconductors are perfect mirrors for $\omega < 2\Delta$. Correspondingly, the optical conductivity $\sigma_1(\omega)$ is zero below the superconducting gap 2Δ except for the δ-peak at zero frequency representing the infinite DC conductivity.

This is only the situation of a conventional superconductor with an isotropic s-wave gap in the dirty limit [67, 68]. The gap feature is absent when the superconductor is in the clean limit [69]. By comparing the mean free path of the quasiparticles with the coherence length of the Cooper pairs, we can define a clean or dirty superconductor. In a clean superconductor $l \gg \xi$ and the opposite occurs in a dirty superconductor. The mean free path is given by $l \approx v_F\tau$, whereas the coherence length $\xi \approx v_F/\Delta$. Consequently, from the optics point of view, the definition of clean and dirty superconductor becomes $\tau^{-1} \ll 2\Delta$ and $\tau^{-1} \gg 2\Delta$ respectively. Figure 3.11 shows the BCS calculations in both the

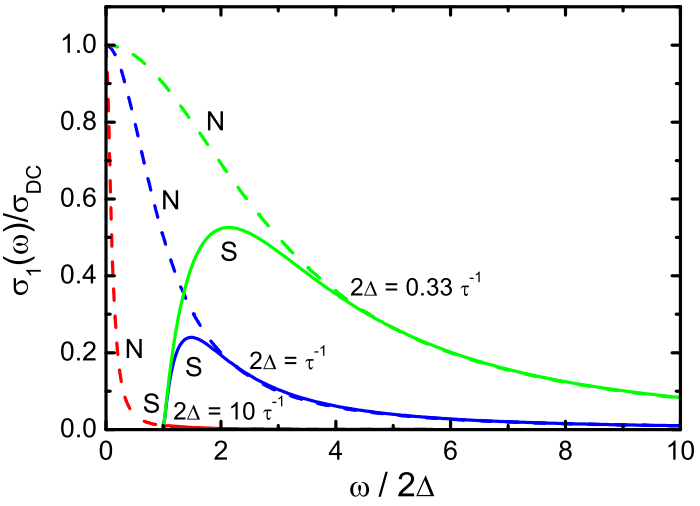

Figure 3.11: The BCS calculations of the real part of the optical conductivity in both clean and dirty limits with parameters: $2\Delta = 0.33\tau^{-1}$ (green lines), $2\Delta = \tau^{-1}$ (blue lines), and $2\Delta = 10\tau^{-1}$ (red lines). The labels 'N' and 'S' refer to the normal and superconducting states, respectively.

clean and dirty limits. The green lines are calculated optical conductivity for a dirty superconductor in normal (dashed line) and superconducting (solid line) states. In the normal state, since τ^{-1} is large compared to 2Δ, the Drude peak is very broad and the optical conductivity at 2Δ is almost as large as σ_{DC}; at the superconducting transition, the optical conductivity vanishes below 2Δ and exhibits a distinct gap feature at 2Δ as shown by the green lines. In the case of

the clean limit, the Drude peak is much narrower than the gap value; the normal state conductivity at 2Δ is vanishingly small. Upon entering the superconducting state, almost no gap feature appears at twice the gap value as shown by the red lines in Fig. 3.11.

Superconductors with d-wave paring symmetry, cuprates for instance, show strikingly different optical properties from the conventional superconductors. As nodes exist in the d-wave superconducting gap, a large number of unpaired quasipaticles appear close to the nodal region. Hence a low frequency residual conductivity should be observed in the superconducting state. Figure 3.12 shows

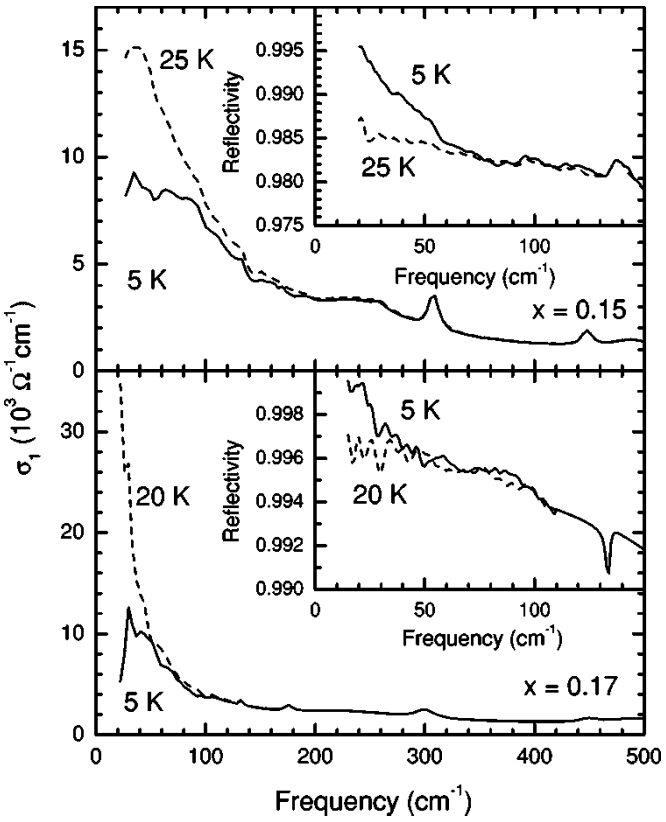

Figure 3.12: Reflectivity and the real part of the optical conductivity for optimally (top panel) and over (bottom panel) doped $Pr_{2-x}Ce_xCuO_4$, adapted from Ref. [70].

the reflectivity and the optical conductivity of $Pr_{2-x}Ce_xCuO_4$ thin film for two

different dopings x = 0.15 with T_c = 21 K (top panel) and x = 0.17 with T_c = 15 K (bottom panel) [70]. The inset of the top panel displays the reflectivity of the x = 0.15 sample (T_c = 21 K) at 25 K and 5 K. Compared with the normal state reflectivity at 25 K, the reflectivity at 5 K increases below about 60 cm^{-1} which is a signature of a superconducting gap. However, unlike *s*-wave superconductors, it doesn't reach a flat unity response. The top main panel shows the optical conductivity of the x = 0.15 sample. The dashed and solid lines denote the normal (25 K) and superconducting (5 K) state spectra respectively. The low frequency optical conductivity is suppressed at 5 K which is associated with the superconducting condensate, but it does not vanish at low frequencies. This residual conductivity is compatible with the existence of nodes in the superconducting gap. The reflectivity and optical conductivity spectra for the x = 0.17 sample shown in the bottom panel exhibit the same features as the x = 0.15 sample. A similar result is reported on a single crystal [71].

In another class of materials, we find two band superconductor MgB_2. In superconducting state, *s*-wave gaps with the same sign but different values, the so-called s_{++} symmetry, open in each band. Hence, the optical properties of MgB_2 has some distinguishing features [72–74]. Figure 3.13 displays the optical conductivity (normalized by the normal state) of MgB_2 with a transition temperature of 38 K. The spectra were measured at 20 K in different magnetic field. Let's focus on the zero magnetic field optical conductivity at 20 K shown as the solid line. $\sigma_1(\omega)$ is almost zero below about 30 cm^{-1} implying that the superconducting gap has an *s*-wave symmetry. The energy, below which the conductivity vanishes, corresponds to twice the small gap value $2\Delta_S$, where Δ_S represents the value of the small gap. Here it's easy to see $2\Delta_S \approx 30$ cm^{-1}. At frequencies higher than $2\Delta_S \approx 30$ cm^{-1}, absorption sets in, indicating pair-breaking in the small gap. The large gap manifests itself as a kink in the optical conductivity at twice its value. Note that the small kink at 50 cm^{-1} is related to the large gap.

In summary, the optical conductivity is very sensitive to the low frequency collective excitations. Different superconducting gap symmetries exhibit strikingly different optical properties. The $s_{\pm}$ pairing symmetry proposed for the iron-based superconductors represents a brand new situation. Although con-

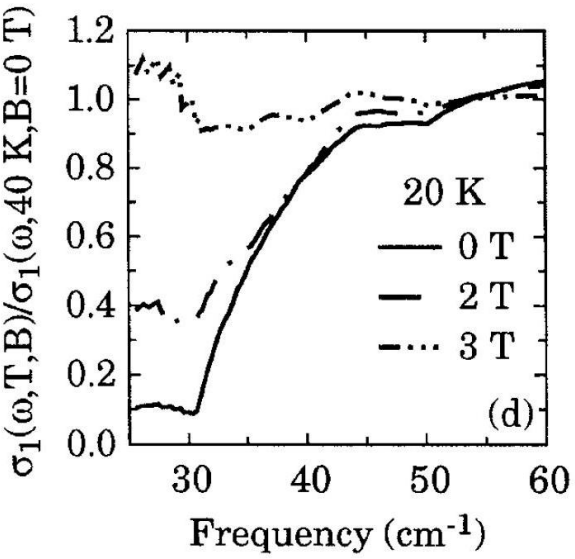

Figure 3.13: Real part of the optical conductivity for MgB_2 single crystal with $T_c = 38$ K, adapted from Ref. [74]. The optical conductivity vanishes below the energy of twice the small gap ~ 30 cm^{-1}, and a kink can be seen at twice the large gap ~ 50 cm^{-1}.

siderable results from optical measurements exist in iron-based superconductors [75–92]. Detailed and systematic work is still absent. The optical response of the $s_{\pm}$ superconducting gap remains highly debated.

Chapter 4

Iron-based High-T_c superconductors

4.1 Introduction to Iron-based superconductors

In 2006, the first iron-based superconductor, LaFePO, was reported by Hosono's group [5]. The next year, a similar material, LaNiPO, was reported by the same group [6]. But due to the low transition temperature (below 5 K) of these materials, these results didn't create extensive interest in the scientific community. The breakthrough came with the fluoride doped arsenide $LaFeAsO_{1-x}F_x$ with the transition temperature up to 26 K [8] which increases to 43 K under pressure [93]. Shortly, a higher T_c up to 55 K was achieved by replacing lanthanum with samarium [94]. These compounds having a ZrCuSiAs-type layered structure are categorized as the 1111 system. Within the year the iron-based superconductor extended to six systems, $Ba_{1-x}K_xFe_2As_2$ [95] and $Ba(Fe_{1-x}Co_x)_2As_2$ [96] derived from $BaFe_2As_2$ representing the 122 system; LiFeAs [97] and NaFeAs [98] representing the 111 system; FeSe [9] and $Fe(Se_{1-x}Te_x)_{0.82}$ [10] representative of the 11 system; materials with more complex layered structure like $(Sr_3Sc_2O_5)Fe_2As_2$ [99] and $(Sr_4V_2O_6)Fe_2As_2$ [100] are representative of the 32522 and 21311 systems respectively. All these compounds represent a new class of high temperature superconductors. As shown in Fig. 4.1, each of them has the distinct layered structure with active FeAs or FeSe layers, in which superconductivity occurs, separated by perovskite-like blocking layers. Among the six systems of iron-based superconductors, the Ba122 system is one of the most studied. Because the parent compound $BaFe_2As_2$ can be easily doped with holes or electrons; superconductivity arises with maximum $T_c = 39$ K for hole doped material and $T_c = 25$ K for electron doped material; in addition, very large single crystals can be synthesized.

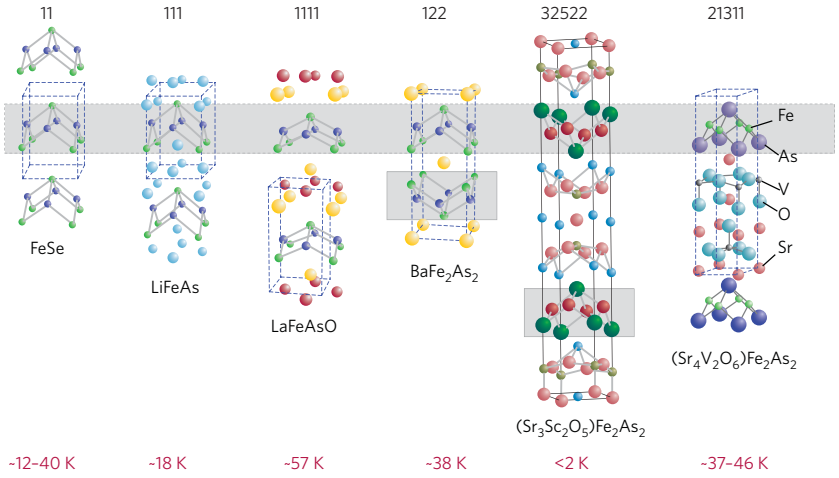

Figure 4.1: The six systems of iron-based superconductors discovered as yet. The temperature listed below each structure is the highest achieved T_c so far, adopted from Ref. [101].

4.2 Ba122 system

In this thesis, we will concentrate on the Ba122 compounds, in particular those doped with K or Co.

4.2.1 Crystal structure

The parent compound of Ba122 system is $BaFe_2As_2$ [102]. It has the tetragonal $ThCr_2Si_2$-type structure (space group $I4/mmm$), and contains distinct FeAs layers separated by barium atoms. Figure 4.2 shows the crystal structure of $BaFe_2As_2$. Experimental atomic positions in $BaFe_2As_2$ are: Ba (0, 0, 0), Fe (0.5, 0, 0.25), As (0, 0, z). The rest of the crystallographic data are listed in Table 4.1.

4.2.2 Band structure

Since the discovery of the iron-based superconductors, the detailed band structure had been calculated for all systems of these compounds [23, 103, 104].

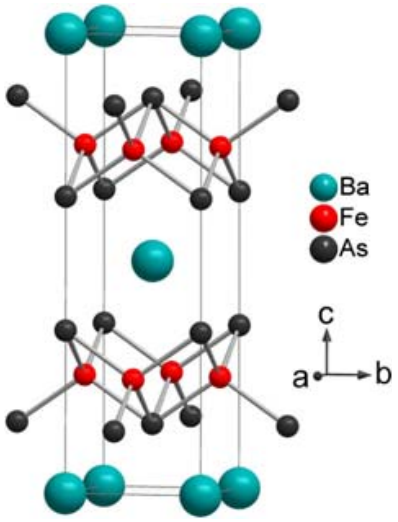

Figure 4.2: The crystal structure of $BaFe_2As_2$.

Figure 4.3 shows the local-density-approximation (LDA) calculations of band

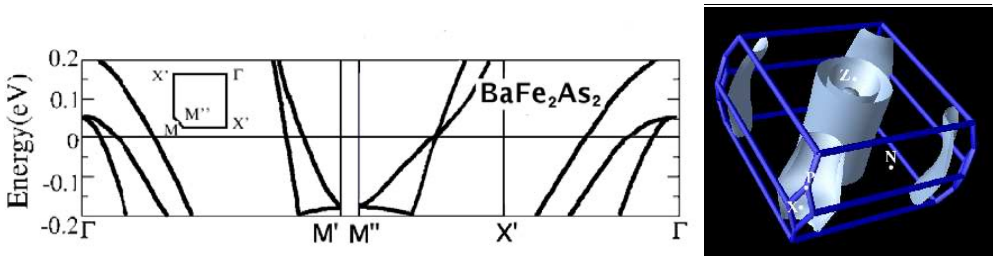

Figure 4.3: The left panel shows the calculated band structure of $BaFe_2As_2$ in a narrow interval of energies near the Fermi level. The right panel displays the Fermi surfaces of this material [105].

structure of $BaFe_2As_2$. Unlike the cuprates, where there is only one band crossing the Fermi level, in $BaFe_2As_2$, the Fermi level is crossed by five bands formed by d-states of Fe, three of them form hole-like Fermi surface pockets close to Γ-point, and the other two form electron-like pockets at the corners of Brillouin zone. This can be seen from the left panel in Fig. 4.3. Clearly, this kind of band structure results in similar Fermi surfaces in these materials. The calculated Fermi surfaces of $BaFe_2As_2$ are shown in the right panel of Fig. 4.3. There are

parameters	values
a, Å	3.9625
b, Å	=a
c, Å	13.0168
z_{As}	0.3545
Ba-As, Å	3.382 × 8
Fe-As, Å	2.403 × 4
Fe-Fe, Å	2.802 × 4
As-Fe-As, (deg)	111.1 × 2
	108.7 × 4

Table 4.1: Crystallographic data of $BaFe_2As_2$.

three hole-like cylinders at the center of Brillouin zone and two electron-like cylinders at the corners. The smallest hole-like cylinders is usually neglected when analyzing the electronic properties in superconducting state, because its contribution to electronic properties is rather small. Superconductors derived from $BaFe_2As_2$ show a myriad of unconventional properties. In these compounds, superconductivity arises in a multi-band system with several Fermi surfaces of different nature (hole or electron-like), which is drastically different from the one-band situation in cuprates.

4.2.3 Phase diagram

One important step towards understanding the mechanism of the superconductivity is elucidating the electronic phase diagram in the temperature *vs* doping plane and comparing it with the known superconductors, such as the cuprates. For the cuprate superconductors, the parent compounds are Mott insulators. Upon doping with holes, the long-range antiferromagnetic order is completely suppressed before superconductivity sets in. They do not coexist at any point of the temperature *vs* doping phase diagram. In electron doped materials, a small coexistence region may or may not exist, this being an unsettled issue. However, the iron-based superconductors produce a different phase diagram. Figure 4.4

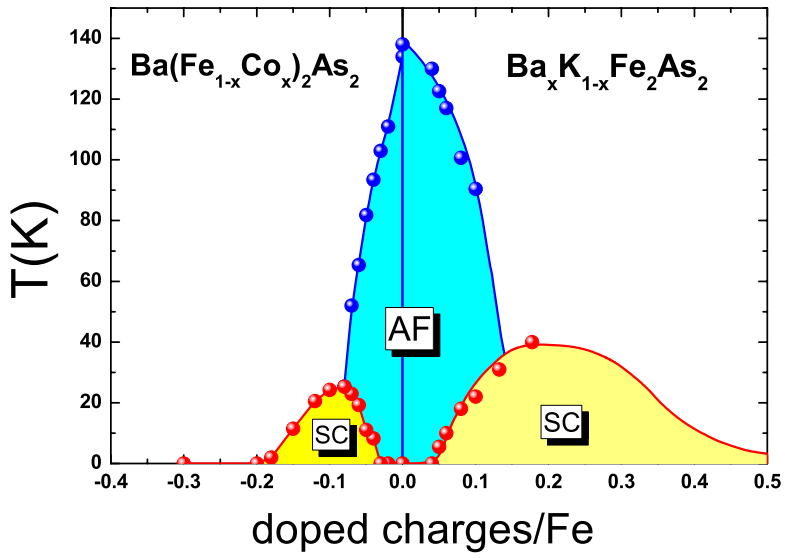

Figure 4.4: The phase diagram of Ba122 system adopted from Ref. [106].

shows the electronic phase diagram of the Ba122 system. Unlike the cuprates, the parent compound ($BaFe_2As_2$) of this system is a poor Pauli-paramagnetic metal with a structural and magnetic phase transition at 140 K [102]. Superconductivity emerges with the suppression of the magnetism which can be achieved by applying pressure or chemical substitution [95, 96, 107]. The substitution of Ba atoms with K atoms yields hole-doped materials [95] with a maximum $T_c \approx 38$ K while the Fe atoms can be substituted with Co or Ni atoms, resulting in electron doped materials [96, 107] with a maximum $T_c \approx 25$ K. As shown in Fig. 4.4, in both electron and hole doped regime, as the doping concentration increases, the magnetic ground state of the parent compound is suppressed, and superconducting domes arise inside the AFM region. An overlap between AFM and superconductivity exits in the underdoped region of the superconducting domes. Some reports claim that magnetically ordered phases and SC state are probably mesoscopically/microscopically separated [108–110] while others are in favor of the coexistence of the magnetic order and the superconductivity [111, 112].

4.2.4 Spin density wave

The parent compound ($BaFe_2As_2$) in this family undergoes a spin density wave (SDW) phase transition at about 140 K. Hu et al. investigated the optical response in the SDW state [61]. Figure 4.5 shows the optical conductivity

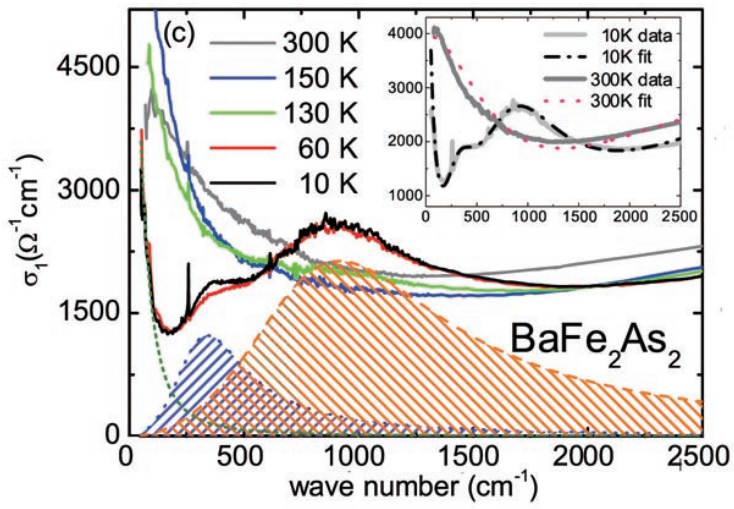

Figure 4.5: Optical conductivity of $BaFe_2As_2$ above and below the SDW transition temperature. Adopted from Ref. [61].

of $BaFe_2As_2$ (T_{SDW} = 138 K), in the normal state, the low frequency optical response is characterized by a Drude peak centered at zero frequency, indicating that the normal state of $BaFe_2As_2$ is metallic. Below T_{SDW} = 138 K, the spectra are substantially suppressed at low frequencies, and simultaneously, the high frequency spectra increase, forming a pronounced double-peak feature at 360 and 890 cm^{-1} on the optical conductivity. Clearly, this feature on $\sigma_1(\omega)$ signals the opening of the SDW gaps. The double-peak character is identified as two distinct SDW gaps which should be associated with different Fermi surface sheets and reflect the multiband property in the 122 system compounds.

4.2.5 Multiband metal

The presence of multiple Fermi surface sheets is also confirmed by a variety of techniques in Ba122 compounds.

The de Haas-van Alphen (dHvA) effect is used to measure the Fermi surface of bulk materials. Arnold et al. [113] reported the de Haas-van Alphen effect measurements in $BaFe_2P_2$ which has a similar band structure to $BaFe_2As_2$. A typical torque *vs* field oscillation curve for $BaFe_2P_2$ is shown in the top panel of Fig. 4.6. By taking the fast Fourier transform (FFT) spectra of the oscillatory

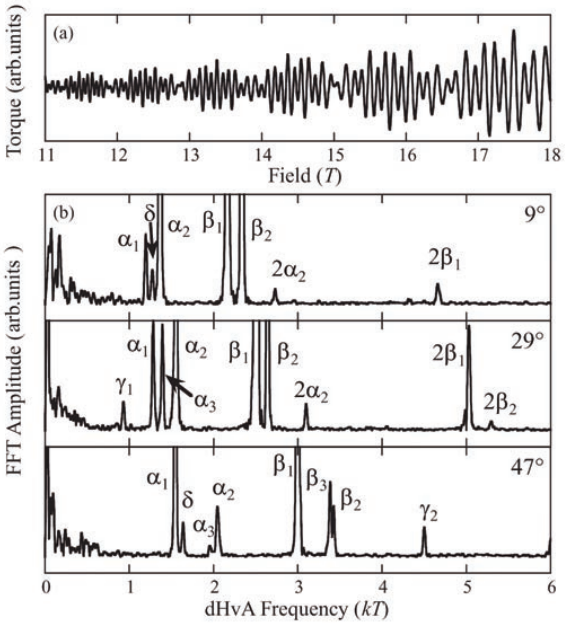

	γ_1	γ_2	δ	α_1	α_2	β_1	β_2
θ	28°	46°	12°	12°	12°	12°	12°
m^*/m_e	2.30	3.32	1.64	1.75	1.58	1.65	1.54
m^*/m_b	1.59	1.59	1.80	1.82	1.88	1.68	1.81
ℓ(nm)	40	150	40	190	200	170	160

Figure 4.6: The top panel shows a typical torque *vs* field oscillation curve for $BaFe_2P_2$ single crystal. The middle panel displays the fast Fourier transforms of the torque curves at various angles. The bottom panel lists some basic parameters on different Fermi surface sheets. Adopted from Ref. [113].

data, the dHvA frequencies can be obtained, as shown in the middle panel. Eight different dHvA peaks can be identified from the dHvA frequency spectra. These peaks originate from multiple Fermi surface sheets as expected by the band structure. The bottom panel lists some basic parameters on different Fermi surface

sheets. Note that the mean free paths l in different bands varies considerably. But two groups of values dominate all the Fermi surfaces. One group is about 40 nm while the other group has the values from 150 nm to 200 nm. Similar results are also observed in $BaFe_2(As_{1-x}P_x)_2$ [114] and $SrFe_2P_2$ [115].

Wu et al. studied the optical conductivity of various iron-based superconductors [85]. Figure 4.7 displays the measured optical conductivity (black solid

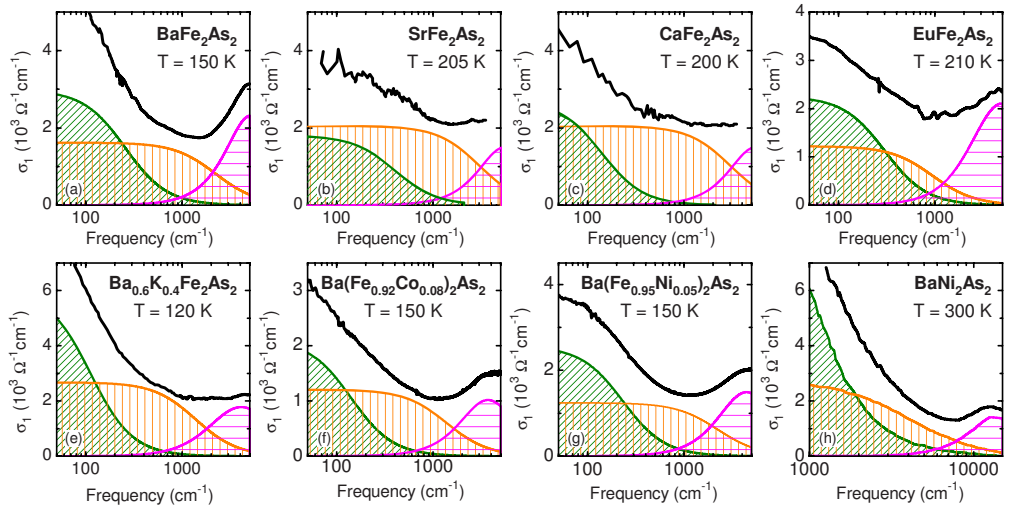

Figure 4.7: Optical conductivity of different iron-based superconductors. The black solid lines in each panel is the measured optical conductivity in the normal state, and the colorful shaded lines represent the components of the fit. Adopted from Ref. [85].

lines) for 8 different samples and components of the fit (colorful shaded lines) used for describing the optical conductivity in the normal state. We can see that for all the 8 different iron-based superconductors measured, the optical conductivity can be decomposed into three components: two Drude terms, accounting for the optical response of free carriers; one Lorentz term for interband transition. The two Drude terms description strongly indicates the presence of multiple Fermi surface sheets in iron-based superconductors. This is compatible with the dHvA effect measurements. Since Infrared spectroscopy is a k-averaged technique, it can not distinguish Fermi surfaces with similar mean free path. The Fermi sur-

faces of iron-based superconductors, observed by dHvA effect, are dominated by two groups of mean free paths, resulting in a two Drude bands description of the infrared optical response. They also found that in the doped compounds, both components are effected by the superconducting transition, suggesting that superconductivity may arise in multiple bands. A similar result is reported by Nakajima et al. [89].

Rullier-Albenque et al. systematically investigated the hole and electron contributions to the transport properties of Ba122 system compounds by studying their Hall coefficient as a function of temperature [116]. Figure 4.8 shows the tem-

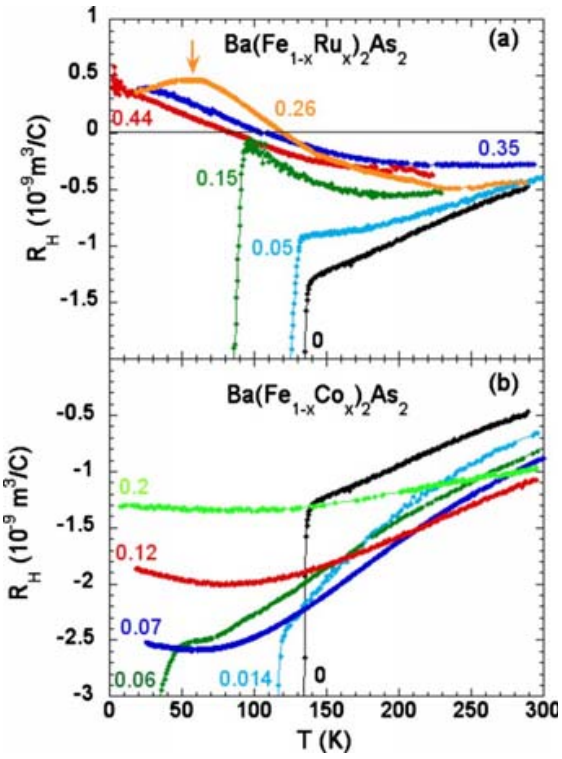

Figure 4.8: The Hall coefficient of $Ba(Fe_{1-x}Ru_x)_2As_2$ (Panel a) and $Ba(Fe_{1-x}Co_x)_2As_2$ (Panel b) as a function of temperature. Adopted from Ref. [116].

perature dependence of the Hall coefficient for $Ba(Fe_{1-x}Ru_x)_2As_2$ (Panel a) and $Ba(Fe_{1-x}Co_x)_2As_2$ (Panel b). A notable phenomenon occurs in $Ba(Fe_{1-x}Ru_x)_2As_2$

(x = 0.26, 0.35 and 0.44) samples: the Hall coefficient R_H increases with decreasing temperature, and more interestingly, a change in sign of R_H occurs roughly at 100 K as shown in panel (a). This pronounced sign change of the Hall coefficient provides substantial information about the carriers in these materials: (i) Both holes and electrons exist in $Ba(Fe_{1-x}Ru_x)_2As_2$ compounds, which is certainly expected in a multiband system with both hole-like and electron-like Fermi surface sheets. (ii) The hole and electron contributions to the transport properties are similar in a large temperature range. (iii) Different variations in hole and electron mobilities with temperature are strongly indicated by the Hall coefficient sign change. However, the Hall coefficient of $Ba(Fe_{1-x}Co_x)_2As_2$ is always found negative [117], as shown in Panel (b), implying that the transport properties are dominated by the electrons. These observations can explain the different shapes of the R-T curves for iron-based superconductors. Similar results are obtained by our infrared optical measurements in optimally doped $Ba_{1-x}K_xFe_2As_2$ which will be discussed in detail in Chapter 6.

4.2.6 Pairing symmetry

The superconducting condensation in iron-based superconductors may involve multiple bands. An unconventional pairing symmetry, the $s_\pm$ symmetry, is proposed for this family of superconductors [24]. Extensive experiments have been done with the aim at confirming the pairing symmetry in Ba122 system iron-based superconductors, but no consensus on the pairing symmetry, especially the existence of nodes in the order parameter, has been reached [75–77, 84, 118–125].

Ding et al. [118] performed an angle-resolved photoemission spectroscopy (ARPES) measurement on $Ba_{0.6}K_{0.4}Fe_2As_2$ single crystal with $T_c = 37$ K. In the normal state at $T = 50$ K, their data revealed three Fermi surface sheets: an inner hole-like FS pocket (the α FS) and an outer hole-like FS sheet (the β FS), both centered at the Γ point (the center of the Brillouin zone); an electron-like FS (the γ FS) centered at M point or $(\pi, 0)$. In the superconducting state, nearly isotropic and nodeless superconducting gaps with different values open simultaneously at the bulk T_c on all three observed Fermi surface sheets, as shown in Fig. 4.9. This signifies that the pairing order parameter in $Ba_{0.6}K_{0.4}Fe_2As_2$ has an s-wave

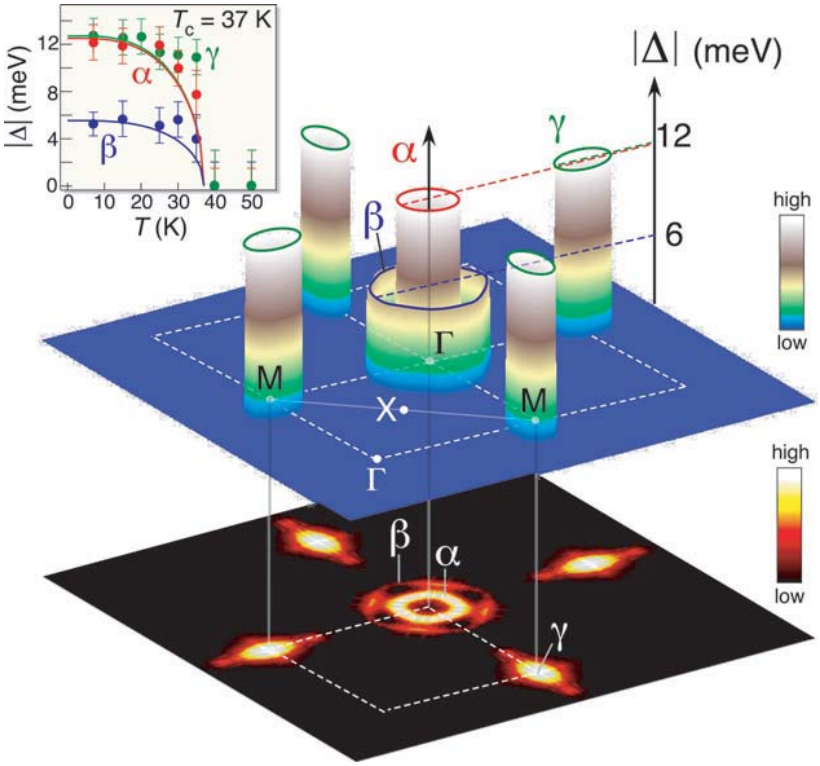

Figure 4.9: The contour of the superconducting gaps of $Ba_{0.6}K_{0.4}Fe_2As_2$ at 15 K measured by ARPES, adopt from Ref. [118]. The gap values are approximately 12 meV, 6 meV, and 12 meV on the α, β, and γ Fermi surface sheets respectively. Each gap has an s-wave symmetry.

symmetry. But ARPES is not a phase sensitive technique. Therefore, they can not rule out the possibility of phase reversal between the order parameters on the different FS sheets.

STM measurements on the same sample, reported by Shan et al., give similar results [122]. The left column in Fig. 4.10 shows the STM spectra measured at different positions on the sample surface in the superconducting state ($T = 3$ K). The two peaks (located at about 3 and 8 meV) feature is a strong signature of two superconducting gaps in this system, and the bottom of these curves are flat to zero strongly indicating that the gaps observed by STM are nodeless. They

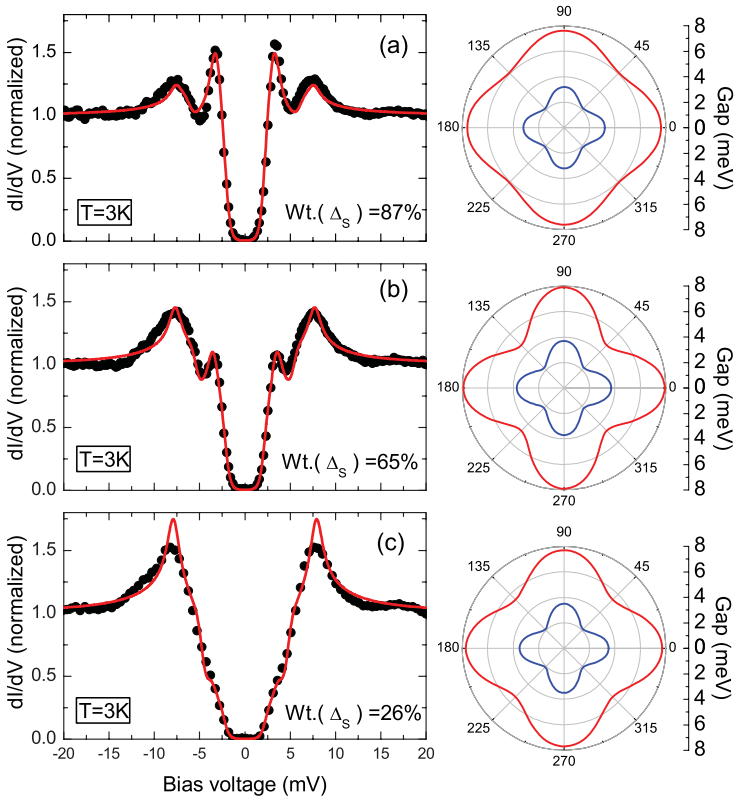

Figure 4.10: The left column depicts the spectra measured at different positions on the sample surface (black dots). The smooth lines through the dots are the fit with two-band model. The right column shows the gap functions for the two gaps utilized in the fitting [122].

obtained two gap values $\Delta_S = 3.3$ meV and $\Delta_L = 7.6$ meV by fitting their data to a multipeak Gaussian function, but both values are smaller than the ones determined by ARPES [118].

Terashima et al. investigated the Fermi surfaces and the properties of the superconducting gaps of the optimally electron doped $BaFe_{1.85}Co_{0.15}As_2$ single crystal with T_c =25.5 K [120]. Unlike the hole-doped system, they found that at the Γ point, the inner band, which is referred to as the α band in $Ba_{1-x}K_xFe_2As_2$, sinks significantly and does not create a small FS pocket as observed in the hole-doped samples [118]. The outer band (the β band) crosses the Fermi level creating

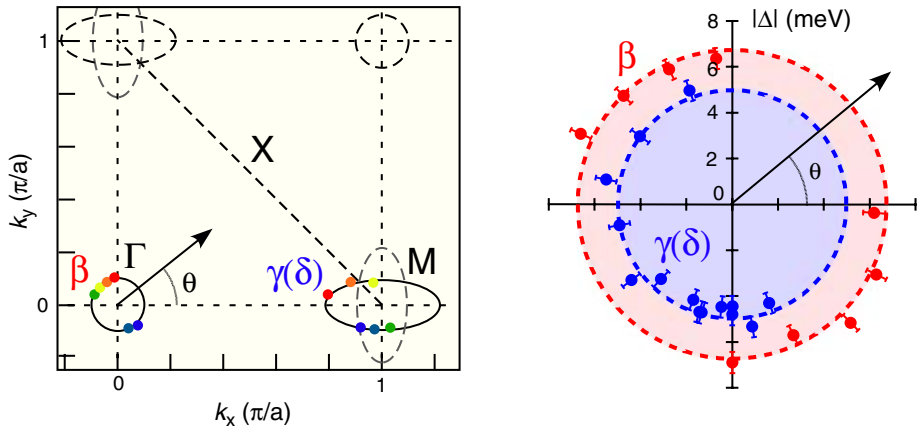

Figure 4.11: The left panel shows the structure of the Fermi surfaces extracted from the ARPES measurements. The right panel shows the gap symmetry and values on different Fermi surfaces. Dashed circles represent the averaged gap value.

a hole-like pocket centered at the Γ point. Near the M point, two electron-like Fermi surface sheets are observed, and these two Fermi surface sheets consist of the inner (γ) and outer (δ) pockets resulting from the hybridization of 2 ellipsoidal pockets elongated along the k_x and k_y direction. The shape of the Fermi surfaces is shown in the left panel on Fig. 4.11. Below T_c, at 8 K, the superconducting gaps with different values open on multiple Fermi surfaces centered at the Γ and M points. The gap on the β hole-like Fermi surface centered at Γ point has a value of 6.7 meV and gaps on the γ and δ electron-like Fermi surfaces near the M points have a value of 4.5 meV. The superconducting gap on each Fermi surface is nodeless and exhibits nearly isotropic behavior. The right panel of Fig. 4.11 displays the gap symmetry and values on different Fermi surfaces.

Using Scanning Tunneling Spectroscopy, Teague et al. also observed two-gap features on the electron doped $Ba(Fe_{1-x}Co_x)_2As_2$ single crystals [121]. The gap values determined from their STS spectra are $\Delta_\Gamma = 10.0$ meV and $\Delta_M = 5.0$ meV for x = 0.12 sample; $\Delta_\Gamma = 8.0$ meV and $\Delta_M = 4.0$ meV for x = 0.06 sample. In contrast to the hole doped $Ba_{1-x}K_xFe_2As_2$, relatively high zero-bias conductance

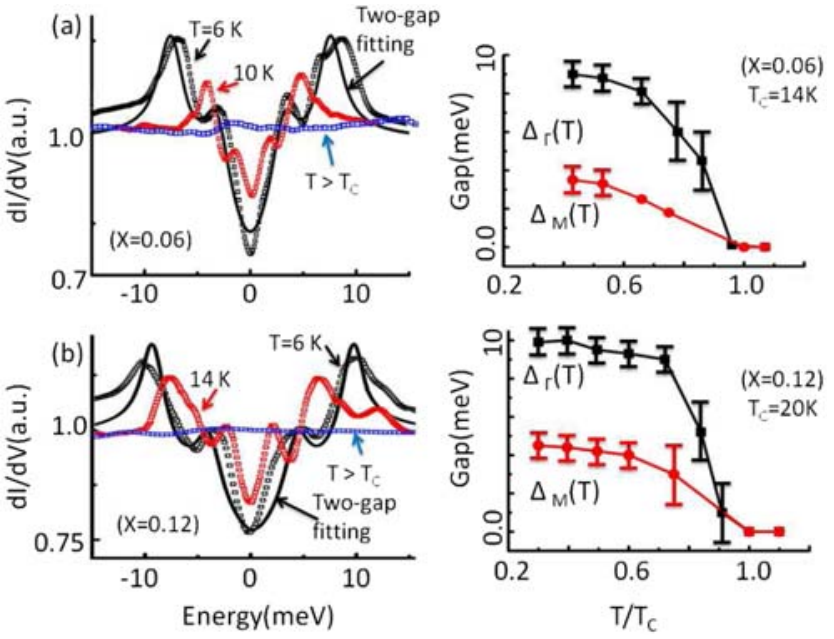

Figure 4.12: Adopted from Ref. [121], the left column shows the normalized tunneling conductance (dI/dV) vs bias voltage (V) for the two samples. Excess zero-bias conductance exists in all tunneling spectra at $T \ll T_c$. Right panel: the tunneling gaps Δ_Γ and Δ_M as a function of the reduced temperature (T/T_c).

exists in all tunneling spectra at $T \ll T_c$, as shown in Fig. 4.12. They attribute the excess zero-bias conductance to significant unitary impurity scattering in sign-changing s-wave superconducting gaps, and also suggest a possible source for the unitary impurity as disorder in the FeAs planes caused by Co in-plane doping.

In addition, lots of experimental results from optical spectroscopy exist on the Ba122 system [75–92]. Figure 4.13 shows some optical measurements on both Co and K doped Ba122 system compounds. Gorshunov et al. measured the optical conductivity of $Ba(Fe_{0.9}Co_{0.1})_2As_2$ ($T_c = 20$ K) as shown in panel (a), below T_c, the opening of the superconducting gap, characterized by a suppression of the low frequency $\sigma_1(\omega)$, is clearly observed. However, a strong quasiparticle absorption shows up below ~ 12 cm^{-1}. A single s-wave Mattis-Bardeen descrip-

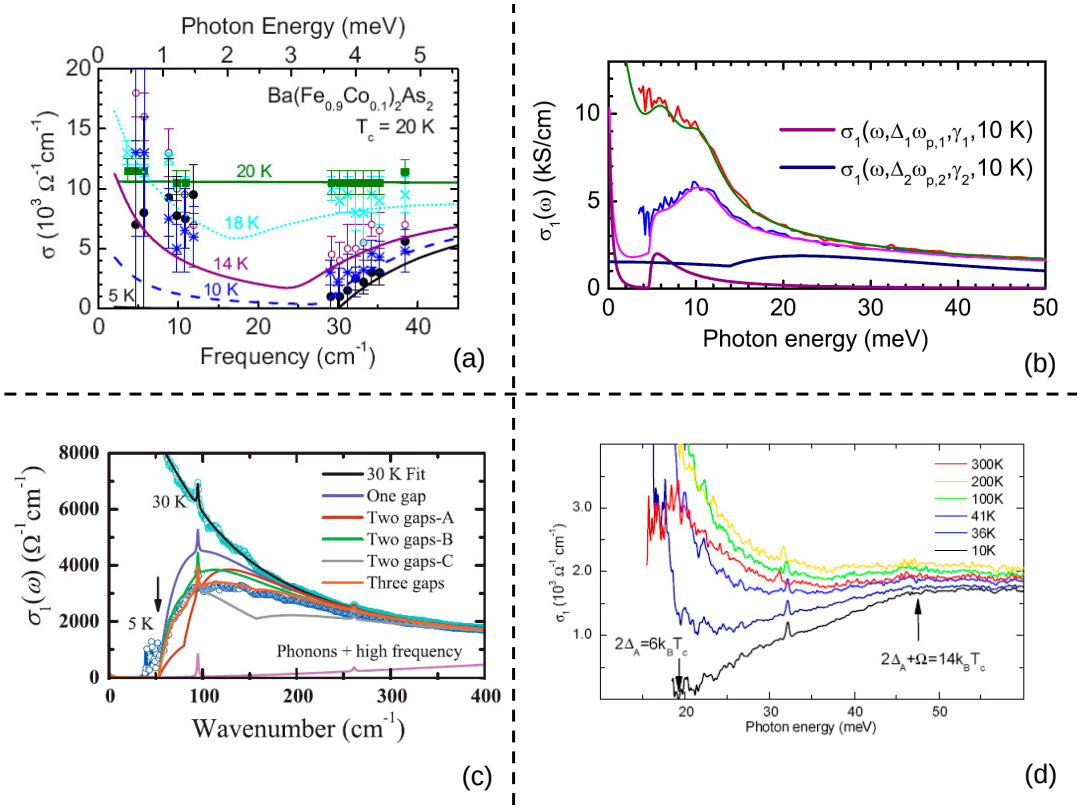

Figure 4.13: (a) Optical conductivity of $Ba(Fe_{0.9}Co_{0.1})_2As_2$ ($T_c = 20$ K) at several temperatures above and below T_c, the smooth lines through the data are BCS fits, adopted from Ref. [83]. (b) Optical conductivity of $Ba(Fe_{0.93}Co_{0.07})_2As_2$ ($T_c = 23$ K) measured at 24 K (red line) and 10 K (blue line). The green smooth line is the fit to the normal state data and the pink smooth line is the 10 K fit which consists of two Mattis-Bardeen conductivities, adopted from Ref. [81]. (c) Optical conductivity of $BaFe_{1.87}Co_{0.13}As_2$ ($T_c = 24.5$ K) measured at 30 K and 5 K. The smooth lines are fits with different parameters. Note that the fit with three gaps (orange line) can describe the measured optical conductivity very well. Adopted from Ref. [77]. (d) Optical conductivity of $Ba_{0.68}K_{0.32}Fe_2As_2$ ($T_c = 38.5$ K) at selected temperatures above and below T_c, adopted from Ref. [126].

tion fails at low frequencies [83]. Panel (b) shows the optical conductivity of $Ba(Fe_{0.93}Co_{0.07})_2As_2$ (T_c = 23 K) measured by Heumen et al. [81]. The red and blue curves are the measured $\sigma_1(\omega)$ at 24 K and 10 K respectively; the green and pink smooth curves are corresponding fits. They describe their superconducting state data (at 10 K) with a superposition of two Mattis-Bardeen conductivity representing two superconducting gaps, shown as the dark blue and purple lines in panel (b). Kim et al. measured the far-infrared optical conductivity of $BaFe_{1.87}Co_{0.13}As_2$ (T_c = 24.5 K) with ellipsometry [77], as shown in Panel (c). The open circles are the experimental data measured at 30 K and 5 K. They fit their superconducting data using different parameters (smooth lines) and found that three superconducting gaps (orange line) give a good description to the low frequency optical response in the superconducting state. The gap values obtained by Kim et al. are compatible with other techniques. Panel (d) displays the optical conductivity of $Ba_{0.68}K_{0.32}Fe_2As_2$ (T_c = 38.5 K) measured by Charnukha et al. [126]. At 10 K, the optical conductivity below $\sim$ 20 meV vanishes, indicating a fully open gap in this material. They described their ellipsometry data in the framework of a multiband Eliashberg theory with two superconducting gaps $2\Delta_1 \approx 6k_BT_c$ and $2\Delta_2 \approx 2.2k_BT_c$ which fall within the reported range for this material.

4.2.7 Pairing mechanism

The pairing mechanism is another crucial issue in understanding the superconductivity in iron-pnictides. Theoretical calculations by Mazin et al. suggest antiferromagnetic spin fluctuations mediated superconductivity in these materials [24], as many believe is the case in cuprates, heavy fermion superconductors, or ruthenates.

Christianson et al. reported an inelastic neutron scattering study on an optimally doped $Ba_{0.6}K_{0.4}Fe_2As_2$ sample with T_c = 38 K [127]. Figure 4.14 shows the inelastic neutron scattering intensity as a function of energy transfer. Data shown in the left panel are measured at 7 K (superconducting state) using incident neutron energies of 15 meV (yellow circles), 30 meV (blue circles) and 60 meV (green circles). A well defined resonant peak can be see at $\sim$ 14 meV

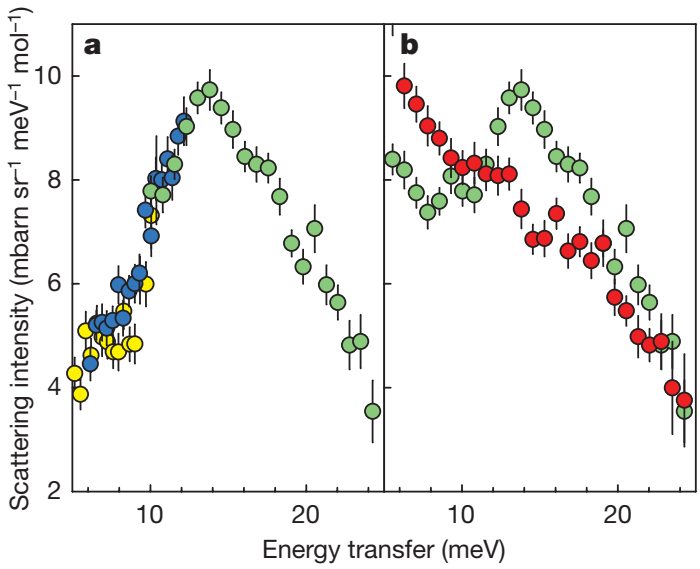

Figure 4.14: The inelastic neutron scattering intensity for $Ba_{0.6}K_{0.4}Fe_2As_2$. The left panel shows the data measured at 7 K using incident neutron energies of 15 meV (yellow circles), 30 meV (blue circles) and 60 meV (green circles). The right panel shows the data measured at 50 K (red circles) and 7 K (green circles) using an incident neutron energy of 60 meV. Adopted from Ref. [127].

for all the incident neutron energies. At 50 K (normal state), the resonant peak is absent, shown as the red circles in the right panel. This resonance peak has also been observed in copper oxide superconductors and several heavy-fermion superconductors. It is predicted that when the sign of the superconducting gap reverses on different parts of the Fermi surface and the electron pairing interaction is repulsive at short range, the resonant peak is present in the superconducting state. Here, the presence of this resonant peak in the superconducting state may imply an antiferromagnetic spin fluctuation mediated superconductivity in $Ba_{0.6}K_{0.4}Fe_2As_2$.

All in all, multiband features have been observed in the Ba122 system compounds by a variety of techniques. However, the properties of the order parameter and the pairing mechanism in iron-based superconductors remains unclear. Further experiments and understanding are still highly desired.

Chapter 5

Experimental Methods

Many and various approaches can be used to measure the frequency dependent optical properties of solids, these approaches are classified in to three categories with different principles. The frequency domain spectroscopy measures the optical response as a function of frequency in a straightforward manner by applying monochromatic radiation and measuring the amplitude and phase of the response at one frequency ω. In order to evaluate the frequency dependent optical constants, the measurement has to be repeated for each frequency of interest. For the time domain spectroscopy, instead of measuring the response of a solid by applying monochromatic radiation varied over a wide frequency range, the optical constants are obtained by performing the experiment in the time domain using a voltage pulse which contains all the frequencies of interest. In time domain transmission spectroscopy, a femtosecond laser pulse is split along two paths and excites a pair of photoconductive antennae deposited on radiation damaged silicon on sapphire. A broadband pulse is emitted by one antenna, transmitted through the sample and measured at the other antenna. By varying the length difference of the two paths, the electric field of the transmitted pulse is mapped out as a function of time. The complex transmission coefficient can be obtained by comparing the Fourier transform of the transmission through the sample to that of a reference. Time domain spectroscopy mainly operates in the frequency range of Terahertz. Another method used to derive the optical constants of solids refers to the Fourier transform spectroscopy. This technic is based on the Michelson interferometer in which a beam of polychromatic light is split into two approximately equal parts at the beamsplitter. These two parts follow different paths and finally recombine at the beamsplitter. The intensity of the recombined light that shows an interference pattern is a function of the rel-

ative difference in path length between the two arms. The frequency dependent intensity of the light can be derived from the intensity of the recombined beam as a function of optical path difference through a Fourier transform. The Fourier transform spectroscopy is widely used in the infrared-visible-UV spectral range (from 10 cm^{-1} to 55000 cm^{-1}) which covers the characteristic energy scales in solids. In this thesis, all our measurements are performed on Fourier transform spectrometers and fiber optics spectrometer. We will introduce the principles and the setup of our Fourier Transform Infrared Spectrometers and fiber optics spectrometer, and sample preparation in this chapter.

5.1 Principles of Fourier Transform Infrared Spectroscopy

In order to explain the principles of Fourier transform spectroscopy, discussing a simple Michelson interferometer is a good start. Figure 5.1 shows the

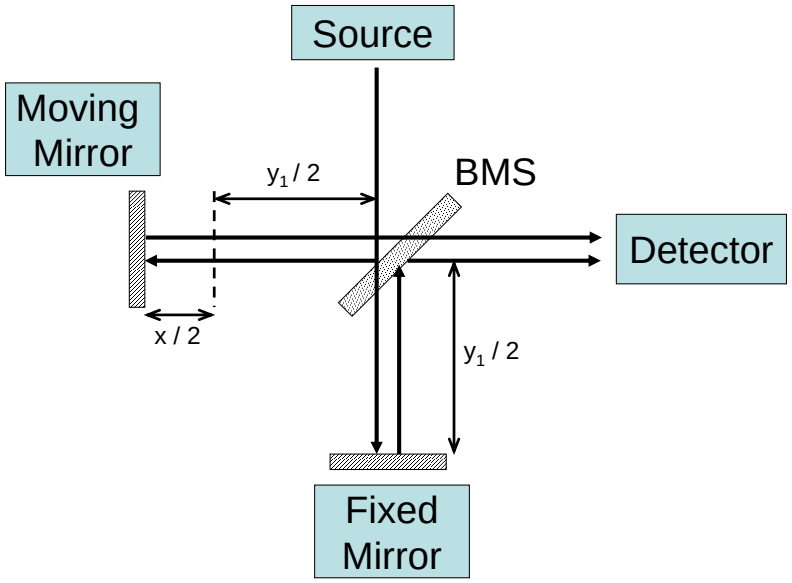

Figure 5.1: Schematic representation of a simple Michelson interferometer. The beamsplitter locates in the center of the interferometer where the beam from the source is divided into two parts. One arm of the interferometer consists of a fixed mirror while the other arm comprises a moving mirror.

schematic view of a simple Michelson interferometer. The beam from the source is split into two approximately equal beams at the beamsplitter (BMS). One beam is reflected by the moving mirror while the other by the fixed mirror, and finally are brought together again at the beamsplitter. The recombined beam with an interference pattern proceeds to the sample area and the detector.

Consider a monochromatic plane wave incident on the beamsplitter with a form

$$E = E_0 \cos(\omega t - 2\pi\nu y) \tag{5.1}$$

where E_0 is the average electric field amplitude; ω is the frequency and ν is the wave number with a unit of cm^{-1} defined as

$$\nu = \frac{1}{\lambda} = \frac{\omega}{2\pi c} \tag{5.2}$$

c is the speed of light. The beam is divided into two at the beamsplitter. The one to the fixed mirror first passes through the beamsplitter, then is reflected by the fixed mirror, finally reflected by the beamsplitter to the detector. It can be written as

$$E_1 = rtCE_0 \cos[\omega t - 2\pi\nu y_1] \tag{5.3}$$

where r is the reflectance of the beamsplitter; t is the transmittance; C is a constant depending on the polarization. The other beam is first reflected by the beamsplitter, then by the moving mirror, and finally passes through the beamsplitter. It can be written as

$$E_2 = rtCE_0 \cos[\omega t - 2\pi\nu(y_1 + x)] \tag{5.4}$$

where x is the path difference or the mirror displacement. These two beams recombine at the beamsplitter. By superimposing, the resultant electric field E is given by

$$E_R = E_1 + E_2 = 2rtCE_0 \cos(\omega t - 2\pi\nu y_1) \cos(\pi\nu x) \tag{5.5}$$

The intensity (I) detected by the detector is the time average of E^2

$$I \propto 4r^2t^2C^2E_0^2 \cos^2(\omega t - 2\pi\nu y_1) \cos^2(\pi\nu x) \tag{5.6}$$

where the time average of the first cosine term is just 1/2. Thus

$$I \propto 2I(\nu)\cos^2(\pi\nu x) \tag{5.7}$$

where $I(\nu)$ is a constant that depends only on ν. This expression simplifies

$$I(x) = I(\nu)[1 + cos(2\pi\nu x)] \tag{5.8}$$

where $I(x)$ is the interferogram of a monochromatic source. As shown in Fig. 5.2.

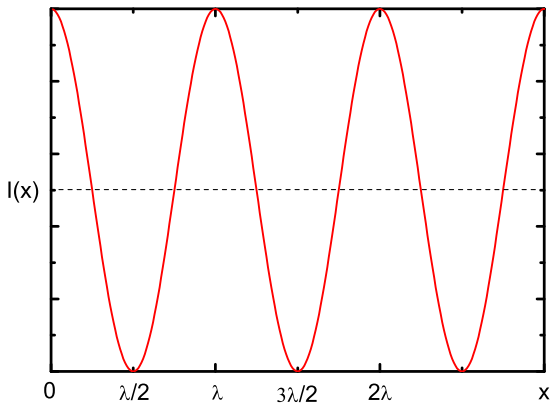

Figure 5.2: The interferogram of a monochromatic source (a laser for instance).

The source used in Fourier transform spectrometer is a polychromatic preferably continuous source. We collect the information of all different wave numbers at the same time and sort it out utilizing a Fourier transform. Hence, the measurement time is substantially decreased. An interferogram for a polychromatic source which covers a frequency range from 0 to ν_m may be obtained by integrating Eq. 5.8

$$\begin{aligned} I(x) &= \int_0^{\nu_m} I(\nu)[1 + \cos(2\pi\nu x)]d\nu \\ &= \int_0^{\nu_m} I(\nu)d\nu + \int_0^{\nu_m} I(\nu)\cos(2\pi\nu x)d\nu \end{aligned} \tag{5.9}$$

when $x = 0$, we get

$$I(0) = 2\int_0^{\nu_m} I(\nu)d\nu \tag{5.10}$$

then Eq. 5.9 becomes

$$I(x) = \frac{1}{2}I(0) + \int_0^{\nu_m} I(\nu)\cos(2\pi\nu x)d\nu \tag{5.11}$$

An ideal interferogram of polychromatic source, as shown in Fig. 5.3, is symmetrical about $x = 0$ where the interference between all of the frequencies is constructive, leading to a central maximum. For $x = \infty$, since the frequencies

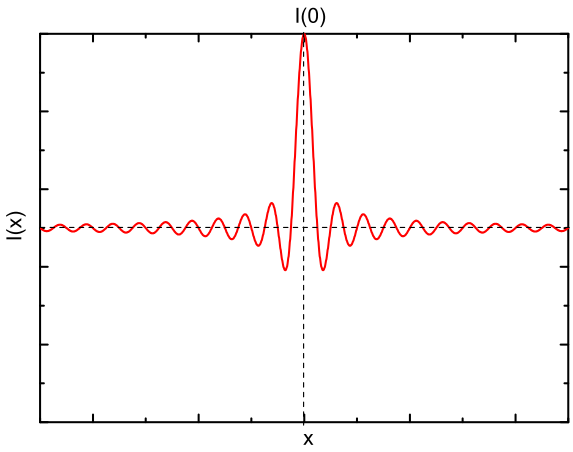

Figure 5.3: An ideal interference pattern of a polychromatic source calculated from Eq. 5.11. Note that $I(0) = 2I(\infty)$.

superimpose both constructively and destructively, the net contribution due to the integral in Eq. 5.11 is zero, then we can get

$$I(\infty) = \frac{1}{2}I(0) \tag{5.12}$$

the substitution of $I(\infty)$ for $I(0)/2$ in Eq. 5.11 yields

$$I(x) - I(\infty) = \int_0^{\nu_m} I(\nu)\cos(2\pi\nu x)d\nu \tag{5.13}$$

letting $\nu_m \to \infty$, using the Fourier transform, the frequency dependent intensity $I(\nu)$ can be derived from the intensity as a function of path difference $I(x)$

$$I(\nu) = \int_0^{\infty} [I(x) - I(\infty)]\cos(2\pi\nu x)dx \tag{5.14}$$

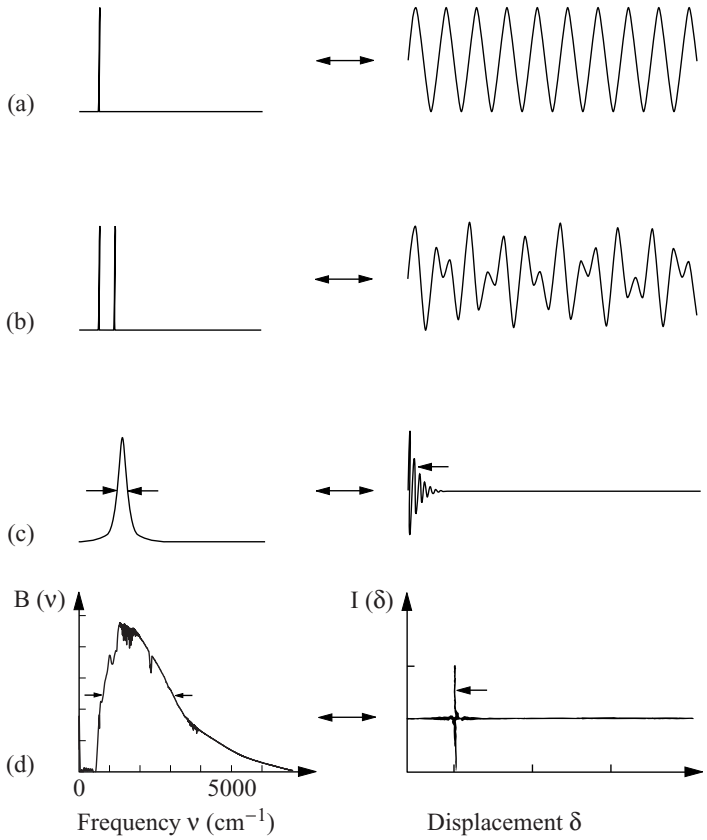

Figure 5.4: Typical spectra collected by the interferometer and their Fourier transforms. Adapted from Ref. [56].

In practice, the interferogram is measured only over a finite mirror displacement, i.e. $x \leq x_{max}$. To extend it beyond the measured x, we use apodization functions instead of cutting it abruptly off. Figure 5.4 shows different spectra obtained by the interferometer and their Fourier transforms. δ is the mirror displacement.

5.2 FTIR spectrometers

The DA8 FTIR spectrometer in the lab of IOP CAS is manufactured by ABB Bomen in Canada. By utilizing a variety of sources, beamsplitters and detectors, spectra can be collected over a frequency range from approximately 20 cm^{-1} to 25000 cm^{-1} with spectral resolution from 4 cm^{-1} to 0.02 cm^{-1}. Scanning velocities from 0.01 to 4 cm/s are available for the moving mirror. The time

for a single scan ranges between seconds to minutes depending on the required spectral resolution and the scanning velocity. Fast Fourier transform (FFT) of the measured interferogram is performed by a vector processor which provides an interface between the DA8 and a controlling personal computer. The instrument control and data acquisition are achieved via the software program PCDA.

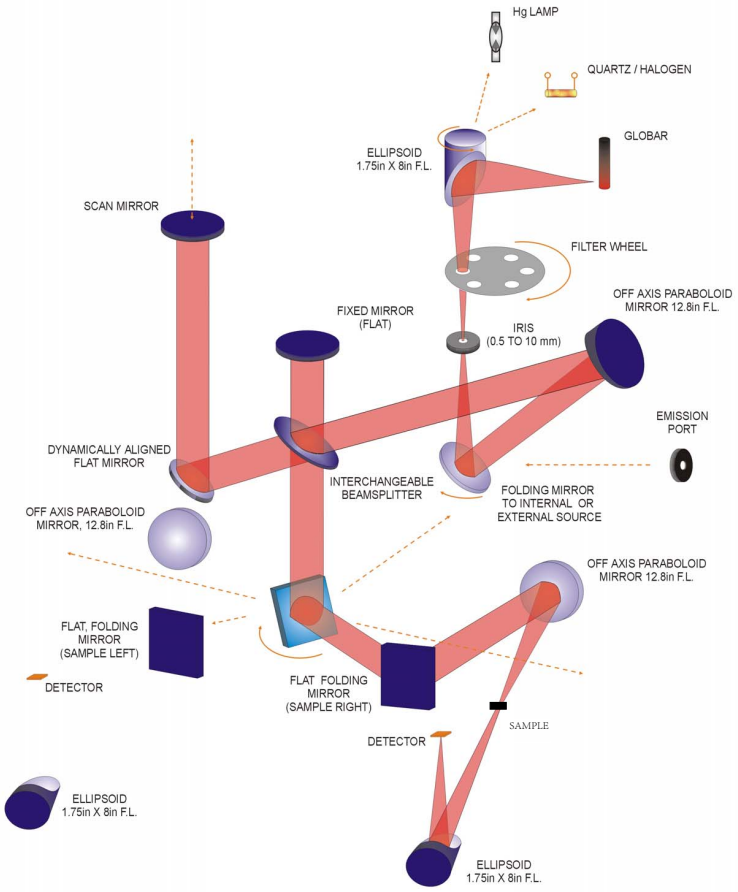

Figure 5.5: Schematic plot of the optical beam path for the DA8 spectrometer.

Figure 5.5 displays a schematic plot of the optical beam path for the DA8 spectrometer. Three internal sources locate at the top of the spectrometer. Light from one of the sources is focused onto a mechanical iris by an off-axis ellipsoidal Al mirror. The diameter of the iris is adjustable from 0.5 to 10 mm, and the aperture size determines the size of the source image to be focused on the sample.

Below the iris, a flat mirror reflects the diverging beam to an off-axis paraboloid Al mirror. The off-axis paraboloid mirror collimates the light for processing in the Michelson arms. This collimated beam is divided into two approximately equal beams at the beamsplitter. Upon reflection from their respective mirrors, these two beams are brought together again at the beamsplitter and proceed towards the sample selection mirror which sits just below the beamsplitter. This mirror rotates to direct the output beam to one of two sample locations. An off-axis paraboloid mirror refocuses the collimated beam onto the sample. After passing through the sample, the diverging beam is focused onto the detector by another off-axis paraboloid mirror. The whole optical beam path system shown in Fig. 5.5 is set up in vacuum to mitigate the water absorption lines which are particularly strong in the infrared range.

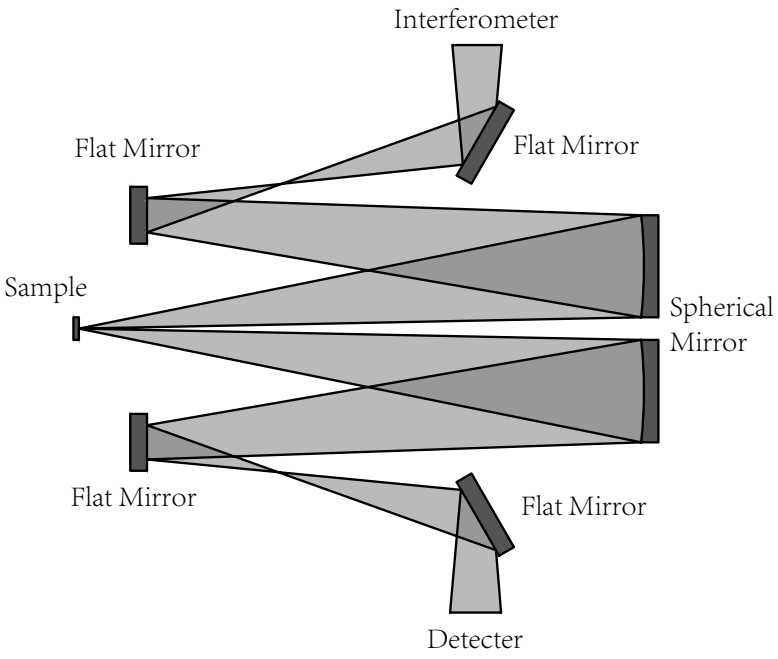

Figure 5.6: The geometry of the reflectivity measurement for ABB Bommen DA8 FTIR spectrometer.

The optical path for the sample measurement shown in Fig. 5.5 illustrates

the transmission configuration. Figure 5.6 shows the geometry of the reflectivity measurement. It consists of four flat and two spherical mirrors. Focused sample beam from the interferometer is reflected by the first flat mirror. Passing the focal point, the beam becomes diverging. The second flat mirror redirects the diverging beam to the first spherical mirror which refocuses the source image on the sample. Upon reflecting from the sample, the second spherical and two flat mirror direct the beam into the detector.

The FTIR spectrometers in ESPCI Paris are Bruker IFS 66v/s and IFS 113v which are manufactured by Bruker Optics in Germany. Fig. 5.7 shows a

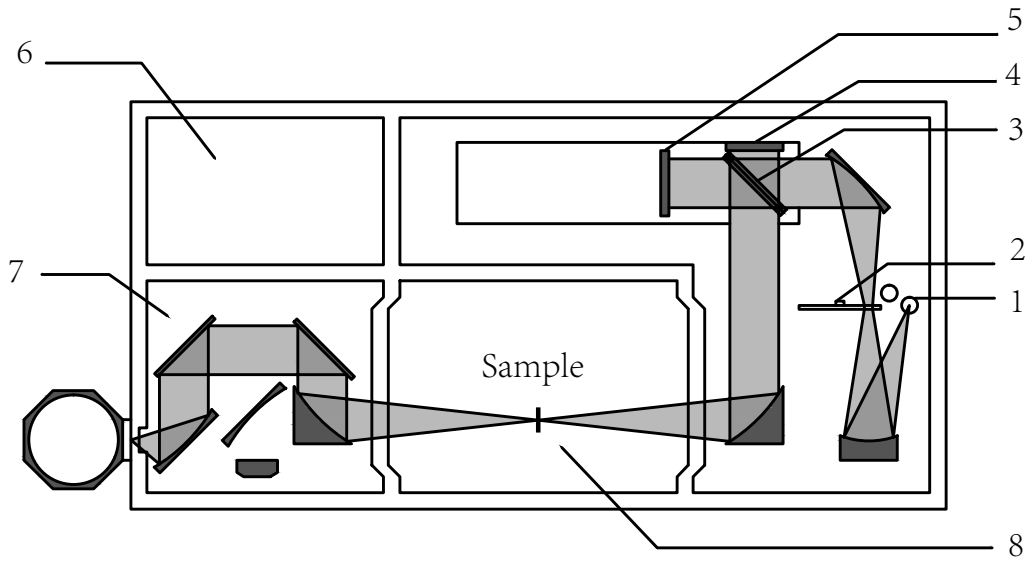

Figure 5.7: Schematic representation of Bruke IFS 66v/s FTIR spectrometer. 1. source; 2. the aperture wheel; 3. beamsplitter; 4. fixed mirror; 5. moving mirror; 6. controlling circuit chamber; 7. detector chamber; 8. sample chamber. The plot is not in real ratio.

schematic representation of the Bruker IFS 66v/s FTIR spectrometer. The whole spectrometer is composed of several chambers. The right part is the interferometer chamber. The main components in this chamber are the sources and the Michelson interferometer. A spherical Al mirror focuses light from one of two

internal sources onto an aperture wheel with a series of different size apertures. Passing through the aperture, the diverging beam is collimated and diverted into the Michelson interferometer by an off-axis ellipsoidal Al mirror at the input of the interferometer. Another off-axis ellipsoidal mirror at the output of the interferometer focuses and directs the output beam onto the sample in the sample chamber which is in the middle front part of the spectrometer. Transmitted through the sample, the diverging beam proceeds into the detector chamber that lies in the left front part of the spectrometer. The detector chamber consists of several detectors and mirrors. By changing the position and orientation of the mirrors, light coming from the sample chamber can be directed into different detectors. The left back part of the spectrometer is the controlling circuit chamber which contains the controlling circuits and the analog to digital converter.

The reflectivity measurement configuration for the Bruker spectrometers is shown in Fig. 5.8. When performing the reflectivity measurement on the Bruker

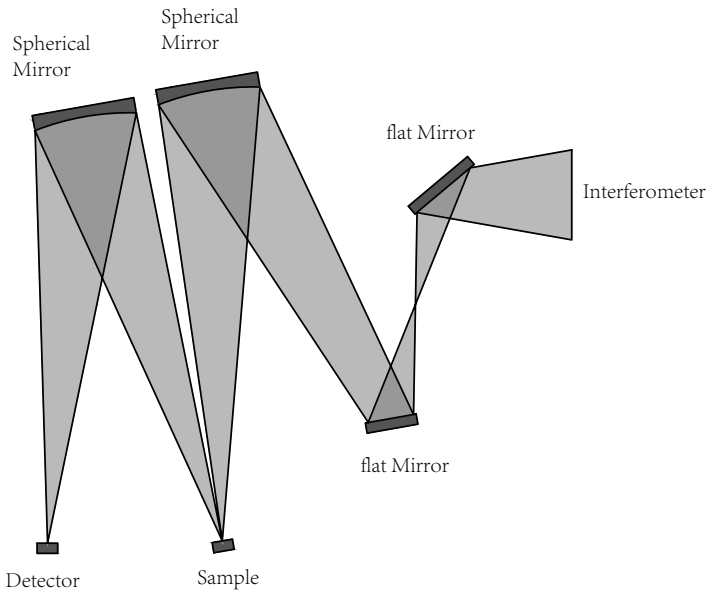

Figure 5.8: The geometry of the reflectivity measurement for Bruker IFS 66v/s and IFS 113v FTIR spectrometers.

spectrometers, this part is set in the sample chamber. The sample is moved out of the chamber and mounted in a cryostat sitting just in front of the sample chamber. The detector is also moved out of the detector chamber and mounted beside the sample cryostat. The reflectivity measurement configuration consists of only two flat and two toroidal mirrors. The output beam of the interferometer is conducted by the two flat mirrors onto a toroidal mirror. The orientation of this toroidal mirror can be adjusted, so it can focuses the beam onto the sample. By adjusting the orientation of the sample, the beam is reflected onto the second toroidal mirror by the sample. The orientation of the second toroidal mirror is also adjustable. Finally, the diverging beam from the sample is refocused by the second toroidal mirror directly onto the detector.

The Fourier transform infrared spectrometers cover a very broad frequency range from approximately 10 cm^{-1} to 25000 cm^{-1}. In order to achieve the spectra over such a broad frequency range, a series of combinations of source, beamsplitter and detector are needed for data collection. Table 5.1 lists the spectral range for several optical elements including sources, beamsplitters and detectors.

The spectrometers are equipped with three internal broadband blackbody radiation sources: mercury arc, globar and quartz tungsten halogen. The mercury arc is a mercury vapor discharge lamp that uses mercury in an excited state to produce light. It emits best in the far infrared range below approximately 200 cm^{-1}. Globar is a silicon carbide rod. When electrically heated up, it emits radiation from far to near infrared. The globar source operates best in the frequency range from 50 cm^{-1} to 10000 cm^{-1}. The quartz tungsten halogen source makes light by heating the tungsten filament wire to a very high temperature until it glows. It produces radiation with a broad frequency range from 2000 cm^{-1} to 25000 cm^{-1}.

Many and various beamsplitters are provided for the Fourier transform spectrometers. In the far infrared range, Mylar with different thicknesses are widely used as beamsplitters. The different thicknesses of Mylar optimize spectrometer throughput in a narrow spectral range about the interference maxima in the Mylar pellicle. The KBr, CaF_2 and Quartz beamsplitters used for the mid and near

	Optical elements	Spectral range [cm^{-1}]
Source	Mercury arc	5 - 200
	Globar	50 - 10000
	Tungsten	2000 - 25000
Beamsplitter	50 μm Mylar	10 - 60
	25 μm Mylar	20 - 120
	Silicon 3 mm	10 - 600
	Mylar:Ge (T222)	30 -680
	KBr:Ge	370 - 7800
	CaF_2	1900 - 25000
	Quartz	4000 - 25000
Detector	4.2 K Silicon Bolometer	5 - 700
	4.2 K Photoconductor	350 - 5000
	77 K HgCdTe	420 - 12000
	DTGS	250 - 12000
	77 K InSb	1850 - 12800
	Silicon Diode	9000 - 25000

Table 5.1: Spectral range for some frequently used optical elements including sources, beamsplitters and detectors.

infrared are designed based on a different principle. These beamsplitters consist of a plate of non-absorbing substrate material with a semi-reflecting film on it. For example, the KBr beamsplitter is a plate of KBr with a thin coating of Ge which has appropriate thickness so that half of the light incident at a 45 degree angle is transmitted, and the remainder reflected. In recent years, a thick (several millimeters) silicon wafer is used as beamsplitter in the far infrared range [128, 129]. This silicon beamsplitter operates effectively well in the frequency range from 10 cm^{-1} to 600 cm^{-1} and can replace several Mylar beam splitters to span the entire far infrared range. Care is needed when handling the beamsplitters. For instance, Mylar beamsplitters are vulnerable to UV radiations, so a filter should be used to shield the UV component of the mercury arc. The KBr

beamsplitter is extremely hygroscopic and should be stored in a low humidity dry box.

Photodetectors are classified into three categories: photovoltaic, photoconductive, and thermal. The Bolometer used in the far infrared range is a thermal detector. It measures the power of electromagnetic radiation via the heating of a material with a temperature-dependent electrical resistance. The 4.2 K Photoconductor and HgCdTe (MCT) detectors are classified into the photoconductive category. If light is absorbed by a photoconductive material, like HgCdTe, the number of free carriers in the material increases and raises its electrical conductivity. When applying a bias voltage to the material, the corresponding current is proportional to the power of the light absorbed by the material. InSb and Si detectors fall into the photovoltaic category. These detectors consist of photovoltaic materials which create DC voltage or corresponding current upon its exposure to light. Hence, the photovoltaic detectors measure the electromagnetic radiation by converting it into voltage or current. All the detectors come paired with a preamplifier specially matched to the detector's impedance and frequency roll-off. The preamplifiers increase the relatively weak detector signals to levels appropriate for analog to digital conversion (ADC), then, data acquisition can be performed.

Each source have its characteristic power spectra; the beamsplitters also have their own transmittance curves and the frequency response of different detectors shows strikingly dissimilar behavior. The measured power spectrum is given by the combination of all these factors. Figure 5.9 shows the power spectra and corresponding 100% lines for different combinations of source, beamsplitter and detector. The 100% lines are obtained by measuring the power spectra twice and dividing one by another. These spectra were measured on the Bruker IFS 66v/s FTIR spectrometer by Dr. Ricardo Lobo in ESPCI Paris. Note that the signal to noise ratio of the 100% lines becomes poor at both edges of the measuring range, but these measuring ranges have overlaps. The overall spectrum can be obtained by cutting off the edge data for each measuring range and merging them together.

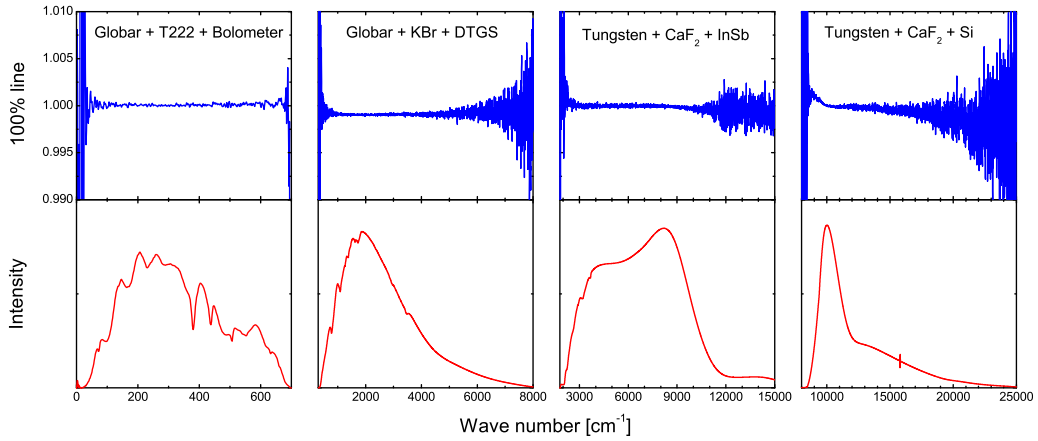

Figure 5.9: The power spectra and corresponding 100% lines for different combinations of source, beamsplitter and detector. Data were collected on the Bruder IFS 66v/s FTIR spectrometer by Dr. Ricardo Lobo in ESPCI Paris.

5.3 Fiber optic spectrometer

In our lab, we also have an Avaspec-2048 $\times$ 14 model fiber optic spectrometer manufactured by Avantes. Figure 5.10 shows the schematic plot of the fiber optic spectrometer with the reflectivity measurement configuration in our lab. It comprises a source (AvaLight-DHS), fibers with a probe head, a spectrometer (AvaSpec) and the PC. The light source is composed of a Deuterium lamp and a Halogen lamp which can cover the frequency range from near infrared to deep UV. The spectrometer consists of a fiber optic entrance connector, collimating and focusing mirror, diffraction grating, and 2048 pixels CCD linear array, as shown in the middle panel. The SMA-entrance connector can couple the light from a fiber onto the collimating mirror, then the light is reflected by the collimating mirror on the diffraction grating which splits and diffracts the light into beams propagating in different directions. The directions of these beams depend on the wavelength of the light. When the beams are collimated and diverted by the focussing mirror onto the detector (2048 pixels CCD linear array), the light intensity as a function of wavelength $[I(\lambda)]$ can be obtained. All these parts are integrated into a small box. The left part of the bottom panel displays the structure of the probe head of the fibers. It consists of 1 read fiber in the center

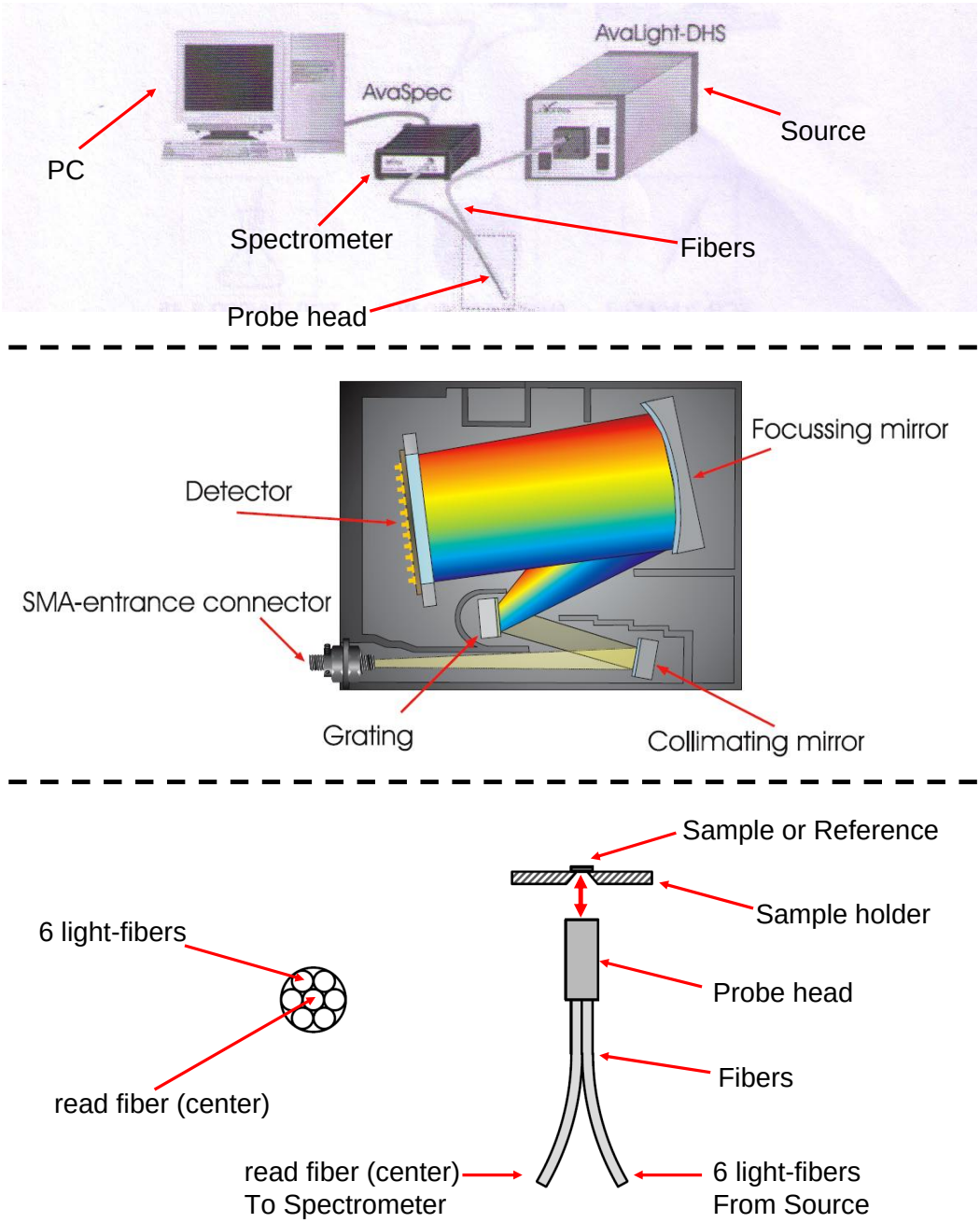

Figure 5.10: Schematic representation of Avaspec-2048 × 14 model fiber optic spectrometer.

and 6 light-fibers surrounding the read fiber. The read fiber is connected to the spectrometer while the 6 light fibers are connected to the source. Light from the source is coupled into the 6 light fibers and carried to the probe head. The sample is mounted facing the probe head. Light coming out from the 6 light fibers is reflected by the sample into the read fiber in the center of the probe head. This fiber transfers the light reflected by the sample to the fiber optic entrance connector which can couple the light into the spectrometer. The data acquisition is performed by an Avasoft-Basic software installed in a PC.

The right part of the bottom panel in Fig. 5.10 displays the schematic diagram of the sample mounting. The probe head is mounted face up and the sample is placed face down on the sample holder which has a cone-type hole towards the probe head. The light reflected by the cone-type hole does not enter the read fiber in the center of the probe head, so the read fiber only collects the light reflected by the sample. The reflectivity measurement procedure is as follows: (i) put the whole system in a dark environment, remove the sample or reference from the sample holder, and then save dark. We get the spectrum of the background I_{BG}. (ii) put an Al mirror (reference) face down on the sample holder, and make sure that the Al mirror can cover the hole on the sample holder completely, then save reference. We get $I_{Al+BG} - I_{BG}$. (iii) remove the Al mirror and put the sample on the sample holder. The sample should also cover the hole on the sample holder completely. Then save sample and we get $[I_{Sam+BG} - I_{GB}]/[I_{Al+BG} - I_{BG}]$. Finally we can get the reflectivity of the sample via

$$R_{sam} = \frac{I_{Sam+BG} - I_{BG}}{I_{Al+BG} - I_{BG}} \times R_{Al} \tag{5.15}$$

where R_{Al} is the absolute reflectivity of the Al mirror which can be measured with reference free methods like V-W, V-N and ellipsometry. With this fiber optic spectrometer, the frequency range of our data can be extended to the visible and UV range (9000 cm^{-1} to 55000 cm^{-1}) at room temperature.

5.4 *in situ* gold overfilling technique

As we discussed in Chapter 3, if we measure the reflectivity over a wide frequency range followed by a Kramers-Kronig analysis which yields the phase, all the frequency dependent complex optical constants can be easily calculated. But the newly discovered and most interesting single crystal materials are usually small and irregular in shape. Figure 5.11 shows the size and shape of an optimally

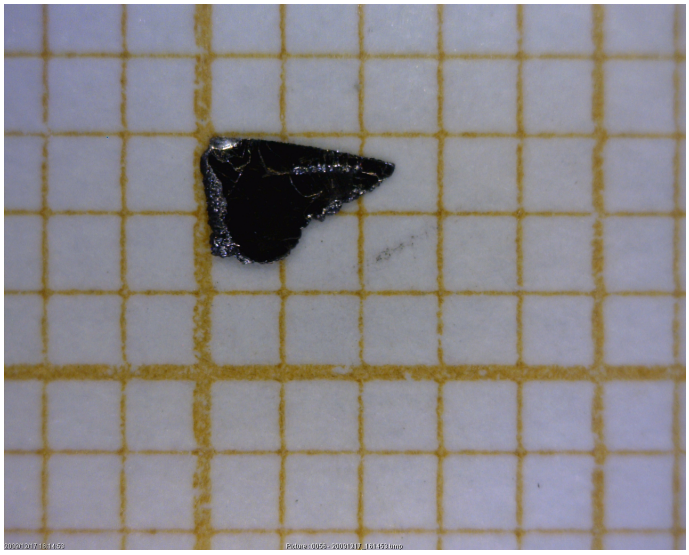

Figure 5.11: Picture of an optimally doped $Ba(Fe_{1-x}Co_x)_2As_2$ single crystal. The dimension of one small square on the graph paper is 1 mm by 1 mm.

doped $Ba(Fe_{1-x}Co_x)_2As_2$ single crystal. The dimension of one small square on the graph paper is 1 mm by 1 mm. From the picture we can see that the size of the sample is only about 1.5 mm by 1.5 mm. Besides the irregular shape, cleavage steps characterize the surface of the sample. Therefore, the reflectivity measurement becomes particularly difficult in the far infrared range ($\leq 200\text{cm}^{-1}$) because of the weakness of the mercury arc and the lack of photoconductive detectors.

The solution of these problems lies in the *in situ* gold overfilling technique [130]. With this technique, the entire area of the sample is utilized, and the geometrical effects due to rough surface can be corrected by coating the sample surface with a good metal (gold) and using the coated sample as its own reference

in reflectivity measurements. Figure 5.12 displays the schematic diagram of the

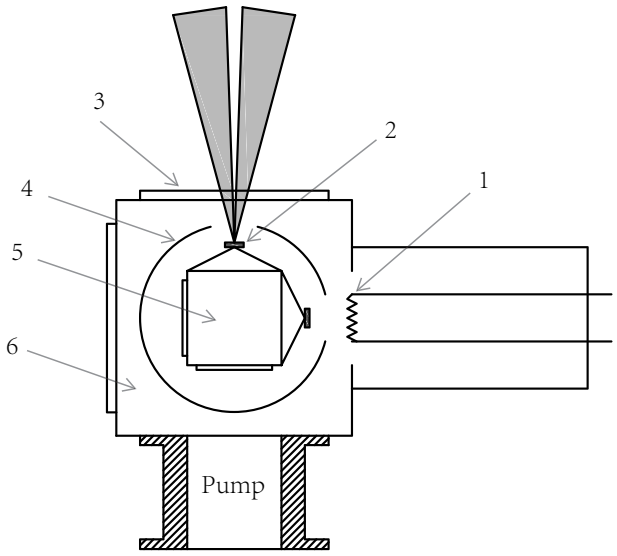

Figure 5.12: Schematic diagram of the *in situ* gold overfilling technique. 1. filament (spiral tungsten wire with gold wire wound on it); 2. sample or stainless steel mirror; 3. optical window; 4. aluminum radiation shield; 5. cold tail of cryostat with copper cone (sample holder); 6. vacuum shroud.

in situ gold overfilling technique. The whole setup is installed in a vacuum shroud labeled by number 6. The cold tail of cryostat with two copper cones locates in the center of the vacuum shroud. The sample and a stainless steel mirror are glued on the copper cones. An aluminum radiation shield protects the cold tail and the sample against the external radiation, so the sample can be cool down to the liquid helium temperature 4.2 K. The cold tail, together with the radiation shield can be rotated by 90 degree without breaking the vacuum. Label 1 denotes a length of tungsten wire which has been coiled to form a filament with gold wire wound on it. When applying a DC voltage of about 2 Volt, the filament glows and the gold is evaporated. This produces a layer of gold on the surface of the sample. The thickness of the gold layer is about several times of the classical skin depth even in the far infrared range ($\sim 100\text{cm}^{-1}$), which ensures that multiple

reflections do not occur.

The procedure of the reflectivity measurement with the *in situ* gold overfilling technique is as follows: (1) measure the single channel power spectrum of the stainless steel mirror, and thus we get I_{Mirror}; (2) rotate the cryostat and measure the single channel power spectrum of the sample, and we get I_{Sam}/I_{Mirror}; (3) evaporation; (4) measure the single channel power spectrum of the stainless steel mirror again; (5) rotate the cryostat and measure the single channel power spectrum of the coated sample, and we get $I_{CoatedSam}/I_{Mirror}$. Finally, we obtain the reflectivity of the sample

$$R_{Sam}(\omega) = \frac{I_{Sam}(\omega)/I_{Mirror}(\omega)}{I_{CoatedSam}(\omega)/I_{Mirror}(\omega)} \times R_{gold} \tag{5.16}$$

The use of a stainless steel reference mirror is to reduce the influence of system drift. With the *in situ* gold overfilling technique, the measured reflectivity has absolute accuracy better than 0.5% and a relative accuracy better than 0.1%.

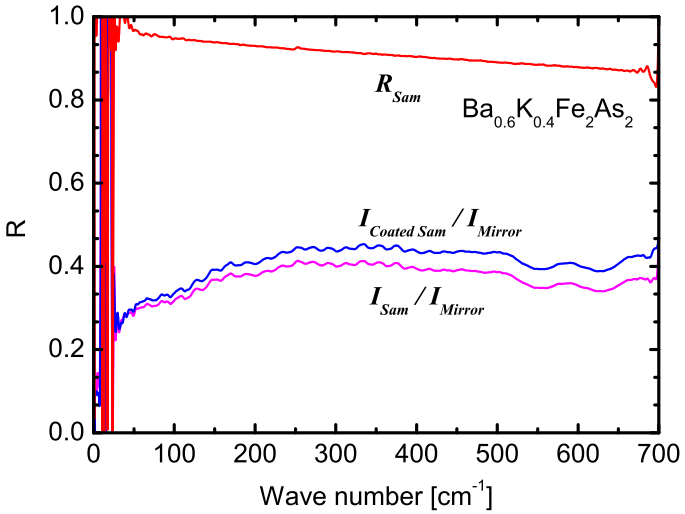

Figure 5.13: Reflectivity in the far infrared range measured with the *in situ* gold overfilling technique for optimally doped $Ba_{0.6}K_{0.4}Fe_2As_2$ single crystal at room temperature.

Figure 5.13 shows the frequency dependent reflectivity in the far infrared range determined by the *in situ* gold overfilling technique for an optimally doped

$Ba_{0.6}K_{0.4}Fe_2As_2$ single crystal at room temperature. Note that all the fine structure in the spectra of $I_{CoatedSam}/I_{Mirror}$ and I_{Sam}/I_{Mirror} has been eliminated. When measuring the reflectivity in frequency range above 10000 cm^{-1}, we coat the sample surface by aluminum instead of gold, as the reflectivity of gold starts to decrease above 10000 cm^{-1} and dives at about 19000 cm^{-1} representing the plasma edge, as shown in Fig. 3.5. Additionally, in order to achieve a high quality gold or aluminum layer on the surface of the sample, a good vacuum is need. An indication of a poor vacuum is the continuous increase of the strength of the 3200 cm^{-1} line from ice and the suppression of the reflectivity above this frequency with time below $\sim$ 150 K.

5.5 Optical cryostat

The LT-3-110 model optical cryostat designed by Advanced Research Systems, Inc. (USA) is exploited for the acquisition of temperature dependent reflectivity with the *in situ* gold overfilling technique. Figure 5.14 shows a panoramic view of the LT-3-110 optical cryostat, the radiation shield and the cold tail of the cryostat. The cryostat sits on a rotation stage with the cold tail extending into the vacuum shroud. There are double O-rings between the cryostat and the vacuum shroud. So the cryostat can be easily rotated without breaking the vacuum. A high vacuum (7×10^{-5} Pa) can be achieved by a turbo pump connected to the vacuum port at the bottom of the vacuum shroud. Inside the vacuum shroud, the sample and a stainless steel mirror are mounted on the cold tail of the cryostat which is covered by the radiation shield to prevent the cold tail against external radiation. The position of the sample and the stainless steel mirror can be adjusted and recorded by the two adjustment screws near the rotation stage. The sample in the cryostat can be cooled down to 4.2 K via a continuous flow of liquid helium. Two temperature sensors are fixed on the cryostat to read the temperature of the system. One is installed near the top of the cold tail as shown in Fig. 5.14 (the lower right panel). This sensor is used to detect the temperature of the cold tail, and also used as the input of temperature controlling system, so it's called the temperature control sensor. The other sits at the bottom of the cold tail close to the sample, and hence it records the temperature of the sample.

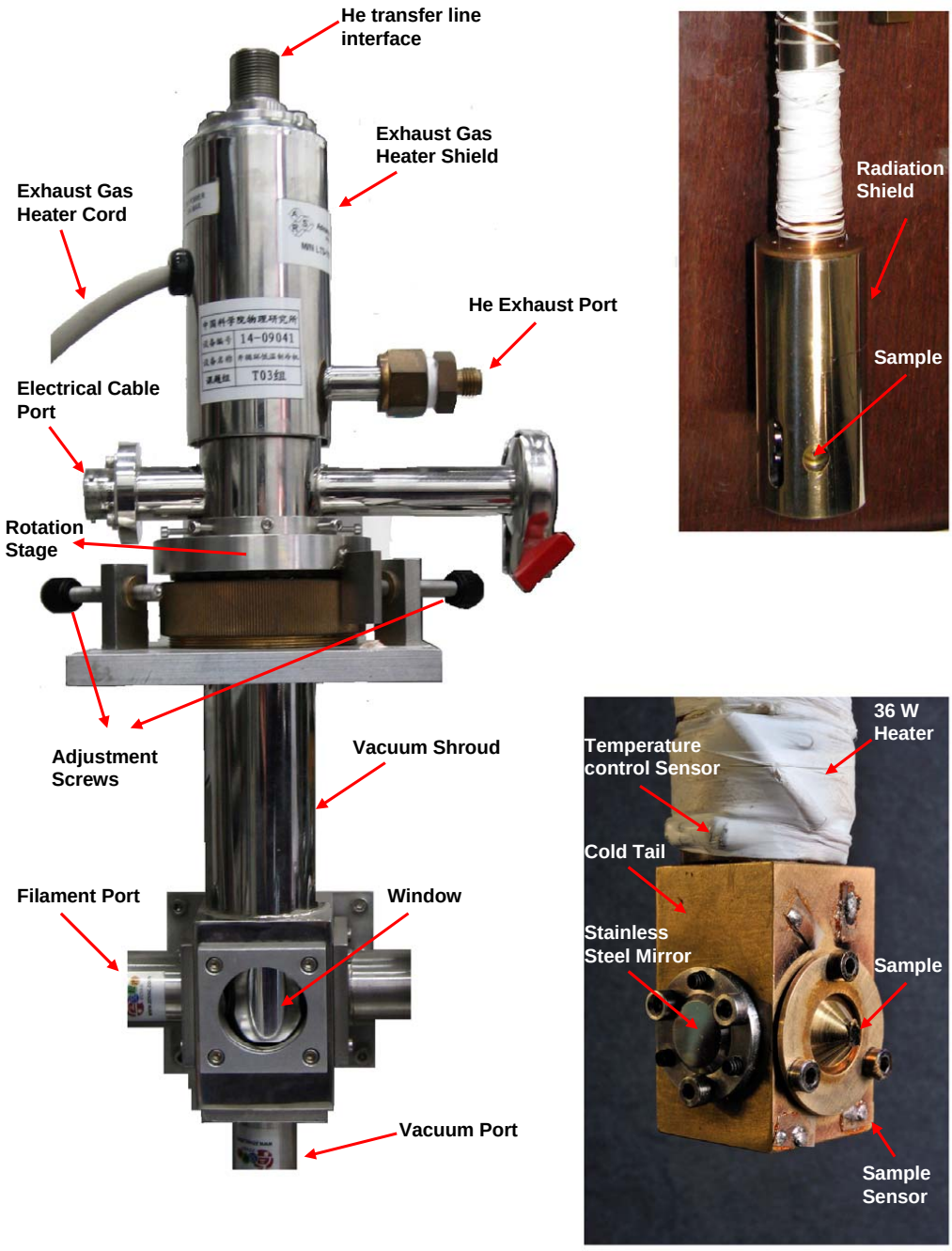

Figure 5.14: LT-3-110 model optical cryostat.

A combination of liquid helium flow control and power control of a 36 W heater near the cold tail allows precise temperature control of the sample.

5.6 Sample preparation and measurement

The high quality $Ba_{1-x}K_xFe_2As_2$ single crystals used in our experiment were grown by self-flux method using FeAs as the flux in the Institute of Physics, Chinese Academy of Sciences[106, 131]. The doping levels of our single crystals are x = 0.4 (optimally doped), x = 0.2 (underdoped), and x = 0.12 (underdoped) respectively. Our $Ba(Fe_{1-x}Co_x)_2As_2$ x = 0.08 (optimally doped) sample was grown by the same method in IRAMIS, SPEC, CEA [117]. Each sample is characterized by a large and shining surface which is supremely excellent for optical measurements.

The sample is mounted at the top of a copper cone by General Electric (GE) varnish, as shown in Fig. 5.15, and the cone is mechanically fixed to the cold tail of the cryostat by screws with a copper washer. Before gluing the sample, one

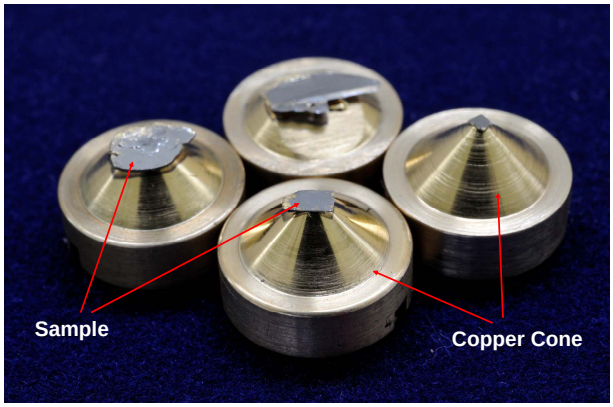

Figure 5.15: Samples with different size mounted on copper cones. Note that the size of the flat top of the cone should be approximately equal to the size of the sample.

needs to polish the copper cone. The size of the flat top of the copper cone should be approximately equal to the size of the sample. If the size of the cone top is larger than the sample, the sample can not cover the cone top completely, and the spectra will be contaminated by the light reflected by the copper. In

addition, too small cone top leads to poor thermal contact, so the sample can not be effectively cooled down in experiment. After mounting the sample on the copper cone by GE varnish, one should leave it in a dry environment for several hours, to make sure that the glue is completely dry, and then it's ready for experiment.

For each sample, the near normal incidence reflectivity from 20 cm^{-1} to 14000 cm^{-1} was measured on Bruker IFS 66v/s and IFS 113v spectrometers at 18 or 19 different temperatures from 5 K to 300 K. The *in situ* gold overfilling technique was used to obtain the absolute reflectivity of the samples, and the sample was cleaved prior each temperature run. The visible and UV range (10000 cm^{-1} to 55000 cm^{-1}) data at room temperature was collected with our AvaSpec-2048 $\times$ 14 model fiber optic spectrometer.

Chapter 6

Optical properties of K and Co doped Ba122 iron-based superconductors

In this chapter, we investigate the optical properties of K and Co doped Ba122 iron-based superconductors. First, we present our experimental results and data analysis for the optimally doped $Ba_{1-x}K_xFe_2As_2$ and $Ba(Fe_{1-x}Co_x)_2As_2$ samples, representing the hole and electron doped Ba122 systems respectively. Then a comparison between the optical properties of these two samples is presented. And finally, we discuss the optical properties of underdoped $Ba_{1-x}K_xFe_2As_2$ samples.

6.1 Optimally doped $Ba_{1-x}K_xFe_2As_2$

6.1.1 Reflectivity

The resistivity of the crystal exhibits a very sharp superconducting transition with an onset at $T_c = 39.1$ K and a width $\Delta T_c \sim 0.5$ K, as shown in the lower inset of Fig. 6.1. The main panel of Fig. 6.1 displays the in-plane reflectivity of $Ba_{0.6}K_{0.4}Fe_2As_2$ above and below the superconducting transition temperature. The top inset shows the reflectivity at room temperature up to 55000 cm^{-1}. The high reflectivity at low frequencies indicates a metallic response in this material. With the temperature decrease, the reflectivity increases, which is also expected by a metallic material. Upon entering the superconducting state, the low frequency reflectivity turns up quickly, and reaches a flat unity response below $\sim$ 160 cm^{-1} when the temperature is well below T_c. This is a clear signature of a fully open superconducting gap [67, 68].

It is often a complicated task to show that the absolute reflectivity is actually unity. In our set-up, we can claim that the accuracy we have in the absolute value of $R(\omega)$ is about 0.5%. This number is obtained by looking at the fluctuations

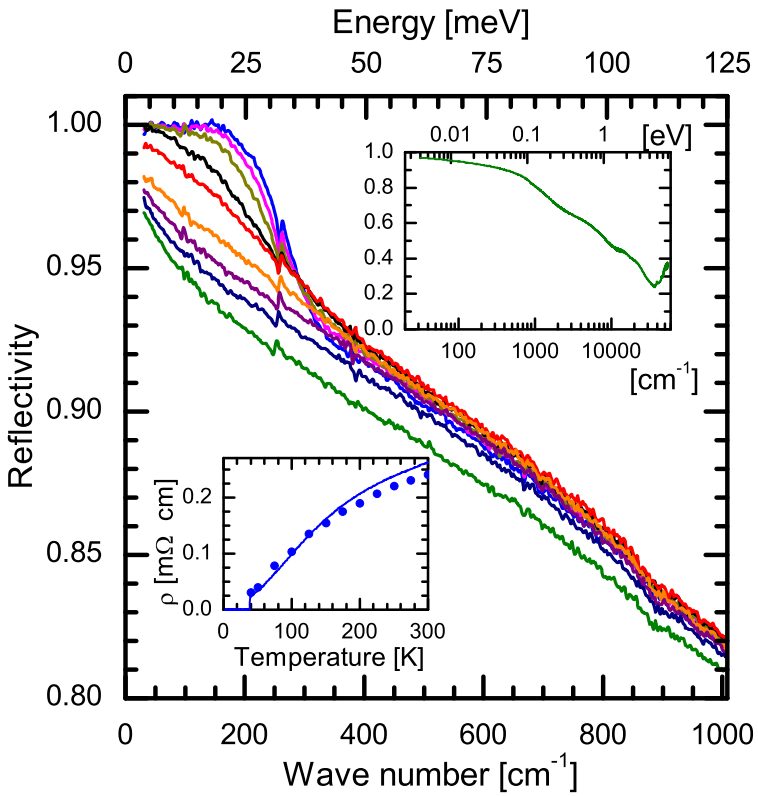

Figure 6.1: Infrared reflectivity of $Ba_{0.6}K_{0.4}Fe_2As_2$ single crystal measured (from top to bottom) at 5, 25, 30, 35, 40, 100, 150, 200, and 300 K. The top inset shows the reflectivity at 300 K up to 55000 cm^{-1}. The solid line in the lower inset is the DC resistivity and the solid circles are values from the zero frequency extrapolation of the optical conductivity.

in multiple measurements and by comparing the *in situ* evaporation results with reference free methods such as V-W, V-N and ellipsometry. Once we get closer to 100% reflectivity the errors in $\sigma_1(\omega)$ get larger. In $Ba_{0.6}K_{0.4}Fe_2As_2$, a 100% reflectivity leads to a fully gapped $\sigma_1(\omega)$ while a 99.5% reflectivity in this system leads to a low energy residual conductivity in the 1000 $\Omega^{-1}cm^{-1}$ range. Hence, it is only fair to ask whether we really have a fully gapped system. Is the accuracy in the absolute reflectivity a deal-breaker to determine a fully open superconducting gap?

Figure 6.2 helps us to solve this problem. A reflectivity of 100% is not the

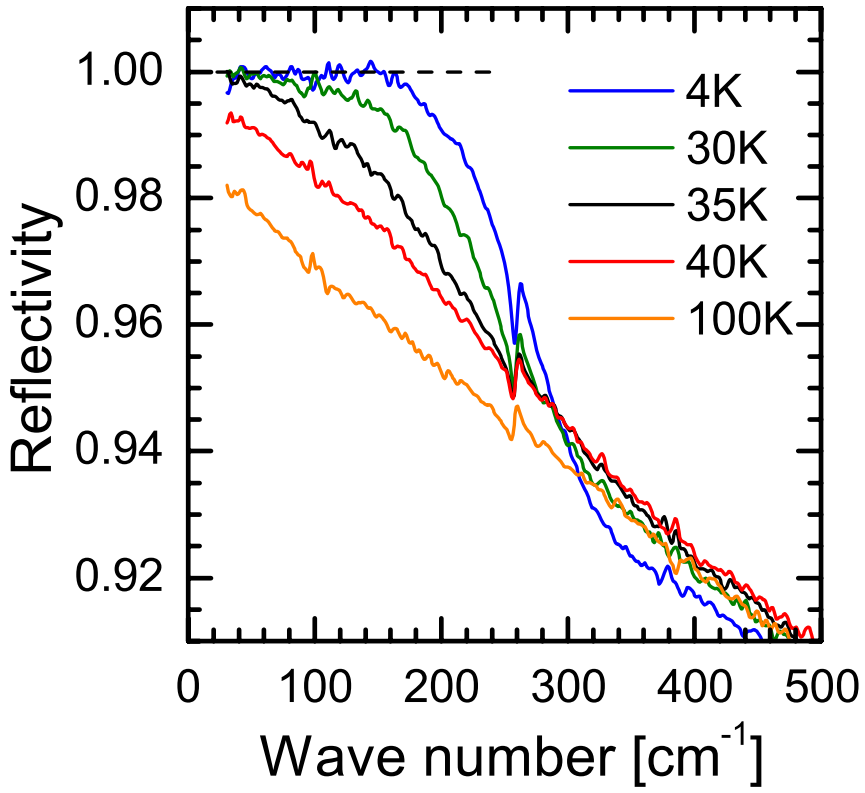

Figure 6.2: The enlarged view of the infrared reflectivity of $Ba_{0.6}K_{0.4}Fe_2As_2$ in the superconducting and normal states. The dashed line is a horizontal line at 100% reflectivity.

only clue on the data about a full gap. The energy dispersion of the data also gives us a strong indication that the gap is fully open. Our $Ba_{0.6}K_{0.4}Fe_2As_2$ sample, at 4 K, has a constant reflectivity below $\sim$ 160 cm^{-1}. This can be clearly seen by comparing the data with the flat 100% line shown in Fig. 6.2. If the system is not fully gapped, one would have to consider the presence of unpaired quasiparticles that leads to a non vanishing curvature in the reflectivity. The curvature is positive for normal Drude-like carries and negative for a gap with residual quasiparticles. At 4 K, our sample has a flat, constant reflectivity below 160 cm^{-1}. For comparison, one can look at the 30 and 35 K data, where although the reflectivity seems to reach 100% at low frequencies, a clear frequency

dispersion is present. Of course, at these two temperatures thermally broken pairs lead to a low frequency absorption.

If we calculate the slope and the curvature of the low frequency reflectivity, both are more than an order of magnitude smaller at 4 K than at 30 or 35 K. The reflectivity at 4 K, below 160 cm^{-1}, is flat with an accuracy better than 0.05%. This is not compatible with unpaired quasiparticles and the only physically meaningful interpretation for the data is a fully gapped system.

In order to have a fine temperature dependence of the gaps and penetration depth for $Ba_{0.6}K_{0.4}Fe_2As_2$, we performed a relative thermal reflectivity (RTR) measurement, in addition to the absolute reflectivity measurements. In this technique, we determine the reflectivity of the material over a relatively narrow temperature range without any physical motion of the sample. The data at each temperature is divided by the measurement at one specific arbitrary temperature T_0. Next, each temperature is multiplied by the absolute reflectivity measured at T_0 using the *in situ* gold overfilling technique. The relative thermal reflectivity is very useful in determining small changes of the spectrum through a phase transition, specially when sharp features, such as the reflectivity edge, emerge from a reasonably featureless background.

In the case of $Ba_{0.6}K_{0.4}Fe_2As_2$ we measured the relative thermal reflectivity from 5 to 45 K, every Kelvin, in the 50-700 cm^{-1} spectral range. All spectra were normalized by the measurement at $T_0 = 40$ K, which is above T_c, then we used the absolute reflectivity at 40 K to correct the data taken at all other temperatures. These measurements have a very high relative accuracy and allow for a fine determination of the spectral temperature evolution. Figure 6.3 shows, as thin red lines, the reflectivity obtained from the RTR method at 16 selected temperatures. For comparison, the more accurate absolute measurements are shown at 4, 35, and 50 K as thick blue lines.

6.1.2 Optical conductivity

The real part $[\sigma_1(\omega)]$ of the optical conductivity was derived from the reflectivity through Kramers-Kronig analysis. At low frequencies we used a Hagen-

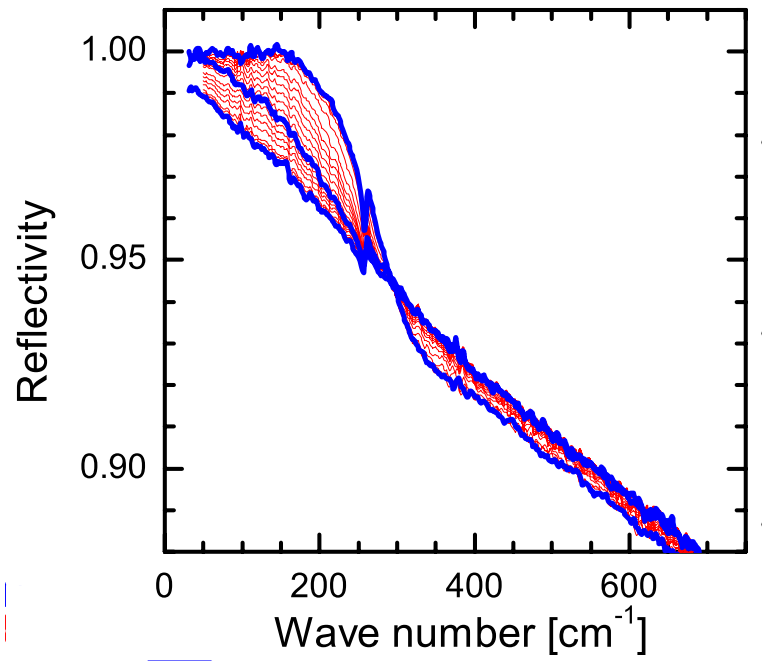

Figure 6.3: The reflectivity obtained from the RTR method at 16 selected temperatures (red thin lines). The more accurate absolute measurements are shown at 4, 35, and 50 K as thick blue lines.

Rubens $(1 - A\sqrt{\omega})$ extrapolation for the normal state and a superconducting $(1 - A\omega^4)$ extrapolation below T_c. At high frequencies we used a constant reflectivity to 40 eV followed by a ω^{-4} free electron termination. Figure 6.4 shows $\sigma_1(\omega)$ up to 10000 cm^{-1} at selected temperatures. The inset shows the enlarged view of $\sigma_1(\omega)$ at low frequencies.

In the normal state, the low frequency optical response is dominated by a metallic behavior which is described by a Drude-like absorption band centered at zero frequency. As the temperature decreases, the spectral weight at low frequencies increases as a result of the narrowing of the Drude-like absorption band. Meanwhile, a large part of the spectral weight below $\sim$ 5000 cm^{-1} is transferred to very high energy scale ($\sim$ 5000 – 12000 cm^{-1}), and this spectral weight redistribution continues down to the superconducting transition temperature. Below T_c, a dramatic suppression of $\sigma_1(\omega)$ sets in. At 5 K, $\sigma_1(\omega)$ vanishes, within error

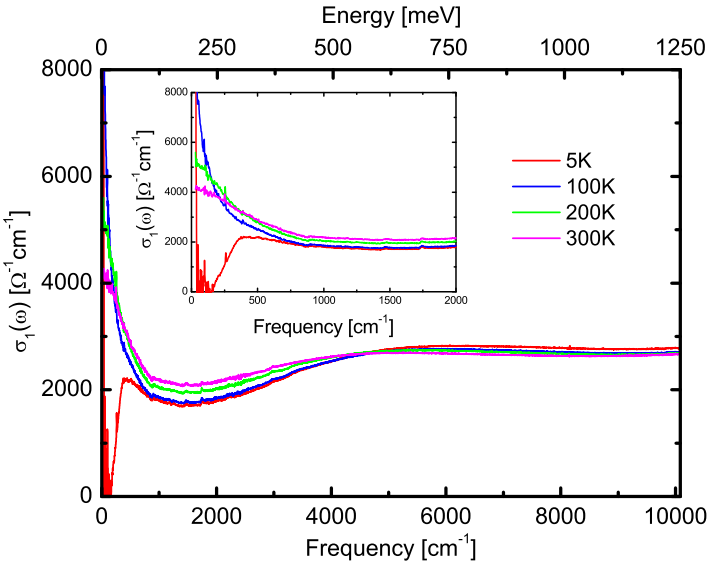

Figure 6.4: In-plane optical conductivity of $Ba_{0.6}K_{0.4}Fe_2As_2$ up to 10000 cm^{-1} at selected temperatures. The inset shows the enlarged view of the optical conductivity at low frequencies.

bars, below about 160 cm^{-1} indicating a fully open gap in $Ba_{0.6}K_{0.4}Fe_2As_2$.

We also converted the reflectivity, measured by the RTR method, to optical conductivity through Kramers-Kronig analysis. Above 700 cm^{-1} we utilized an interpolation of the absolute reflectivity, taken every 5 K. Below 50 cm^{-1} we used either a Hagen-Rubens or a superconducting extrapolation. Figure 6.5 shows the real part of the optical conductivity derived from the relative temperature reflectivity measurements (thin red lines). The thick lines are the data obtained from the absolute reflectivity measurements.

6.1.3 Data analysis

The normal state optical conductivity showing metallic response can be described by a Drude-Lorentz model:

$$\sigma_1(\omega) = \frac{2\pi}{Z_0} \sum_k \left[\frac{\Omega_{p,k}^2}{\tau_k(\omega^2 + \tau_k^{-2})} + \frac{\gamma_k \omega^2 S_k^2}{(\Omega_k^2 - \omega^2)^2 + \gamma_k^2 \omega^2} \right], \tag{6.1}$$

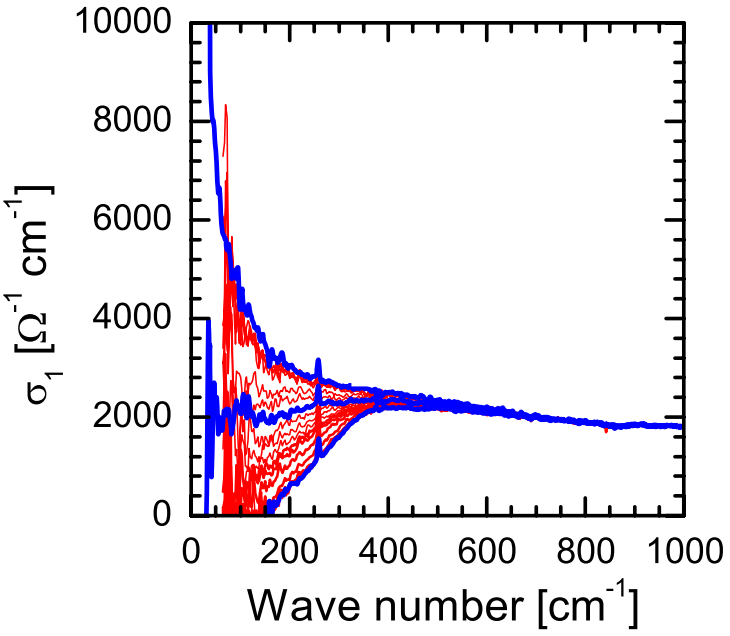

Figure 6.5: In-plane optical conductivity of $Ba_{0.6}K_{0.4}Fe_2As_2$ obtained from the RTR method at 16 selected temperatures (thin red lines). For comparison, the thick lines are the data obtained from the absolute reflectivity measurements.

where Z_0 is the vacuum impedance. The first term in Eq. 6.1 corresponds to a sum of free-carrier Drude responses and the second term is a sum of Lorentz oscillators which have been discussed in detail in Chapter 3. As shown in Fig. 6.6, the optical conductivity at 150 K is decomposed into a broad Drude, a narrow Drude and a Lorentz terms. In addition, we also use one Lorentz oscillator to represent the phonon at about 260 cm^{-1}, not shown here. These four components suffice to describe the optical conductivity up to 10000 cm^{-1} at all the measured temperatures in the normal state. The zero frequency values of our fits represent the inverse dc resistivity of the material which we compare (solid circles in the lower inset of Fig. 6.1) to the measured dc resistivity (solid line). The very good agreement indicates that our parametrization of the data is representative of the physics of the system.

Band structure theory predicts up to 5 bands at the Fermi Level [22, 23].

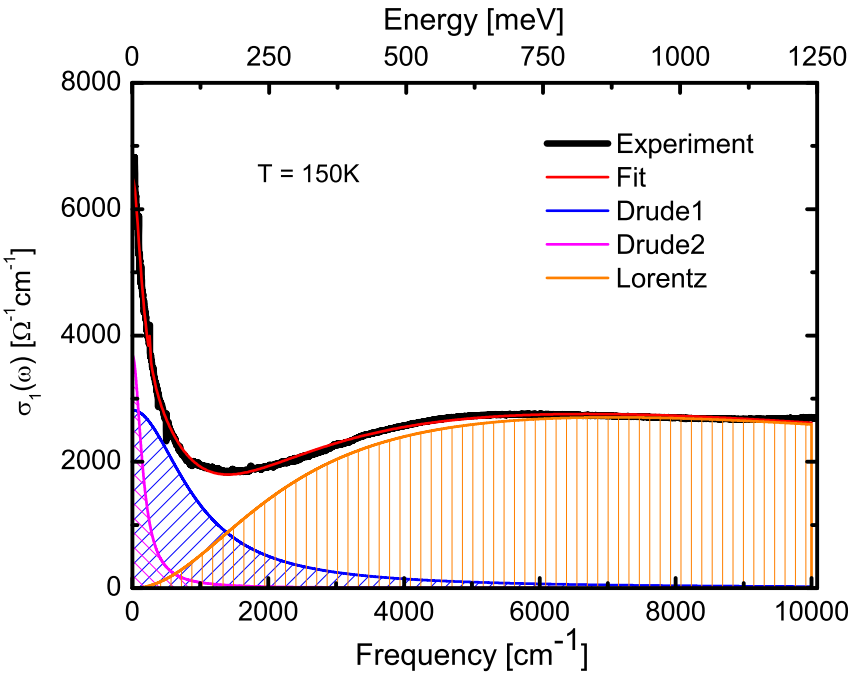

Figure 6.6: The thick black solid line is the optical conductivity of $Ba_{0.6}K_{0.4}Fe_2As_2$ at 150 K, the red solid line through the data is the fit which is decomposed into a broad Drude (blue solid line), a narrow Drude (pink solid line) and a Lorentz (orange solid line) terms.

Here we use two Drude terms to describe the normal state low frequency optical conductivity of our sample, which is compatible with previous works on similar samples [85, 89]. From the infrared spectroscopy point of view, in a multi-band system, if the scattering rates in different bands have the same value, $1/\tau_0$ for instance, we can not distinguish these bands by optical conductivity, because the optical conductivity of this multi-band system can be described by only one Drude with the scattering rate equal to $1/\tau_0$, and Ω_p^2 equal to the sum of all bands. When the scattering rate varies in different bands, optical spectroscopy can distinguish them, because the optical response of the system can not be reproduced by only one Drude band. Thus, the two Drude terms description of the low frequency optical conductivity indicates that: (i) Iron-based superconductors fall into the multi-band system category, and the two Drude terms used here are

associated with different Fermi surface sheets; (ii) Two groups of scattering rates dominate these Fermi surfaces. The presence of multiple bands at the Fermi Level in iron-based superconductors was also confirmed by ARPES [118, 120] and the variation of the scattering rate in different bands was supported by both theory calculation [132] and experiments [114, 115, 133].

The evolution of the two electronic subsystems, represented by the two Drude terms, with temperature provides plenty of interesting information. Figure 6.7 shows the temperature dependence of all the parameters derived from the fit. Panel (a) depicts the plasma frequencies of the two Drude terms as a function of temperature. Upon cooling down, the plasma frequency is roughly a constant for each of the two components. This indicates that there is no electron transfer between these two subsystems, and the multiband structure doesn't change with temperature which is consistent with a previous work [85]. Panel (b) portrays the temperature dependence of the scattering rate of the two electronic subsystems. The scattering rate in the narrow Drude band decreases almost linearly with the temperature decrease while the broad one doesn't show obvious temperature dependence. Panel (c) displays the contribution of the two electronic subsystems to the DC conductivity. From which we can see that both subsystems have contribution to the DC conductivity, but the contribution from the broad Drude does not change with temperature. Hence the temperature dependence of the total DC conductivity arises out of the narrow Drude band.

Note that the resistivity curve of $Ba_{0.6}K_{0.4}Fe_2As_2$ exhibits a change of slope at about 175 K. This can be explained by the different temperature dependence of the two Drude bands. The two curves in Panel (c) cross over at about 175 K. Above this temperature, the DC conductivity contribution from the narrow Drude band (red squares) is smaller than from the broad one (blue squares), so the total DC conductivity is dominated by the broad Drude band which does not show obvious temperature dependence. As a result, above 175 K, the DC resistivity decreases slowly upon cooling down. Below 175 K, the DC conductivity contribution from the narrow Drude band exceeds the broad one, and the total DC conductivity is dominated by the narrow Drude band which exhibits distinct temperature dependence. Hence, below 175 K, the decrease of the DC resistivity

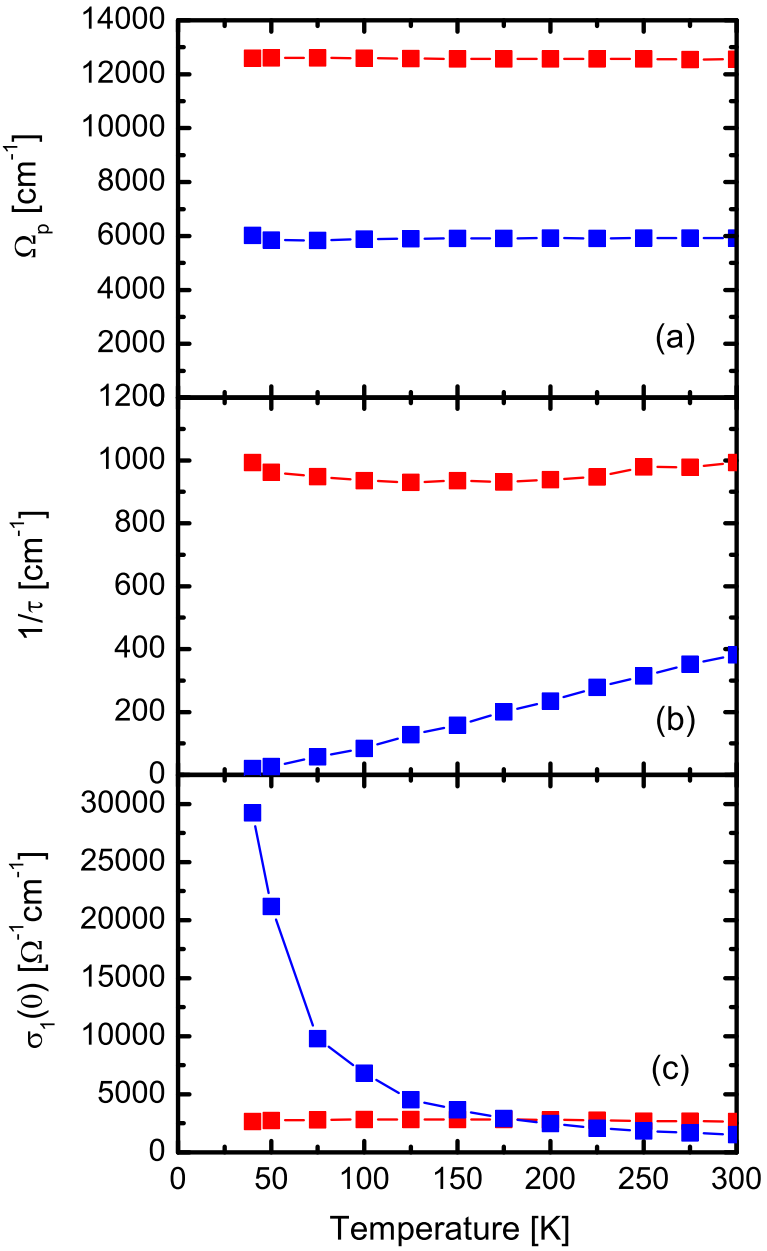

Figure 6.7: Panel (a) shows the plasma frequency of the two Drude terms as a function of temperature. Panel (b) shows the temperature dependence of the scattering rate of the two Drude terms. Panel (c) displays the contribution of the two Drude terms to the DC conductivity at different temperatures.

speeds up with temperature decrease resulting in the change of slope in $R-T$ curve at about 175 K. Similar conclusions are reached by Hall effect investigation [116].

In order to quantitatively describe the optical response below T_c, we replace the two Drude terms used for the normal state in Eq. 6.1 by two corresponding Mattis-Bardeen conductivities, modified to take into account arbitrary scattering [66]. The thick black solid line in Fig. 6.8 is the measured optical conductivity

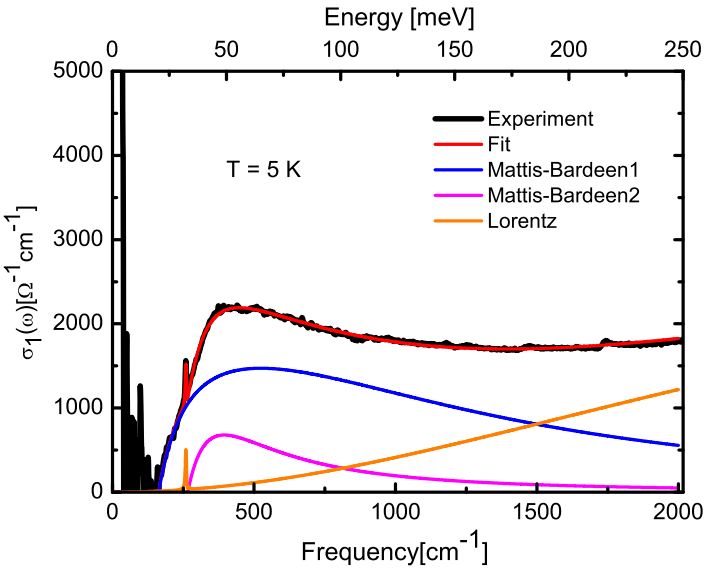

Figure 6.8: The thick black solid line is the optical conductivity of $Ba_{0.6}K_{0.4}Fe_2As_2$ at 5 K, the red solid line through the data is the fit which is the superposition of two Mattis-Bardeen terms describing the superconducting state optical conductivity and two Lorentz oscillators accounting for the phonon at about 260 cm^{-1} and the mid-infrared interband transitions.

of $Ba_{0.6}K_{0.4}Fe_2As_2$ at 5 K, and the red solid line through the data is the fit which consists of four contributions: two superconducting bands, one phonon and the mid-infrared interband transition. We found that the low frequency optical response of $Ba_{0.6}K_{0.4}Fe_2As_2$ in the superconducting state can be reproduced very well by two Mattis-Bardeen terms. These two terms have absorption edges at $E_S^0 = 20$ meV and $E_L^0 = 33$ meV. In the Mattis-Bardeen theory, the absorption

edge occurs at $E = 2\Delta$. However, Mattis-Bardeen assumes a weakly coupled superconductor and some impurity scattering. In the case of the strongly coupled pnictides, the onset of absorption in $\sigma_1(\omega)$ happens at $E = E_B + 2\Delta$, where E_B is the energy of the pairing mechanism exchange boson [134]. Nevertheless, Mattis-Bardeen is still a very good approximation for the electrodynamics of the system, as far as one takes into account the energy of the gluing boson to extract the gap value from the absorption edge. A good candidate for the pairing glue response is a magnetic resonance in $Ba_{0.6}K_{0.4}Fe_2As_2$ found by Neutron scattering at about 14 meV [127] (discussed in Sec. 4.2.7, see Fig. 4.14). If we use this value as E_B, we find zero temperature gaps at $\Delta_S^0 = 3$ meV and $\Delta_L^0 = 9.5$ meV, values well within the reported range for this material [94, 118, 122, 125, 135–137].

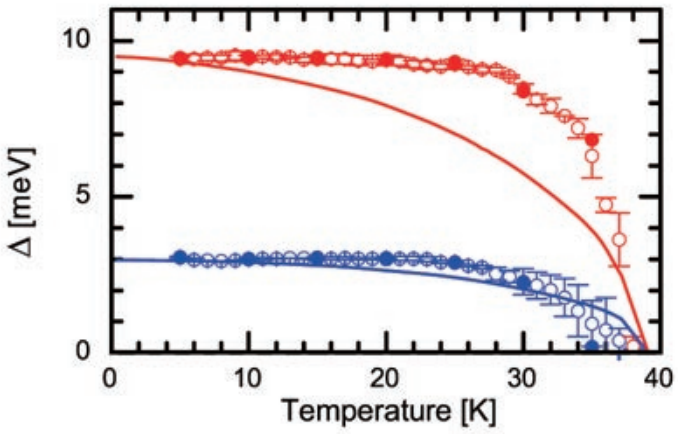

Figure 6.9: Superconducting gap values obtained by fitting $\sigma_1(\omega)$. Open symbols are derived from the fine reflectivity temperature resolution measurements and solid symbols from the accurate absolute reflectivity. The solid lines are calculations for a two band superconductor with a large interband interaction term.

Figure 6.9 shows the temperature dependence of the gaps obtained from fits to $\sigma_1(\omega)$. Suhl et al. proposed an extension of the weak coupling BCS theory for multiple bands [16]. This theory takes into account a pairing interaction for each band (V_{11} and V_{22}) as well as an interband (V_{12}) pairing term. When $V_{12} \ll \sqrt{V_{11}V_{22}}$, a two band material behaves almost as two independent sin-

gle band superconductors. In this case, the smaller gap closes at a temperature smaller that the macroscopic T_c for the material. Conversely, when only V_{12} is not null, one finds the situation shown as the solid lines in Fig. 6.9, which qualitatively agrees with our data: both gaps have a similar temperature dependence and close at the same T_c. The experimentally determined gap opening faster than calculations is in accordance with pnictides falling into strongly coupled superconductor category [138]. Nevertheless, the qualitative agreement indicates a strong interband pairing interaction (V_{12}) in pnictides.

6.1.4 Spectral weight analysis

The spectral weight is defined as the area under the optical conductivity spectrum, written as

$$SW = \int_{0^+}^{\omega_c} \sigma_1(\omega) d\omega, \tag{6.2}$$

where ω_c is a cut-off frequency. As we discussed in Chapter 3, when the cut-off frequency is replaced by infinite, the spectral weight depends only on the total number of electrons and the bare electron mass. Therefore, implied by charge conservation, this spectral weight should be conserved. Indeed, the optical conductivity is a linear response function which means that the total optical conductivity is a simple sum of conductivities responsible for different excitations. The spectral weight can be separately conserved for each kind of excitation if the integral covers the spectrum responsible for the specific excitation. Figure 6.10 shows the spectral weight as a function of temperature at different cut-off frequencies.

First we discuss the result in the normal state. Figure 6.10 (a) shows the temperature dependence of the spectral weight at $\omega_c = 400$ cm^{-1}. As the temperature decreases, the spectral weight below 400 cm^{-1} increases all the way down to T_c. This is due to the narrowing of the Drude absorption band. The almost T linear behavior of the spectral weight indicates strong correlations among the carriers [139, 140]. At a cut-off frequency $\omega_c = 1000$ cm^{-1} as shown in Fig. 6.10 (b), the spectral weight is temporarily conserved. This is in accord with our previous analysis. The cut-off frequency $\omega_c = 1000$ cm^{-1} covers almost all the

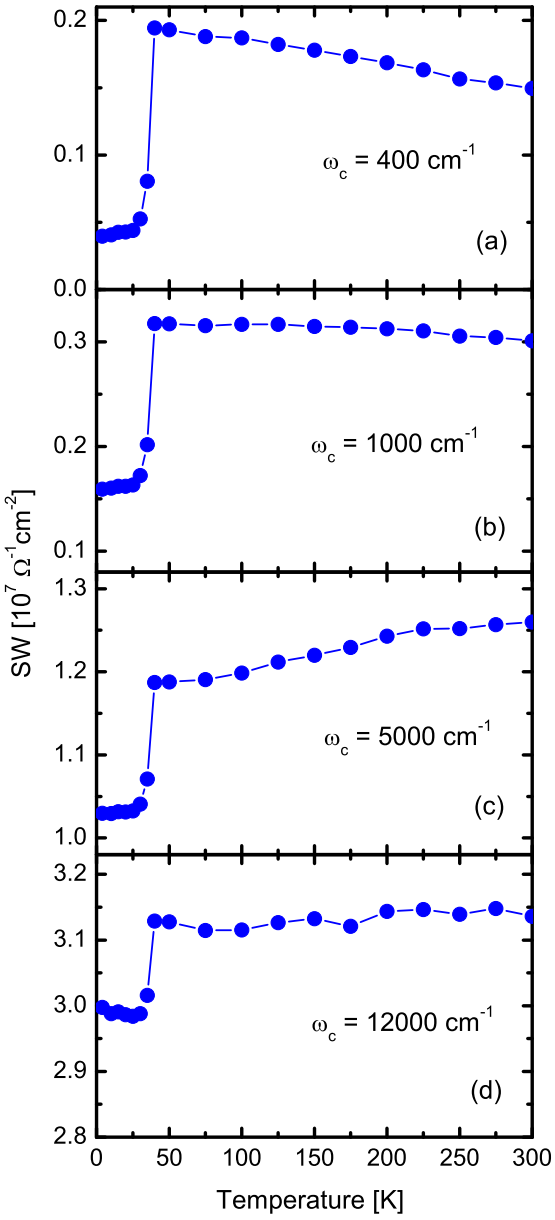

Figure 6.10: Spectral weight as a function of temperature at different cut-off frequencies: (a) $\omega_c = 400$ cm^{-1}; (b) $\omega_c = 1000$ cm^{-1}; (c) $\omega_c = 5000$ cm^{-1}; (d) $\omega_c = 12000$ cm^{-1}.

spectral weight of the narrow Drude term although not high enough to cover the broad one, which can be seen from Fig. 6.6. The temperature dependence of the low frequency conductivity comes from the contribution of the narrow Drude band, and the broad Drude band is not affected by the temperature leading to a temporary conservation of the spectral weight. When integrating to a higher cut-off frequency, for instance $\omega_c = 5000$ cm^{-1}, an interesting phenomenon happens. As displayed in Fig. 6.10 (c), the spectral weight below 5000 cm^{-1} decreases upon cooling down. This phenomenon indicates that a large part of spectral weight below 5000 cm^{-1} is transferred to a higher energy scale. A crossover of the optical conductivity at $\sim$ 5000 cm^{-1} can be see from the main panel of Fig. 6.4. Figure 6.10 (d) shows that the spectral weight is recovered when $\omega_c = 12000$ cm^{-1} is taken as the upper limit of the integration in Eq. 6.2. In summary, the spectral weight analysis in the normal state implies that a free carrier metallic response at low frequencies coexists with a striking spectral weight transfer from below $\sim$ 5000 cm^{-1} to very high, broad energy scale ($\sim$ 5000 – 12000 cm^{-1}). This is not expected for a normal metal. In this case, the normal state of the iron-pnictide superconductors probably needs to be re-understood.

Next we concentrate on the superconducting state. In all the four panels of Fig. 6.10, a striking suppression of the spectral weight appears at T_c. From the optical conductivity (Fig. 6.4) we can also see that a large part of the low frequency optical spectral weight disappeared with the opening of the superconducting gaps. This is due to the superconducting condensate. The spectral weight lost from finite frequency in the superconducting state is compensated by the weight of the $\delta(\omega)$ function at zero frequency representing the infinite DC conductivity. This is often referred to as the Ferrell-Glover-Tinkham (FGT) sum rule [15, 141]. As we described in Eq. 6.2, when the cut-off frequency covers the excitation spectrum responsible for the superconducting condensate, the FGT sum rule is fulfilled. In the conventional superconductors, this happens at an energy corresponding roughly to 4Δ. However, in the underdoped high-T_c cuprates, the recovery of the FGT sum rule goes to very high energy ($\sim$ 1 – 2 eV), or the sum rule is even violated [139, 142–145]. What should we expect for the iron-pnictide superconductors?

To confirm the FGT sum rule, we need to determine the superfluid weight which is related to a London plasma frequency. It can be calculated utilizing the imaginary part $[\sigma_2(\omega)]$ of the optical conductivity [70, 146]. In the superconducting state, the real part of the optical conductivity has the contribution of two separate parts: a delta function at zero frequency representing the superconducting condensate and a regular non-superconducting part $\sigma_1'(\omega)$. Thus $\sigma_1(\omega)$ is written as

$$\sigma_1(\omega) = \frac{\pi^2}{Z_0}\Omega_L^2\delta(\omega) + \sigma_1'(\omega), \tag{6.3}$$

where Ω_L is the London plasma frequency, namely the superconducting plasma frequency. Kramers-Kronig of $\sigma_1(\omega)$ in Eq. 6.3 yields the imaginary part $[\sigma_2(\omega)]$ of the optical conductivity, written as

$$\sigma_2(\omega) = \frac{2\pi}{Z_0\omega}\Omega_L^2 - \frac{2\omega}{\pi}\int_0^\infty \frac{\sigma_1'(\omega')}{\omega'^2 - \omega^2}d\omega', \tag{6.4}$$

$\sigma_1(\omega)$ and $\sigma_2(\omega)$ can be obtained directly from Kramers-Kronig of the reflectivity. Because $\sigma_1(\omega)$ is achieved only for finite frequencies, it has no information on the $\delta(\omega)$ function at zero frequency therefore equals $\sigma_1'(\omega)$. Consequently, the London plasma frequency Ω_L can be easily obtained by applying Eq. 6.4.

The FGT sum rule can be verified by comparing the London plasma frequency determined above and the contribution to the London plasma frequency from the spectral weight lost in the optical conductivity due to the superconducting condensate. This contribution at a specific temperature in the superconducting state up to ω is derived as follows:

$$\Omega^2(\omega) = \frac{Z_0}{\pi^2}\int_{0^+}^{\omega}[\sigma_1^n(\omega') - \sigma_1^s(\omega')]d\omega', \tag{6.5}$$

where $\sigma_1^n(\omega)$ is the optical conductivity spectrum in the normal state, and here we choose the one at 40 K; $\sigma_1^s(\omega)$ corresponds to the optical conductivity in the superconducting state. One can expect $\Omega(\omega \to \infty) = \Omega_L$.

The flat lines in Fig. 6.11 are Ω_L determined from Eq. 6.4. They are compared to the missing spectral weight contribution to Ω_L determined from Eq. 6.5. We can see that the FGT sum rule is satisfied at about 600 cm^{-1} corresponding roughly to $4.5\Delta_L$.

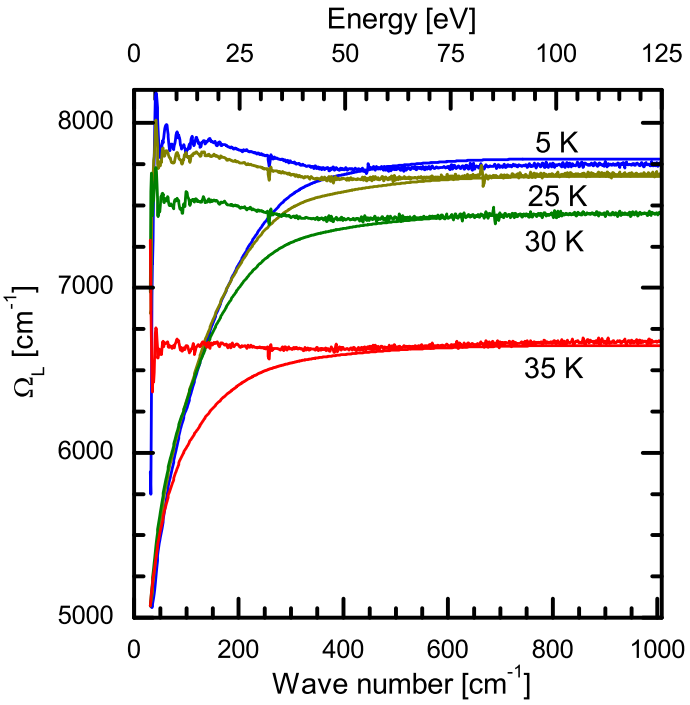

Figure 6.11: London plasma frequency of $Ba_{0.6}K_{0.4}Fe_2As_2$. The flat lines are determined from the ω^{-1} contribution to $\sigma_2(\omega)$ and they are compared to the low frequency spectral weight lost between $\sigma_1(\omega)$ at 40 K and low temperatures.

The penetration depth can be easily calculated from the London plasma frequency via $\lambda = 1/2\pi\Omega_L$. Figure 6.12 shows the penetration depth as a function of temperature for $Ba_{0.6}K_{0.4}Fe_2As_2$. The dashed line is obtained by utilizing the solution of the penetration depth BCS equation assuming a strong coupling temperature dependence for a gap $\Delta_0 = 9.5\text{meV} = \Delta_L^0$. In the inset we show the superfluid density and the same calculation as in the main panel. Within error bars the large gap Δ_L^0, having a smaller penetration depth, dominates the value of the total penetration depth. This is a signature that the superconducting bands respond in parallel as implied by summing two Mattis-Bardeen terms in $\sigma_1(\omega)$.

We can also study the FGT sum rule only within the conduction bands. Figure 6.6 decomposes the optical conductivity into three components: two Drude terms accounting for the free carrier response and a Lorentz term accounting for

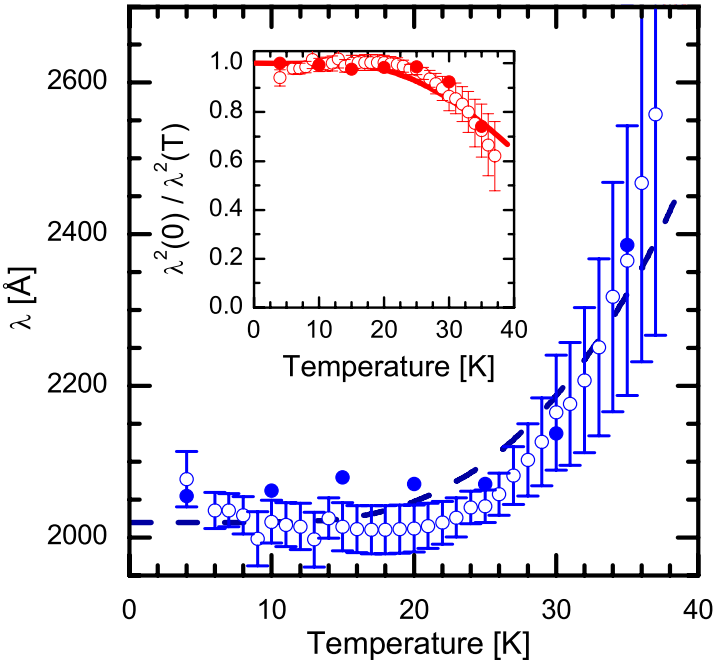

Figure 6.12: Penetration depth derived from the London plasma frequency. Solid symbols are obtained from the accurate absolute reflectivity and open symbols from the fine reflectivity temperature resolution measurements. The dashed line is a calculation with $\Delta_L^0 = 9.5$ meV. The inset shows the superfluid density and the same calculation as in the main panel.

interband transition, so the total spectral weight has the contribution from the free carriers and the interband transition, written as

$$SW_{total} = SW_{Drude} + SW_{Lorentz} \tag{6.6}$$

Therefore, we can get the spectral weight only from the free carriers by subtracting the Lorentz contribution from the total spectral weight. Figure 6.13 shows the spectral weight of the Drude terms as a function of temperature normalized by its value at 300 K (blue solid circles). A cut-off frequency of $\omega_c = 8000$ cm^{-1} is used for the spectral weight calculation. It is high enough to cover all the spectral weight of the two Drude terms which can be seen from Fig. 6.6. Above T_c, the spectral weight of the Drude terms doesn't change with the temperature de-

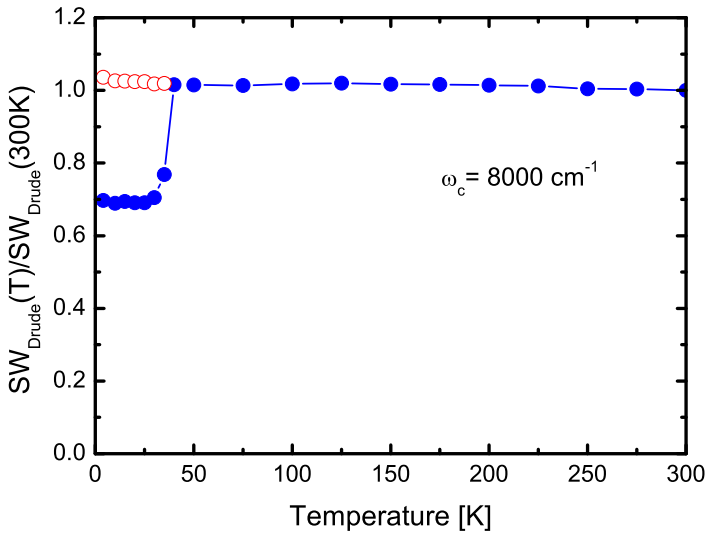

Figure 6.13: The blue solid circles are the spectral weight of the two Drude terms, representing the conduction bands, as a function of temperature at $\omega_c = 8000$ cm^{-1}. The open circles are obtained by adding the superfluid weight to the spectral weight in the superconducting state.

crease implying that the band structure and the area of the Fermi surface do not change upon cooling down. In the superconducting state, the spectral weight is suppressed by 30% indicating that about 30% of the conduction band electrons participate in the superconducting condensate. Further, $Ba_{0.6}K_{0.4}Fe_2As_2$ is in dirty limit. The red open circles in Fig. 6.13 are obtained by adding the superfluid weight to the spectral weight in the superconducting state. They follow the normal state very well demonstrating that the spectral weight lost from finite frequency due to the superconducting condensate is fully recovered by the $\delta(\omega)$ function at zero frequency, i.e. the FGT sum rule is fulfilled.

6.2 Optimally doped $Ba(Fe_{1-x}Co_x)_2As_2$

6.2.1 Reflectivity

Figure 6.14 shows the far-infrared absolute reflectivity at low temperatures, above and below T_c. Upon crossing the superconducting transition, the reflec-

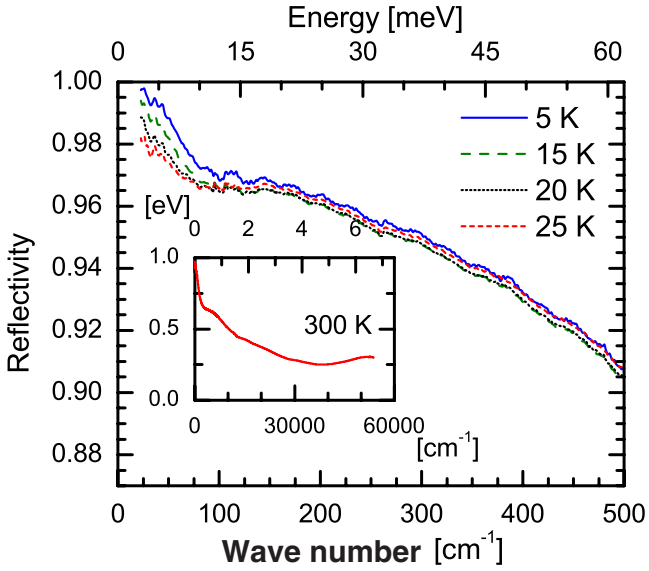

Figure 6.14: Reflectivity of $Ba(Fe_{0.92}Co_{0.08})_2As_2$ at low temperatures above and below $T_c = 22.5$ K. The inset shows the 300 K reflectivity in the full measured spectral range.

tivity increases below 100 cm^{-1}, but unlike the case in $Ba_{0.6}K_{0.4}Fe_2As_2$, the reflectivity of $Ba(Fe_{0.92}Co_{0.08})_2As_2$ does not reach a flat unity response expected for a fully s-wave-gapped superconductor. The inset of this figure shows the reflectivity at 300 K measured in the full spectral range.

6.2.2 Optical conductivity

The optical conductivity is derived from the measured reflectivity via Kramers-Kronig analysis. A Hagen-Rubens (normal state) or a two-fluid (superconducting state) is used for the low frequency extrapolation. At high frequencies, we use a constant reflectivity up to 200 000 cm^{-1} and terminate the data with an ω^{-4} free-electron response. Different choices of low- and high-frequency extrapolations do not change the optical conductivity more than 1% in the far-infrared range. Figure 6.15 shows the measured far-infrared reflectivity (symbols) at various temperatures and corresponding fits (solid lines). Upon entering the superconducting state, the opening of the superconducting gap, characterized by

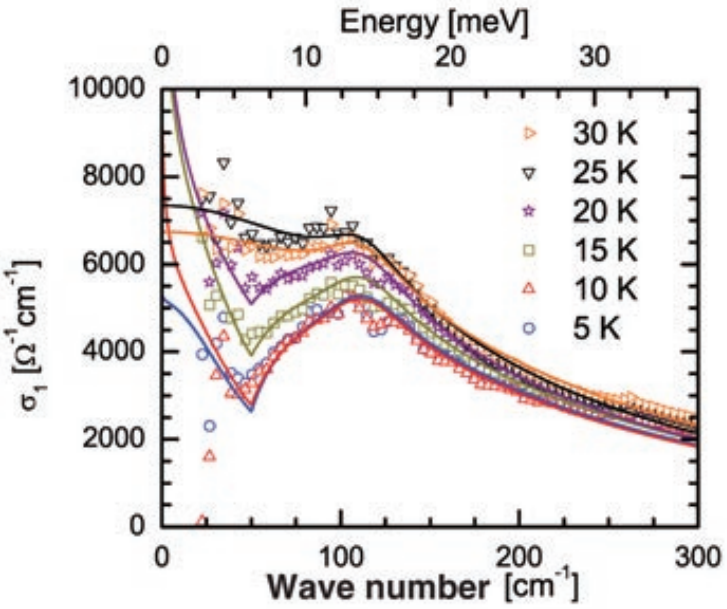

Figure 6.15: The symbols are measured optical conductivity at various temperature above and below T_c. The solid smooth lines are corresponding fits.

a suppression of the low energy optical conductivity, is clearly observed. But two notable differences in optical response between the Co and K doped samples can be seen: (i) The superconducting gap in the Co doped sample opens in an energy scale much lower than the K doped Ba122 sample; (ii) The low energy optical conductivity does not vanish in the superconducting state. Large residual conductivity exists in the Co doped Ba122 system [147, 148].

6.2.3 Data analysis

We fit the 30 K low frequency optical conductivity assuming a single Drude response and a Lorentz oscillator as shown in Fig. 6.16. The Drude term characterizes the free carriers. The origin of the Lorentz peak is not well established. It could be the response of localized carriers induced by disorder but as it has been seen in an independent $Ba(Fe_{1-x}Co_x)_2As_2$ measurement [81], it is likely an intrinsic excitation such as low-energy interband transitions. In any case, its spectral weight is small and the parameters used in this Lorentz peak at 30 K

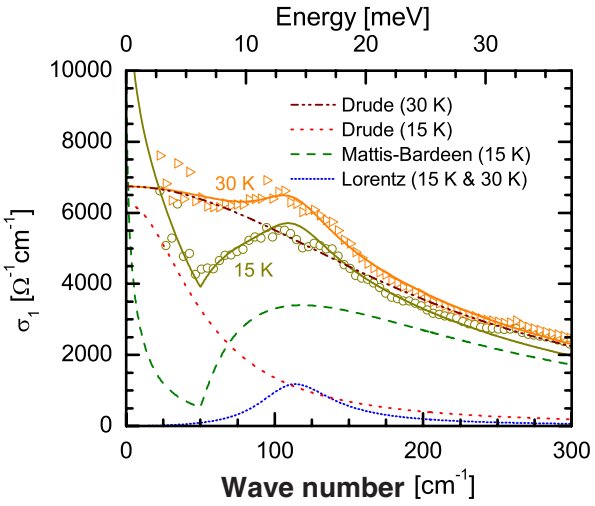

Figure 6.16: The open circles are the real part of the optical conductivity at 15 K and the open triangles at 30 K. The solid lines going through these points are fits to the data.

are kept fixed at all other temperatures.

In the superconducting state of a conventional BCS superconductor, one would replace the normal-state Drude term by a Mattis-Bardeen response alone, like we did for the $Ba_{0.6}K_{0.4}Fe_2As_2$ sample. However, to describe the data at 15 K, we must keep an independent Drude peak accounting for the low energy residual conductivity in the superconducting state. The fit to the 15 K data is then composed of the same Lorentzian found at 30 K together with a Mattis-Bardeen and an extra Drude peak. The effect observed by Gorshunov et al., that the measured low frequency optical conductivity is higher than the thermally broken pairs in a Mattis-Bardeen term [83], is clearly shown in Fig. 6.16. Adding the Drude response in the superconducting phase (red dotted line) to the Mattis-Bardeen component (green dashed line), leads to a proper description of the data below 50 cm^{-1}. Note that the measured $\sigma_1(\omega)$ has a low frequency upturn with a width ~ 50 cm^{-1} that is much broader than the width ~ 10 cm^{-1} of the thermally broken pairs from the BCS contribution. Hence, the Mattis-Bardeen description fails below the gap in the superconducting state, but the introduction of an

additional Drude peak, which accounts for the additional low energy absorption, reconciles the model and the data. This extra absorption could be due to gap anisotropy of the electron pocket [25, 149–151], impurity localized levels inside an isotropic gap [152], or pair breaking due to interband impurity scattering in an $s_{\pm}$ symmetric gap [153, 154]. To confirm the origin of the additional low energy absorption, we compared the optical response of $Ba(Fe_{0.92}Co_{0.08})_2As_2$ with $Ba_{0.6}K_{0.4}Fe_2As_2$.

6.3 Comparison between the optimally K doped and Co doped Ba122 samples

In Chapter 4, we discussed the crystal structure of the Ba122 system. The parent compound of the Ba122 system, $BaFe_2As_2$, contains distinct FeAs layers separated by barium atoms. When doping the parent compound with either holes or electrons, superconductivity arises in the FeAs planes. The $Ba_{1-x}K_xFe_2As_2$ is obtained by substituting the Ba atoms with K atoms which sit out of the FeAs planes. Hence, no impurity is introduced into the FeAs planes. However, $Ba(Fe_{1-x}Co_x)_2As_2$, derived from the substitution of Fe atoms with Co atoms, represents a different situation as Co atoms directly go into the FeAs planes. Structural defects caused by the in-plane doping can been considered as non-magnetic impurity. The non-magnetic impurity is not pair breaking in an s_{++} symmetry gap, but plays an extremely important role in the $s_{\pm}$ symmetry gap. When scattering by non-magnetic impurity between bands having s_+ and s_- symmetries takes place, Cooper pairs are annihilated and excess of unpaired quasiparticles appear in the superconducting state [25, 26]. In this sense, to grasp some information on the predicted $s_{\pm}$ symmetry for iron-based superconductors, it is instructive to compare the optical response of $Ba(Fe_{1-x}Co_x)_2As_2$ with $Ba_{1-x}K_xFe_2As_2$.

Figure 6.17 shows the optical conductivity for both materials at 5 K. In $Ba_{0.6}K_{0.4}Fe_2As_2$, $\sigma_1(\omega)$ vanishes, within error bars, below the smaller absorption threshold E_S^0. Hence, there is no sign of unpaired carriers at low frequencies in the superconducting state. Conversely, the data for $Ba(Fe_{0.92}Co_{0.08})_2As_2$ shows

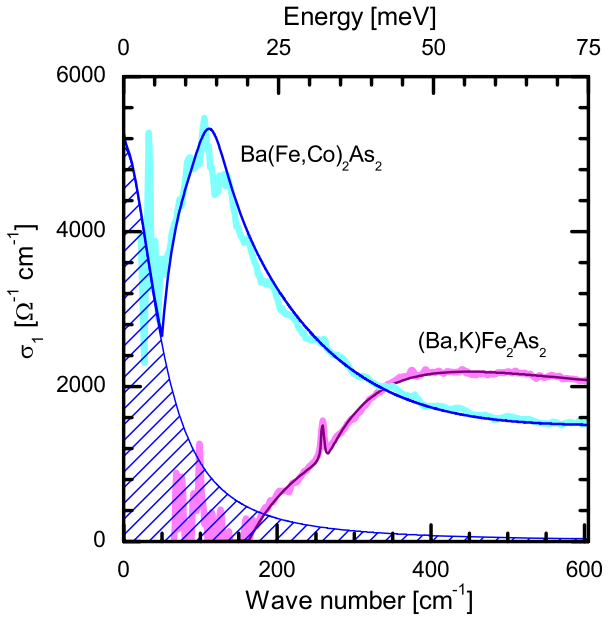

Figure 6.17: Optical conductivity at 5 K for $Ba(Fe_{0.92}Co_{0.08})_2As_2$ and $Ba_{0.6}K_{0.4}Fe_2As_2$.

a large low energy, sub-gap absorption in the superconducting state. This extra absorption is described by a Drude peak characterizing the unpaired carriers. Furthermore, residual low temperature specific heat [155] and penetration depth [156] are also observed in this system. The fact that the non-magnetic impurity introduced into the $Ba(Fe_{0.92}Co_{0.08})_2As_2$ induces pair-breaking matches naturally the $s_\pm$ gap symmetry proposed for iron-based superconductors. This result strongly supports an $s_\pm$ pairing symmetry in the Ba122 family superconductors.

6.4 Underdoped $Ba_{1-x}K_xFe_2As_2$

The top panel in Fig. 6.18 shows the temperature dependence of resistivity for $Ba_{1-x}K_xFe_2As_2$ (x = 0.2) sample. The $R-T$ curve exhibits a steep superconducting transition at $T_c = 19$ K. The inset of the top panel shows the derivative of the resistivity $d\rho/dT$ as a function of temperature. The sharp peak at 104 K in $d\rho/dT$ is related to the SDW transition. A small kink can be seen on the $R-T$ curve at the SDW transition temperature. The bottom panel displays the

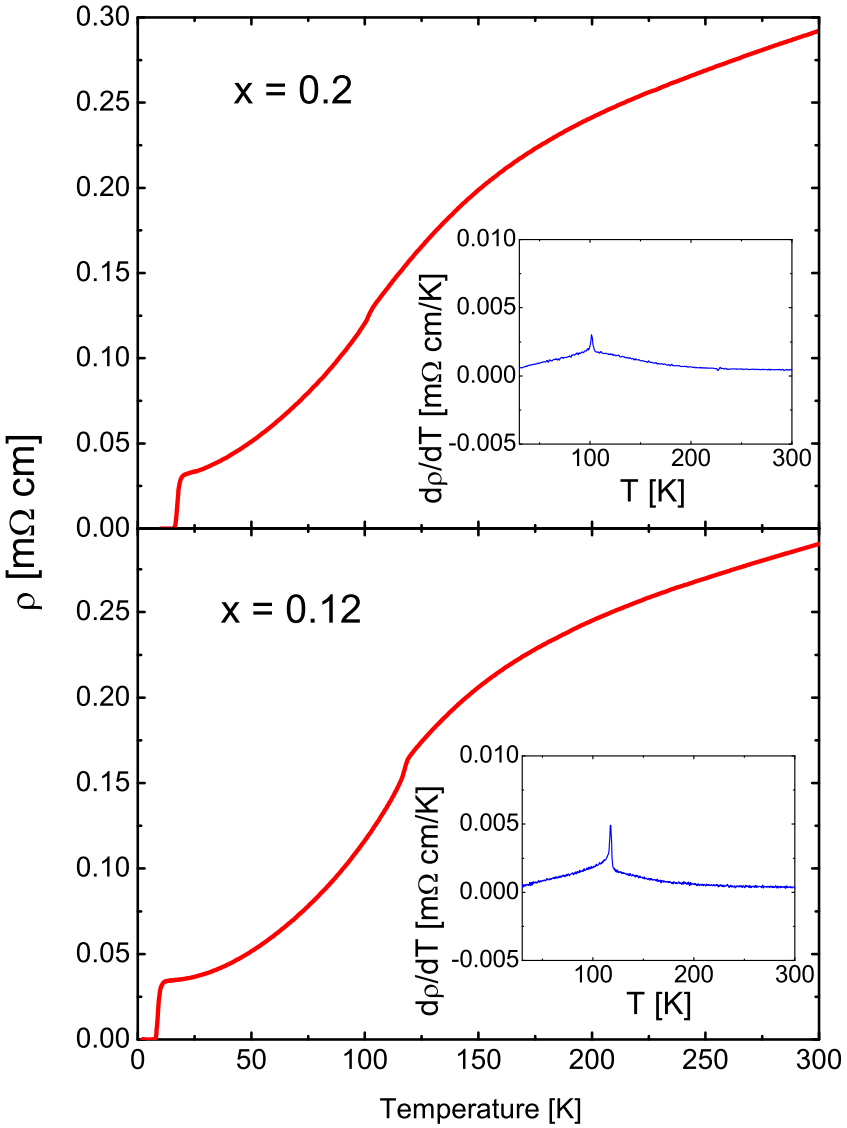

Figure 6.18: The top panel shows the temperature dependence of resistivity of $Ba_{1-x}K_xFe_2As_2$ (x = 0.2) single crystal. The $R-T$ curve is characterized by a steep superconducting transition at $T_c = 19$ K. The inset shows the derivative of the resistivity $d\rho/dT$ as a function of temperature. The sharp peak at 104 K in $d\rho/dT$ is associated with the SDW transition. A small kink can be seen in the $R-T$ curve at the SDW transition temperature. The bottom panel depicts the same curves for the x = 0.12 sample. $T_c = 11$ K, $T_{SDW} = 121$ K.

same curves for x = 0.12 sample. T_c = 11 K, T_{SDW} = 121 K.

6.4.1 Reflectivity

Figure 6.19 shows the measured infrared reflectivity at selected temperatures for both samples up to 1200 cm^{-1}. The inset in each panel displays the reflectivity of full measured range at 300 K. For the x = 0.2 sample, shown in the top panel, the reflectivity exhibits a metallic response and approaches to unity at zero frequency for high temperatures such as 150 and 300 K. Below T_{SDW} = 104 K, a substantial suppression of $R(\omega)$ at about 650 cm^{-1} sets in and intensifies with the temperature decrease. Simultaneously, the low frequency reflectivity increases faster towards unity at zero frequency. This is a clear evidence for the opening of a partial gap on the Fermi surface. The continuous increase of the reflectivity at low frequencies indicates that the material is still metallic in the SDW state. Below 75 K, defined as T^* in this section, another suppression of $R(\omega)$ appears in a lower energy scale ($\sim$ 150 cm^{-1}) suggesting the opening of a second partial gap with a smaller value. Note that the suppression due to the smaller partial gap is much weaker than the one due to the SDW transition. Upon crossing the superconducting transition which occurs at 19 K, the reflectivity below $\sim$ 150 cm^{-1} increases which is a signature of a superconducting gap, but in contrast to the optimally doped $Ba_{0.6}K_{0.4}Fe_2As_2$, the reflectivity does not reach a flat unity response expected for an s-wave gap.

Similar features manifest themselves on the reflectivity of the x = 0.12 sample as shown in the bottom panel of Fig. 6.19. However, marked differences exist between these two samples: (i) The suppression of $R(\omega)$ due to the SDW transition is stronger in the more underdoped (x = 0.12) sample; (ii) The smaller partial gap suppresses the reflectivity more weakly in the x = 0.12 sample; (iii) The more underdoped sample (x = 0.12) exhibits a weaker superconducting gap feature than the x = 0.2 sample.

6.4.2 Optical conductivity

The optical conductivity spectra for these two samples are derived from the measured reflectivity via Kramers-Kronig analysis. The top panel of Fig. 6.20

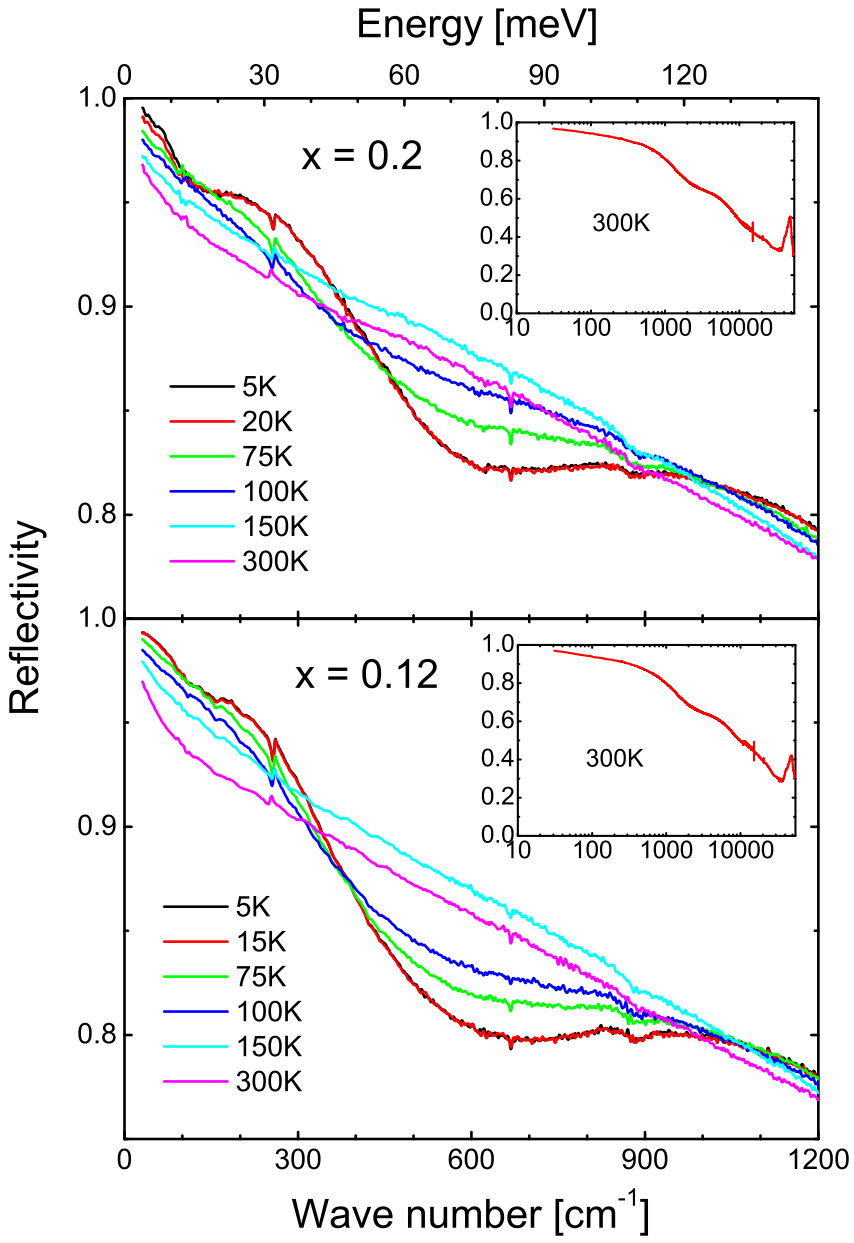

Figure 6.19: The top panel shows the reflectivity of $Ba_{1-x}K_xFe_2As_2$ (x = 0.2) single crystal below 1200 cm^{-1} at various temperatures. The inset shows the reflectivity up to 55000 cm^{-1} at 300 K. The bottom panel portrays the same spectra for the x = 0.12 sample.

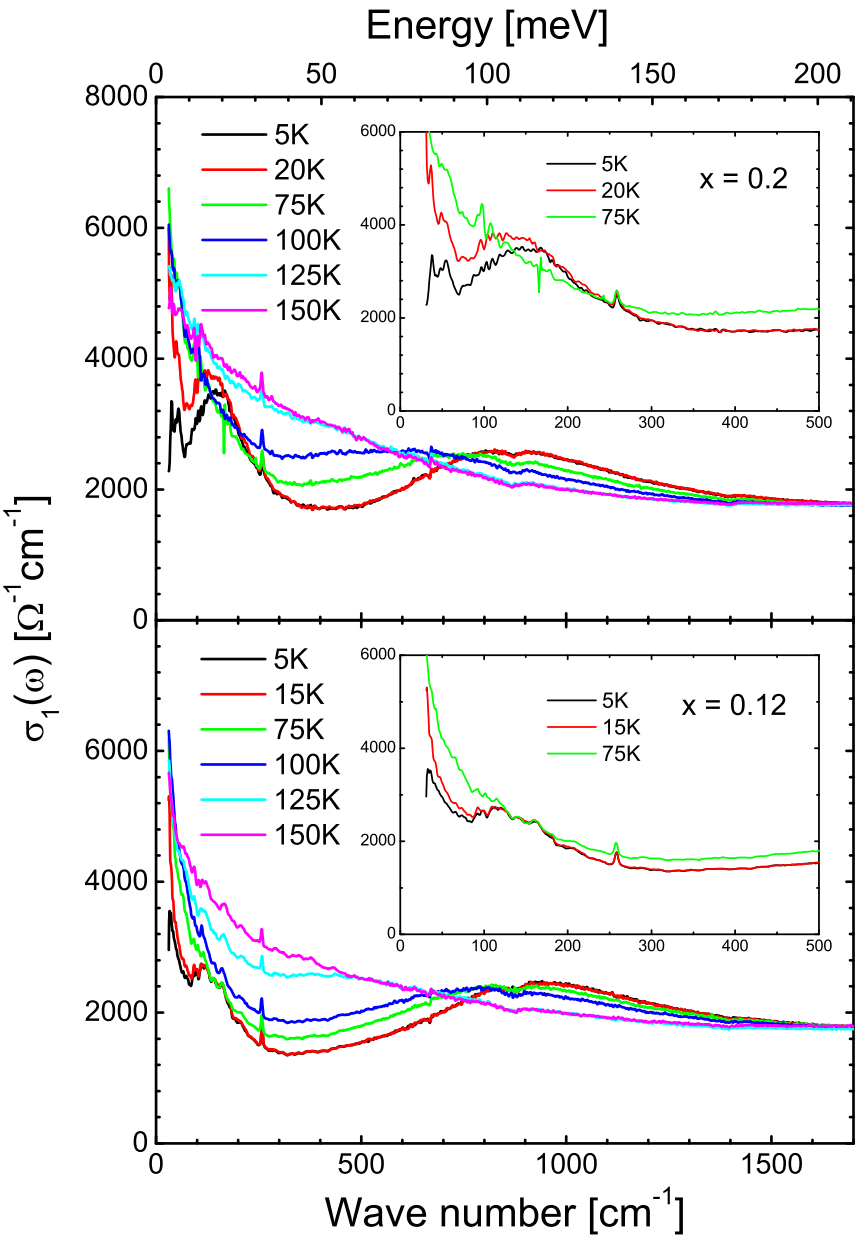

Figure 6.20: The top panel shows the optical conductivity of $Ba_{1-x}K_xFe_2As_2$ (x = 0.2) below 1700 cm^{-1} at several temperatures. The inset displays the enlarged view of $\sigma_1(\omega)$ at low frequencies. The bottom panel shows the same spectra for the x = 0.12 sample.

shows the real part of the optical conductivity of $Ba_{1-x}K_xFe_2As_2$ (x = 0.2) below 1700 cm^{-1} at several temperatures. At temperatures above T_{SDW}, 150 K and 125 K for instance, a Drude-like metallic response dominates the low frequency optical conductivity. Below T_{SDW} = 104 K, the spectra below about 650 cm^{-1} are severely suppressed; meanwhile, the optical conductivity increases in a higher energy scale from 650 cm^{-1} to 1700 cm^{-1}. The SDW state spectra $\sigma_1(\omega, T)$ and the normal state spectra $\sigma_1(\omega, 125K)$ intersect with each other, resulting in an intersection point at about 650 cm^{-1}. As the temperature decreases, both the low energy spectral suppression and the high energy bulge become stronger, and the intersection point moves to a higher energy scale. This spectral evolution manifests the behavior of a density wave like gap: transfer of low frequency spectral weight to high frequencies, an SDW gap in this material. If we take the intersection points as the gap values, we can see that the gap value increases with the temperature decrease. Below $T^* \sim$ 75 K, a second suppression in the optical conductivity below roughly 110 cm^{-1} with a bulge extending from about 110 cm^{-1} to 250 cm^{-1} sets in and develops with the temperature decrease, implying the opening of a smaller partial gap on the Fermi surface. The inset of Fig. 6.20 shows the enlarged view of the low temperature optical conductivity at low frequencies, so the smaller partial gap feature can be seen more clearly. Since it opens below 75 K, much lower than the SDW transition temperature (T_{SDW} = 104 K), it's unlikely due to the SDW transition. The origin of this smaller partial gap will be discussed below. The superconducting transition occurs at T_c = 19 K, which is characterized by the opening of a superconducting gap. As shown in the inset of Fig. 6.20, the reduction of the optical conductivity at low frequencies between 20 K and 5 K is due to the superconducting gap opening. The spectral weight lost in the transition is recovered by the weight of a δ function at zero frequency representing the infinite DC conductivity in the superconducting state. The zero frequency δ function is not visible in the $\sigma_1(\omega)$ spectra, because only finite frequency optical conductivity can be experimentally measured, but its weight can be easily calculated from the imaginary part of the optical conductivity [70, 146]. Note that, unlike the optimally doped $Ba_{0.6}K_{0.4}Fe_2As_2$, the low frequency optical conductivity does not vanish below an absorption edge in

the superconducting state. Large residual low frequency absorption appears in the underdoped samples, signaling the existence of nodes in the superconducting gap. Furthermore, the optical conductivity spectral depletion due to the superconducting condensate extends up to 180 cm^{-1}, almost the same energy scale as the smaller partial gap, hinting that the superconducting and smaller partial gaps share the same electronic states, and may have the same origin.

Very similar features are observed in the x = 0.12 sample, as shown in the bottom panel of Fig. 6.20. But the SDW gap opens at a higher temperature (T_{SDW} = 121 K) and the gap value shifts to a higher energy scale ($\sim$ 750 cm^{-1}). The low frequency spectral suppression due to the opening of the SDW gap is stronger indicating that a larger part of the Fermi surface is removed by the gap associated with the SDW phase transition in the more underdoped (x = 0.12) sample. In contrast to the SDW gap, both the smaller partial gap and the superconducting gap features are much weaker in the more underdoped sample. The evolution of the three gaps (SDW gap, the smaller partial gap and the superconducting gap) with doping also suggests that the smaller partial gap may have the same origin with the superconducting gap and play as a competitive order to the SDW phase.

6.4.3 spectral weight analysis

Both the superconducting and the SDW gaps have their respective origins. In order to investigate the origin of the smaller partial gap and the relations among these gaps, a restricted spectral weight analysis is indispensable.

The restricted spectral weight is defined as

$$SW_a^b = \int_a^b \sigma_1(\omega) d\omega \tag{6.7}$$

where a and b are the lower and upper cut-off frequencies respectively. By choosing appropriate lower and upper cut-off frequencies, one can study the relations among different phase transitions. When replacing a by 0 and b by ∞, the spectral weight is conserved.

Figure 6.21 shows the temperature dependence of the spectral weight, normalized by its value at 300 K, at different cut-off frequencies for the x = 0.2

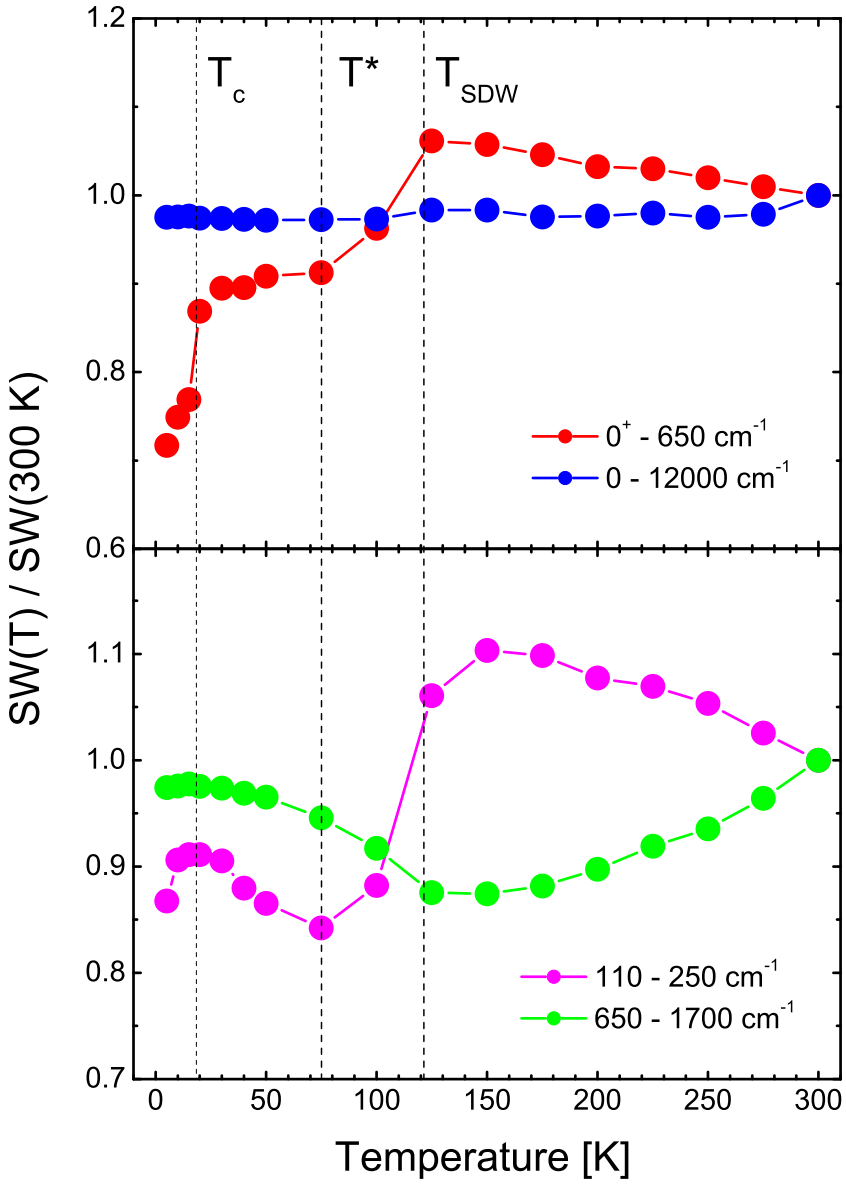

Figure 6.21: Temperature dependence of the spectral weight, $\mathrm{SW}_a^b = \int_a^b \sigma_1(\omega)d\omega$, normalized by its value at 300 K, for $Ba_{1-x}K_xFe_2As_2$ (x = 0.2) sample. a and b represent the lower and upper cut-off frequencies respectively. The vertical dashed lines denote T_c, T^* and T_{SDW} respectively.

sample. The vertical dashed lines denote T_c, T^* and T_{SDW} respectively. The blue solid circles in the top panel of Fig. 6.21 are the normalized spectral weight with cut-off frequencies $a = 0$ and $b = 12000$ cm^{-1} as a function of temperature. Here, the weight of the zero frequency δ function is included. Moreover, since the optical conductivity is measured only down to 30 cm^{-1}, we fit the low frequency normal state optical conductivity with a Drude model to estimate the spectral weight below 30 cm^{-1}. The upper cut-off frequency ($b = 12000$ cm^{-1}) is high enough to cover the whole spectrum responsible for the phase transitions in this material. Hence the blue solid circles form a flat line leveled at about unity, indicating that the sum rule is fulfilled.

The red solid circles in the top panel shows the temperature dependence of the normalized spectral weight with cut-off frequencies $a = 0^+$ and $b = 650$ cm^{-1}. Here 0^+ means that the superfluid weight is not included. The continuous increase of the normalized $\mathrm{SW}_{0^+}^{650}$ with decreasing T above T_{SDW} is related to narrowing of the Drude band. This is the typical optical response of a metallic material. A strong spectral weight suppression occurs at T_{SDW}, which is clearly associated with the opening of the SDW gap. At T_c, another sharp drop of the spectral weight breaks in, implying the superconducting gap opening. Whereas, no feature is observed at T^*, because the upper cut-off frequency ($b = 650$ cm^{-1}) is sufficiently high to cover the excitation spectrum responsible for the smaller partial gap.

The temperature dependence of normalized SW_{650}^{1700}, shown as green solid circles in the bottom panel of Fig. 6.21, provides clues about the relation between the superconducting and SDW gaps. Above T_{SDW}, the material shows metallic response which can be described by a Drude peak centered at zero frequency. With the temperature decrease, the DC conductivity increases and the scattering rate reduces. The continuous narrowing of the Drude band induces a transfer of spectral weight from mid infrared to far infrared ranges, resulting in the continuous decrease of the spectral weight in the 650 - 1700 cm^{-1} range. Below T_{SDW}, the opposite behavior dominates the optical conductivity. The SDW gap depletes the spectral weight below 650 cm^{-1} and transfers it to the 650 - 1700 cm^{-1} range, leading to the continuous increase of SW_{650}^{1700} with decreasing T. This

behavior continues into the superconducting state and does not show any feature at T_c. These observations indicate that the SDW and superconducting gaps are separate and even act as competitive orders in this material. Here it is expected that, if a partial gap is due to a precursor order of superconductivity, for example preformed pairs without phase coherence, once a long range superconductivity is established below T_c, a significant part of the spectral weight transferred to high frequencies by the partial gap should be transferred back to low energies and join the superconducting condensate [157, 158]. Whereas, the partial gap due to a competitive order of superconductivity depletes the low-energy spectral weight available for superconductivity and holds it in high frequency scale without transferring it to superfluid weight below T_c. From the normalized SW_{650}^{1700} *vs* T curve (green solid circles) we note that no loss of spectral weight is observed at T_c. This means that the spectral weight transferred to high frequencies by the SDW gap remains in the high frequency scale and does not join the superconducting condensate. Therefore, the SDW phase acts as a competitive order to superconductivity in this material.

In this sense, the origin of the smaller partial gap and its relation to superconductivity can be revealed by a close inspection of the temperature dependence of normalized SW_{110}^{250}, shown as pink solid circles in the bottom panel. Above T^*, the curve shows the same feature as the normalized $\mathrm{SW}_{0^+}^{650}$ *vs* T curve: continuous increase upon cooling down followed by a suppression at T_{SDW} due to the SDW gap opening. At T^*, the spectral weight in the 110 - 250 cm^{-1} range reaches a minimum and starts to increase with decreasing temperature. This is due to the opening of the smaller partial gap. This smaller partial gap, opening at T^*, depletes the spectral weight below 110 cm^{-1} and retrieves it in the 110 - 250 cm^{-1} frequency range, leading to the increase of SW_{110}^{250} below T^*. An interesting phenomena happens to the smaller partial gap when the material undergoes the superconducting transition. In contrast to the case of the SDW partial gap, a significant loss of the spectral weight in the 110 - 250 cm^{-1} frequency range is observed below T_c. This observation indicates that the spectral weight transferred to the 110 - 250 cm^{-1} range by the smaller partial gap joins the superconducting condensate when superconductivity is established in the material. Hence, the

smaller partial gap is likely a precursor order with respect to the superconductivity, such as preformed pairs without phase coherence.

Chapter 7

Summary

In this thesis, we measured the optical reflectivity of $Ba_{1-x}K_xFe_2As_2$ (x = 0.4, 0.2, and 0.12) and $Ba(Fe_{1-x}Co_x)_2As_2$ (x = 0.08) samples at 18 different temperatures from 5 to 300 K. These systematic measurements allow us to investigate both the temperature and doping dependence of the optical response of the K doped Ba122 system iron-based superconductors and compare it with the Co doped Ba122 system.

In the optimally doped $Ba_{1-x}K_xFe_2As_2$ (x = 0.4) sample, upon entering the superconducting state, the low frequency reflectivity increases and reaches a flat unity response. The conductivity vanishes below an absorption edge at about 160 cm^{-1}, and no residual conductivity appears at low frequencies in the superconducting state. These optical responses strongly indicate the opening of a superconducting gap with s-wave symmetry.

Quite differently in the optimally doped $Ba(Fe_{1-x}Co_x)_2As_2$ (x = 0.08) sample, below T_c, the reflectivity turns up at low frequencies but does not reach a flat unity response, and large residual conductivity exists at low energies representing unpaired quasiparticles. These low frequency optical responses do not favor the s-wave pairing symmetry.

This remarkable difference in low frequency optical response between the K and Co doped samples contains important information about the pairing symmetry in the Ba122 iron-based superconductors. In the K doped sample, K atoms sit at the Ba sites, out of the FeAs planes which are responsible for superconductivity. This out-of-plane doping does not disturb the FeAs planes, and no defect is introduced into the FeAs planes, hence the gap symmetry manifests itself in a straightforward way: s-wave symmetry. As optical method is not phase sensitive, it can not distinguish between s_{++} and $s_{\pm}$. However, in the Co doped sample,

Co atoms go into the FeAs planes, and the disturbance to the FeAs planes causes structural defects which can be considered as non-magnetic impurities. In an s_{++} symmetry gap, non-magnetic impurities are not pair-breaking since the order parameters in different bands have the same sign. But in an $s_{\pm}$ symmetry gap, a different situation is expected. If the order parameters in different bands have opposite signs, when scattered from one band to another by non-magnetic impurities, the Cooper pairs are broken up. Here, in the Co doped Ba122 system, non-magnetic impurities in the FeAs planes induce large residual conductivity at low frequencies representing unpaired quasiparticles, namely, the non-magnetic impurities in this material are pair-breaking. This observation is in strong support of an $s_{\pm}$ gap symmetry in the Ba122 system iron-based superconductors.

In the underdoped $Ba_{1-x}K_xFe_2As_2$ (x = 0.2 and 0.12) samples, the opening of the SDW and superconducting gaps is clearly observed from the optical spectra at low temperatures, additionally, a small partial gap opens at about 110 cm^{-1} when the temperature is below 75 K. As this small partial gap opens below 75 K, much lower than the SDW transition temperature, it's unlikely due to the SDW transition.

In order to clarify the origin of the small partial gap and its relation to superconductivity, we performed a spectral weight analysis. From our spectral weight analysis, we found that, the small partial gap transfers the low frequency spectral weight to an energy scale just above its value, but when the long range superconducting order is established in the material, the spectral weight, transferred to high frequencies by the small partial gap, joins the superconducting condensate. This indicates that the small partial gap shares the same electronic states with the superconducting gap, suggesting that the small partial gap is associated with a precursor order to superconductivity. In contrast, the SDW gap transfers the low energy spectral weight to high energy scale and holds it at high frequencies rather than transfer it to the superfluid weight, so the SDW gap depletes the low frequency electronic states available for superconducting condensate. This result suggests that the SDW acts as a competitive order to superconductivity.

The doping dependence of these gaps is also supportive of this scenario. In

the more underdoped sample (x = 0.12), the SDW gap feature is stronger while both the superconducting and small partial gaps feature become weaker, i.e. the superconducting and small partial gaps exhibit the same doping evolution while the SDW gap evolves oppositely with doping. This result implies that the small partial gap may have the same origin as the superconducting gap and be associated with a precursor order to superconductivity while the SDW phase is in favor as a competitive order.

Appendix A

Useful equations in optical spectroscopy

Plasma frequency:

$$\Omega_p^2 = \frac{Z_0}{\pi^2}\int_0^{\omega_{sp}} \sigma_1(\omega)d\omega \tag{A.1}$$

Superfluid weight:

$$SW_s = \int_{0^+}^{\infty} [\sigma_1^n(\omega) - \sigma_1^s(\omega)]d\omega \tag{A.2}$$

Superfluid plasma frequency:

$$\Omega_{ps}^2 = \frac{Z_0}{\pi^2}\int_{0^+}^{\infty} [\sigma_1^n(\omega) - \sigma_1^s(\omega)]d\omega = \frac{Z_0}{\pi^2} SW_s \tag{A.3}$$

Penetration depth:

$$\lambda = \frac{1}{2\pi\Omega_{ps}} \tag{A.4}$$

The relation between the imaginary part of the optical conductivity and the superfluid plasma frequency:

$$\sigma_2(\omega) = \frac{2\pi}{Z_0\omega}\Omega_{ps}^2 - \frac{2\omega}{\pi}\int_{0^+}^{\infty} \frac{\sigma_1(\omega')}{\omega'^2 - \omega^2}d\omega', \tag{A.5}$$

Drude model:

$$\hat{\sigma}(\omega) = \frac{2\pi}{Z_0}\frac{\Omega_p^2}{\tau^{-1} - i\omega} \tag{A.6}$$

Extended Drude model:

$$\begin{aligned}\hat{\sigma}(\omega, T) &= \frac{2\pi}{Z_0}\frac{\Omega_p^2}{\tau^{-1}(\omega, T) - i\omega[1 + \lambda(\omega, T)]} \\ &= \frac{2\pi i}{Z_0}\frac{\Omega_p^2}{\omega - 2\Sigma^{op}(\omega, T)}\end{aligned} \tag{A.7}$$

where Σ^{op} is the optical self-energy, which is defined as:

$$\Sigma^{op}(\omega, T) \equiv \Sigma_1^{op}(\omega, T) + i\Sigma_2^{op}(\omega, T) \tag{A.8}$$

Real and imaginary parts of the optical self-energy:

$$-2\Sigma_1^{op}(\omega,T) = \omega\lambda(\omega,T) = \omega(\frac{m^*}{m} - 1) \tag{A.9}$$

$$\lambda(\omega,T) = \frac{m^*}{m} - 1 = \frac{2\pi\Omega_p^2}{Z_0}\frac{1}{\omega}Im[\frac{1}{\sigma}] \tag{A.10}$$

$$-2\Sigma_2^{op}(\omega,T) = \frac{1}{\tau(\omega,T)} = \frac{2\pi\Omega_p^2}{Z_0}Re[\frac{1}{\sigma}] \tag{A.11}$$

Kinetic energy of carriers:

$$\begin{aligned} E_k &= -\frac{2\hbar^2 V}{\pi e^2 a^2}\int_0^{\omega_c}\sigma_1(\omega)d\omega \\ &= -\frac{2\hbar^2 c}{\pi e^2}\int_0^{\omega_c}\sigma_1(\omega)d\omega \end{aligned} \tag{A.12}$$

where a is the in-plane lattice constant, c is the c-axis lattice constant and V is the unit cell volume.

Appendix B

Conversion table

	E [eV]	T [K]	f [Hz]	ν [cm^{-1}]
E [eV]	1	11 605	2.418×10^{14}	8066
T [K]	8.617×10^{-5}	1	2.084×10^{10}	0.671
f [Hz]	4.136×10^{-15}	4.799×10^{-11}	1	3.336×10^{-11}
ν [cm^{-1}]	1.240×10^{-4}	1.490	2.998×10^{10}	1

Table B.1: The conversion between energy E, temperature T, frequency f, wave number $\nu = 1/\lambda$. Some basic physical constants are used for these conversions: the elementary charge $e = 1.602 \times 10^{-19}$ A·s, the Boltzmann constant $k_B = 1.381 \times 10^{-23}$ J·K^{-1}, and the Planck's constant $\hbar = 1.055 \times 10^{-34}$ J·s, the Light speed in a vacuum $c = 2.998 \times 10^{8}$ m·s^{-1}.

Quantity	Gaussian (cgs) system	SI (mks) system
Speed of light	c	$c = \frac{1}{\sqrt{\epsilon_0 \mu_0}}$
Electric field	$\mathbf{E}$	$\sqrt{4\pi\epsilon_0}\ \mathbf{E}$
Electric displacement	$\mathbf{D}$	$\sqrt{\frac{4\pi}{\epsilon_0}}\ \mathbf{D}$
Charge density	ρ	$\frac{1}{\sqrt{4\pi\epsilon_0}}\rho$
Electric polarization	$\mathbf{P}$	$\frac{1}{\sqrt{4\pi\epsilon_0}}\ \mathbf{P}$
Current density	$\mathbf{J}$	$\frac{1}{\sqrt{4\pi\epsilon_0}}\ \mathbf{J}$
Dielectric constant	$\hat{\epsilon}$	$\frac{\hat{\epsilon}}{\epsilon_0}$
Conductivity	$\hat{\sigma}$	$\frac{\hat{\sigma}}{4\pi\epsilon_0}$
Magnetic field	$\mathbf{H}$	$\sqrt{4\pi\mu_0}\ \mathbf{H}$
Magnetic induction	$\mathbf{B}$	$\sqrt{\frac{4\pi}{\mu_0}}\ \mathbf{B}$
Magnetization	$\mathbf{M}$	$\sqrt{\frac{4\pi}{\mu_0}}\ \mathbf{M}$
Permeability	$\hat{\mu}$	$\frac{\hat{\mu}}{\mu_0}$
Impedance	$\hat{Z}$	$4\pi\epsilon_0\hat{Z}$

Table B.2: The conversion between the cgs and SI unit systems. Equations in cgs units can be converted into those in the SI system via this table by replacing the relevant symbols with the corresponding one one the right column of the table.

Appendix C

The fundamental constants

Quantity	Values in SI units
Speed of light in a vacuum	$c = 2.99792458 \times 10^8 \mathrm{m} \cdot \mathrm{s}^{-1}$
Permittivity of vacuum	$\epsilon_0 = 8.8542 \times 10^{-12}$ A $\cdot$ s $\cdot$ V^{-1} $\cdot$ m^{-1}
Permeability of vacuum	$\mu_0 = 1.2566 \times 10^{-6}$ V $\cdot$ s $\cdot$ A^{-1} $\cdot$ m^{-1}
Elementary charge	$e = 1.602189 \times 10^{-19}$ A $\cdot$ s
Mass of electron	$m = 9.010953 \times 10^{-31}$ kg
Mass of proton	$m_p = 1.67261 \times 10^{-27}$ kg
Mass of neutron	$m_n = 1.67482 \times 10^{-27}$ kg
Planck's constant	$h = 6.626176 \times 10^{-34}$ J $\cdot$ s $\hbar = h/2\pi = 1.054589 \times 10^{-34}$ J $\cdot$ s
Boltzmann's constant	$k_B = 1.38066 \times 10^{-23}$ J $\cdot$ K^{-1}
Avogadro's constant	$N_A = 6.02205 \times 10^{23}$ mol^{-1}

Table C.1: Fundamental physical constants

References

[1] J. Bardeen, L. N. Cooper, and J. R. Schrieffer. Microscopic Theory of Superconductivity. *Phys. Rev.*, 106:162–164, Apr 1957.

[2] J. Bardeen, L. N. Cooper, and J. R. Schrieffer. Theory of Superconductivity. *Phys. Rev.*, 108:1175–1204, Dec 1957.

[3] J. G. Bednorz and K. A. Müller. Possible high-Tc superconductivity in the Ba-La-Cu-O system. *Zeitschrift f*ü *r Physik B Condensed Matter*, 64:189–193, 1986. 10.1007/BF01303701.

[4] Jun Nagamatsu, Norimasa Nakagawa, Takahiro Muranaka, Yuji Zenitani, and Jun Akimitsu. Superconductivity at 39 K in magnesium diboride. *Nature*, 410(6824):63–64, March 2001.

[5] Yoichi Kamihara, Hidenori Hiramatsu, Masahiro Hirano, Ryuto Kawamura, Hiroshi Yanagi, Toshio Kamiya, and Hideo Hosono. Iron-Based Layered Superconductor: LaOFeP. *Journal of the American Chemical Society*, 128(31):10012–10013, 2006. PMID: 16881620.

[6] Takumi Watanabe, Hiroshi Yanagi, Toshio Kamiya, Yoichi Kamihara, Hidenori Hiramatsu, Masahiro Hirano, and Hideo Hosono. Nickel-Based Oxyphosphide Superconductor with a Layered Crystal Structure, LaNiOP. *Inorganic Chemistry*, 46(19):7719–7721, 2007.

[7] Marcus Tegel, Daniel Bichler, and Dirk Johrendt. Synthesis, crystal structure and superconductivity of LaNiPO. *Solid State Sciences*, 10(2):193 – 197, 2008.

[8] Y. Kamihara, T. Watanabe, M. Hirano, and H. Hosono. Iron-Based Layered Superconductor La[$O_{1-x}F_x$]FeAs (x = 0.05-0.12) with T_c = 26 K. *J.Am.Chem.Soc.*, 130:3296, 2008.

[9] Fong-Chi Hsu, Jiu-Yong Luo, Kuo-Wei Yeh, Ta-Kun Chen, Tzu-Wen Huang, Phillip M. Wu, Yong-Chi Lee, Yi-Lin Huang, Yan-Yi Chu, Der-Chung Yan, and Maw-Kuen Wu. Superconductivity in the PbO-type structure α-FeSe. *Proc. Natl. Acad. Sci.*, 105:14262, 2008.

[10] M. H. Fang, H. M. Pham, B. Qian, T. J. Liu, E. K. Vehstedt, Y. Liu, L. Spinu, and Z. Q. Mao. Superconductivity close to magnetic instability in $Fe(Se_{1-x}Te_x)_{0.82}$. *Phys. Rev. B*, 78:224503, Dec 2008.

[11] Leon N. Cooper. Bound Electron Pairs in a Degenerate Fermi Gas. *Phys. Rev.*, 104:1189–1190, Nov 1956.

[12] H. Fröhlich. Theory of the Superconducting State. I. The Ground State at the Absolute Zero of Temperature. *Phys. Rev.*, 79:845–856, Sep 1950.

[13] Emanuel Maxwell. Isotope Effect in the Superconductivity of Mercury. *Phys. Rev.*, 78:477–477, May 1950.

[14] C. A. Reynolds, B. Serin, W. H. Wright, and L. B. Nesbitt. Superconductivity of Isotopes of Mercury. *Phys. Rev.*, 78:487–487, May 1950.

[15] M. Tinkham and R. A. Ferrell. Determination of the Superconducting Skin Depth from the Energy Gap and Sum Rule. *Phys. Rev. Lett.*, 2(8):331–333, Apr 1959.

[16] H. Suhl, B. T. Matthias, and L. R. Walker. Bardeen-Cooper-Schrieffer Theory of Superconductivity in the Case of Overlapping Bands. *Phys. Rev. Lett.*, 3(12):552–554, Dec 1959.

[17] A. A. Abrikosov and L. P. Gorkov. Contribution to the theory of superconducting alloys with paramagnetic impurities. *Sov. Phys. JETP*, 12:1243, 1961.

[18] F. Reif and Michael A. Woolf. Energy gap in superconductors containing paramagnetic impurities. *Phys. Rev. Lett.*, 9:315–316, Oct 1962.

[19] Igor I. Mazin. Superconductivity gets an iron boost. *Nature*, 464:183, 2010.

[20] B. O. Wells, Z. X. Shen, D. S. Dessau, W. E. Spicer, D. B. Mitzi, L. Lombardo, A. Kapitulnik, and A. J. Arko. Evidence for **k** -dependent, in-plane anisotropy of the superconducting gap in $Bi_2Sr_2CaCu_2O_{8+\delta}$. *Phys. Rev. B*, 46:11830–11834, Nov 1992.

[21] I. I. Mazin and V. P. Antropov. Electronic structure, electron-phonon coupling, and multiband effects in MgB_2. *Physica C: Superconductivity*, 385(1-2):49 – 65, 2003.

[22] K. Haule, J. H. Shim, and G. Kotliar. Correlated Electronic Structure of $LaO_{1-x}F_xFeAs$. *Phys. Rev. Lett.*, 100(22):226402, Jun 2008.

[23] D. J. Singh and M.-H. Du. Density Functional Study of $LaFeAsO_{1-x}F_x$: A Low Carrier Density Superconductor Near Itinerant Magnetism. *Phys. Rev. Lett.*, 100(23):237003, Jun 2008.

[24] I. I. Mazin, D. J. Singh, M. D. Johannes, and M. H. Du. Unconventional Superconductivity with a Sign Reversal in the Order Parameter of $LaFeAsO_{1-x}F_x$. *Phys. Rev. Lett.*, 101(5):057003, Jul 2008.

[25] A. V. Chubukov, M. G. Vavilov, and A. B. Vorontsov. Momentum dependence and nodes of the superconducting gap in the iron pnictides. *Phys. Rev. B*, 80(14):140515, Oct 2009.

[26] Yunkyu Bang, Han-Yong Choi, and Hyekyung Won. Impurity effects on the $\pm s$ -wave state of the iron-based superconductors. *Phys. Rev. B*, 79(5):054529, Feb 2009.

[27] M. K. Wu, J. R. Ashburn, C. J. Torng, P. H. Hor, R. L. Meng, L. Gao, Z. J. Huang, Y. Q. Wang, and C. W. Chu. Superconductivity at 93 K in a new mixed-phase Y-Ba-Cu-O Compound System at ambient pressure. *Phys. Rev. Lett.*, 58:908–910, Mar 1987.

[28] A. Schilling, M. Cantoni, J. D. Guo, and H. R. Ott. Superconductivity above 130 K in the Hg ‐ Ba ‐ Ca ‐ Cu ‐ O system. *Nature*, 363:56, 1993.

[29] M. Nuñez-Regueiro, J. L. Tholence, E. V. Antipov, J. J. Capponi, and M. Marezio. Pressure-Induced Enhancement of T_c Above 150 K in Hg-1223. *Science*, 262(5130):97–99, 1993.

[30] C. W. Chu, L. Gao, F. Chen, Z. J. Huang, R. L. Meng, and Y. Y. Xue. Superconductivity above 150 K in $HgBa_2Ca_2Cu_3O_{8+\delta}$ at high pressures. *Nature*, 365:323, 1993.

[31] H. A. Mook, M. Yethiraj, G. Aeppli, T. E. Mason, and T. Armstrong. Polarized neutron determination of the magnetic excitations in $YBa_2Cu_3O_7$. *Phys. Rev. Lett.*, 70:3490–3493, May 1993.

[32] H. F. Fong, P. Bourges, Y. Sidis, L. P. Regnault, A. Ivanov, G. D. Gu, N. Koshizuka, and B. Keimer. Neutron scattering from magnetic excitations in $Bi_2Sr_2CaCu_2O_{8+\delta}$. *Nature*, 398(6728):588–591, April 1999.

[33] Pengcheng Dai, H. A. Mook, G. Aeppli, S. M. Hayden, and F. Dogan. Resonance as a measure of pairing correlations in the high-T_c superconductor $YBa_2Cu_3O_{6.6}$. *Nature*, 406(6799):965–968, August 2000.

[34] H. He, P. Bourges, Y. Sidis, C. Ulrich, L. P. Regnault, S. Pailhès, N. S. Berzigiarova, N. N. Kolesnikov, and B. Keimer. Magnetic Resonant Mode in the Single-Layer High-Temperature Superconductor $Tl_2Ba_2CuO_{6+\delta}$. *Science*, 295(5557):1045–1047, 2002.

[35] Tom Timusk and Bryan Statt. The pseudogap in high-temperature superconductors: an experimental survey. *Reports on Progress in Physics*, 62(1):61, 1999.

[36] H. Alloul, T. Ohno, and P. Mendels. ^{89}Y NMR evidence for a fermi-liquid behavior in $YBa_2Cu_3O_{6+x}$. *Phys. Rev. Lett.*, 63:1700–1703, Oct 1989.

[37] H. Ding, T. Yokoya, J. C. Campuzano, T. Takahashi, M. Randeria, M. R. Norman, T. Mochiku, K. Kadowaki, and J. Giapintzakis. Spectroscopic evidence for a pseudogap in the normal state of underdoped high-T_c superconductors. *Nature*, 382:51, 1996.

[38] A. G. Loeser, Z.-X. Shen, D. S. Dessau, D. S. Marshall, C. H. Park, P. Fournier, and A. Kapitulnik. Excitation Gap in the Normal State of Underdoped $Bi_2Sr_2CaCu_2O_{8+\delta}$. *Science*, 273(5273):325–329, 1996.

[39] V. M. Krasnov, A. Yurgens, D. Winkler, P. Delsing, and T. Claeson. Evidence for Coexistence of the Superconducting Gap and the Pseudogap in Bi-2212 from Intrinsic Tunneling Spectroscopy. *Phys. Rev. Lett.*, 84:5860–5863, Jun 2000.

[40] C. C. Homes, T. Timusk, R. Liang, D. A. Bonn, and W. N. Hardy. Optical conductivity of c axis oriented $YBa_2Cu_3O_{6.70}$: Evidence for a pseudogap. *Phys. Rev. Lett.*, 71(10):1645–1648, Sep 1993.

[41] M. Reedyk, T. Timusk, Y.-W. Hsueh, B. W. Statt, J. S. Xue, and J. E. Greedan. Far-infrared investigation of the pseudogap in underdoped $Pb_2Sr_2(Y/Ca)Cu_3O_8$. *Phys. Rev. B*, 56:9129–9133, Oct 1997.

[42] Ch. Renner, B. Revaz, J.-Y. Genoud, K. Kadowaki, and Ø. Fischer. Pseudogap Precursor of the Superconducting Gap in Under- and Overdoped $Bi_2Sr_2CaCu_2O_{8+\delta}$. *Phys. Rev. Lett.*, 80:149–152, Jan 1998.

[43] M. R. Norman, H. Ding, M. Randeria, J. C. Campuzano, T. Yokoya, T. Takeuchi, T. Takahashi, T. Mochiku, K. Kadowaki, P. Guptasarma, and D. G. Hinks. Destruction of the Fermi surface in underdoped high-Tc superconductors. *Nature*, 392(6672):157–160, March 1998.

[44] M. Kugler, O. Fischer, Ch. Renner, S. Ono, and Yoichi Ando. Scanning Tunneling Spectroscopy of $Bi_2Sr_2CuO_{6+\delta}$: New Evidence for the Common Origin of the Pseudogap and Superconductivity. *Phys. Rev. Lett.*, 86:4911–4914, May 2001.

[45] Yayu Wang, Lu Li, and N. P. Ong. Nernst effect in high-T_c superconductors. *Phys. Rev. B*, 73:024510, Jan 2006.

[46] A. Kanigel, U. Chatterjee, M. Randeria, M. R. Norman, S. Souma, M. Shi, Z. Z. Li, H. Raffy, and J. C. Campuzano. Protected Nodes and the Col-

lapse of Fermi Arcs in High-T_c Cuprate Superconductors. *Phys. Rev. Lett.*, 99:157001, Oct 2007.

[47] Jianqiao Meng, Wentao Zhang, Guodong Liu, Lin Zhao, Haiyun Liu, Xiaowen Jia, Wei Lu, Xiaoli Dong, Guiling Wang, Hongbo Zhang, Yong Zhou, Yong Zhu, Xiaoyang Wang, Zhongxian Zhao, Zuyan Xu, Chuangtian Chen, and X. J. Zhou. Monotonic d -wave superconducting gap of the optimally doped $Bi_2Sr_{1.6}La_{0.4}CuO_6$ superconductor by laser-based angle-resolved photoemission spectroscopy. *Phys. Rev. B*, 79(2):024514, Jan 2009.

[48] Guy Deutscher. Coherence and single-particle excitations in the high-temperature superconductors. *Nature*, 397(6718):410–412, February 1999.

[49] M. Le Tacon, A. Sacuto, A. Georges, G. Kotliar, Y. Gallais, D. Colson, and A. Forget. Two energy scales and two distinct quasiparticle dynamics in the superconducting state of underdoped cuprates. *Nat Phys*, 2(8):537–543, August 2006.

[50] Kiyohisa Tanaka, W. S. Lee, D. H. Lu, A. Fujimori, T. Fujii, Risdiana, I. Terasaki, D. J. Scalapino, T. P. Devereaux, Z. Hussain, and Z.-X. Shen. Distinct Fermi-Momentum-Dependent Energy Gaps in Deeply Underdoped Bi2212. *Science*, 314(5807):1910–1913, 2006.

[51] M. C. Boyer, W. D. Wise, Kamalesh Chatterjee, Ming Yi, Takeshi Kondo, T. Takeuchi, H. Ikuta, and E. W. Hudson. Imaging the two gaps of the high-temperature superconductor $Bi_2Sr_2CuO_{6+x}$. *Nat Phys*, 3(11):802–806, November 2007.

[52] Li Yu, D. Munzar, A. V. Boris, P. Yordanov, J. Chaloupka, Th. Wolf, C. T. Lin, B. Keimer, and C. Bernhard. Evidence for Two Separate Energy Gaps in Underdoped High-Temperature Cuprate Superconductors from Broadband Infrared Ellipsometry. *Phys. Rev. Lett.*, 100(17):177004, May 2008.

[53] Takeshi Kondo, Rustem Khasanov, Tsunehiro Takeuchi, Jo ¨ rg Schmalian, and Adam Kaminski. Competition between the pseudogap and superconductivity in the high-Tc copper oxides. *Nature*, 457:296, 2009.

[54] J. Singleton. *Band Theory and Electronic Properties of Solids*. Oxford University Press, 2001.

[55] D. N. Basov, Richard D. Averitt, Dirk van der Marel, Martin Dressel, and Kristjan Haule. Electrodynamics of correlated electron materials. *Rev. Mod. Phys.*, 83(2):471–542, Jun 2011.

[56] Martin Dressel and George Grüner. *Electrodynamics of Solids*. Cambridge University press, 2002.

[57] 方容川. 固体光谱学. 中国科学技术大学出版社, 2003.

[58] Frederick Wooten. *Optical Properties of Solids*. Academic Press, 1972.

[59] R. P. S. M. Lobo, R. L. Moreira, D. Lebeugle, and D. Colson. Infrared phonon dynamics of a multiferroic $BiFeO_3$ single crystal. *Phys. Rev. B*, 76(17):172105, Nov 2007.

[60] Z.-T. Zhu, J. L. Musfeldt, Z. S. Teweldemedhin, and M. Greenblatt. Anisotropic ab-plane optical response of the charge-density-wave superconductor $P_4W_{14}O_{50}$. *Phys. Rev. B*, 65:214519, Jun 2002.

[61] W. Z. Hu, J. Dong, G. Li, Z. Li, P. Zheng, G. F. Chen, J. L. Luo, and N. L. Wang. Origin of the Spin Density Wave Instability in $A\mathrm{Fe_2As_2}$ (A = Ba,Sr) as Revealed by Optical Spectroscopy. *Phys. Rev. Lett.*, 101(25):257005, Dec 2008.

[62] W. Z. Hu, G. Li, P. Zheng, G. F. Chen, J. L. Luo, and N. L. Wang. Optical study of the spin-density-wave properties of single-crystalline $Na_{1-\delta}FeAs$. *Phys. Rev. B*, 80(10):100507, Sep 2009.

[63] H. S. Somal, B. J. Feenstra, J. Schützmann, Jae Hoon Kim, Z. H. Barber, V. H. M. Duijn, N. T. Hien, A. A. Menovsky, Mario Palumbo, and D. van der Marel. Grazing Incidence Infrared Reflectivity of $La_{1.85}Sr_{0.15}CuO_4$ and NbN. *Phys. Rev. Lett.*, 76:1525–1528, Feb 1996.

[64] Richard A. Ferrell and Rolfe E. Glover. Conductivity of Superconducting Films: A Sum Rule. *Phys. Rev.*, 109:1398–1399, Feb 1958.

[65] D. C. Mattis and J. Bardeen. Theory of the Anomalous Skin Effect in Normal and Superconducting Metals. *Phys. Rev.*, 111(2):412–417, Jul 1958.

[66] W. Zimmermann, E.H. Brandt, M. Bauer, E. Seider, and L. Genzel. Optical conductivity of BCS superconductors with arbitrary purity. *Physica C: Superconductivity*, 183(1-3):99 – 104, 1991.

[67] L. Degiorgi, E. J. Nicol, O. Klein, G. Grüner, P. Wachter, S.-M. Huang, J. Wiley, and R. B. Kaner. Optical properties of the alkali-metal-doped superconducting fullerenes: K_3C_{60} and Rb_3C_{60}. *Phys. Rev. B*, 49(10):7012–7025, Mar 1994.

[68] A. V. Puchkov, T. Timusk, W. D. Mosley, and R. N. Shelton. Optical study of $Ba_{0.6}K_{0.4}BiO_3$ single crystals: Normal and superconducting properties. *Phys. Rev. B*, 50(6):4144–4153, Aug 1994.

[69] K. Kamarás, S. L. Herr, C. D. Porter, N. Tache, D. B. Tanner, S. Etemad, T. Venkatesan, E. Chase, A. Inam, X. D. Wu, M. S. Hegde, and B. Dutta. In a clean high-T_c superconductor you do not see the gap. *Phys. Rev. Lett.*, 64:84–87, Jan 1990.

[70] A. Zimmers, R. P. S. M. Lobo, N. Bontemps, C. C. Homes, M. C. Barr, Y. Dagan, and R. L. Greene. Infrared signature of the superconducting state in $Pr_{2-x}Ce_xCuO_4$. *Phys. Rev. B*, 70(13):132502, Oct 2004.

[71] C. C. Homes, R. P. S. M. Lobo, P. Fournier, A. Zimmers, and R. L. Greene. Optical determination of the superconducting energy gap in electron-doped $Pr_{1.85}Ce_{0.15}CuO_4$. *Phys. Rev. B*, 74(21):214515, Dec 2006.

[72] Robert A. Kaindl, Marc A. Carnahan, Joseph Orenstein, Daniel S. Chemla, Hans M. Christen, Hong-Ying Zhai, Mariappan Paranthaman, and Doug H. Lowndes. Far-Infrared Optical Conductivity Gap in Superconducting MgB_2 Films. *Phys. Rev. Lett.*, 88:027003, Dec 2001.

[73] A. Pimenov, A. Loidl, and S. I. Krasnosvobodtsev. Superconducting energy gap in a MgB_2 film observed by infrared reflectance. *Phys. Rev. B*, 65:172502, Apr 2002.

[74] A. Perucchi, L. Degiorgi, J. Jun, M. Angst, and J. Karpinski. Magneto-Optical Study of the Superconducting Gap of MgB_2 Single Crystals. *Phys. Rev. Lett.*, 89:097001, Aug 2002.

[75] G. Li, W. Z. Hu, J. Dong, Z. Li, P. Zheng, G. F. Chen, J. L. Luo, and N. L. Wang. Probing the Superconducting Energy Gap from Infrared Spectroscopy on a $Ba_{0.6}K_{0.4}Fe_2As_2$ Single Crystal with $T_c = 37$ K. *Phys. Rev. Lett.*, 101(10):107004, Sep 2008.

[76] R. P. S. M. Lobo, Y. M. Dai, U. Nagel, T. Rõ om, J. P. Carbotte, T. Timusk, A. Forget, and D. Colson. Optical signature of subgap absorption in the superconducting state of $Ba(Fe_{1-x}Co_x)_2As_2$. *Phys. Rev. B*, 82(10):100506, Sep 2010.

[77] K. W. Kim, M. Rössle, A. Dubroka, V. K. Malik, T. Wolf, and C. Bernhard. Evidence for multiple superconducting gaps in optimally doped $BaFe_{1.87}Co_{0.13}As_2$ from infrared spectroscopy. *Phys. Rev. B*, 81(21):214508, Jun 2010.

[78] A. Akrap, J. J. Tu, L. J. Li, G. H. Cao, Z. A. Xu, and C. C. Homes. Infrared phonon anomaly in $BaFe_2As_2$. *Phys. Rev. B*, 80(18):180502, Nov 2009.

[79] J. J. Tu, J. Li, W. Liu, A. Punnoose, Y. Gong, Y. H. Ren, L. J. Li, G. H. Cao, Z. A. Xu, and C. C. Homes. Optical properties of the iron arsenic superconductor $BaFe_{1.85}Co_{0.15}As_2$. *Phys. Rev. B*, 82(17):174509, Nov 2010.

[80] C. C. Homes, A. Akrap, J. S. Wen, Z. J. Xu, Z. W. Lin, Q. Li, and G. D. Gu. Electronic correlations and unusual superconducting response in the optical properties of the iron chalcogenide $FeTe_{0.55}Se_{0.45}$. *Phys. Rev. B*, 81(18):180508, May 2010.

[81] E. van Heumen, Y. Huang, S. de Jong, A. B. Kuzmenko, M. S. Golden, and D. van der Marel. Optical properties of $BaFe_{2-x}Co_xAs_2$. *EPL (Europhysics Letters)*, 90(3):37005, 2010.

[82] B. Cheng, Z. G. Chen, C. L. Zhang, R. H. Ruan, T. Dong, B. F. Hu, W. T. Guo, S. S. Miao, P. Zheng, J. L. Luo, G. Xu, Pengcheng Dai, and N. L. Wang. Three-dimensionality of band structure and a large residual quasiparticle population in $Ba_{0.67}K_{0.33}Fe_2As_2$ as revealed by *c*-axis polarized optical measurements. *Phys. Rev. B*, 83(14):144522, Apr 2011.

[83] B. Gorshunov, D. Wu, A. A. Voronkov, P. Kallina, K. Iida, S. Haindl, F. Kurth, L. Schultz, B. Holzapfel, and M. Dressel. Direct observation of the superconducting energy gap in the optical conductivity of the iron pnictide superconductor $Ba(Fe_{0.9}Co_{0.1})_2As_2$. *Phys. Rev. B*, 81(6):060509, Feb 2010.

[84] D. Wu, N. Barišić, M. Dressel, G. H. Cao, Z. A. Xu, J. P. Carbotte, and E. Schachinger. Nodes in the order parameter of superconducting iron pnictides investigated by infrared spectroscopy. *Phys. Rev. B*, 82(18):184527, Nov 2010.

[85] D. Wu, N. Barišić, P. Kallina, A. Faridian, B. Gorshunov, N. Drichko, L. J. Li, X. Lin, G. H. Cao, Z. A. Xu, N. L. Wang, and M. Dressel. Optical investigations of the normal and superconducting states reveal two electronic subsystems in iron pnictides. *Phys. Rev. B*, 81(10):100512, Mar 2010.

[86] D. Wu, N. Barišić, M. Dressel, G. H. Cao, Z-A. Xu, E. Schachinger, and J. P. Carbotte. Eliashberg analysis of optical spectra reveals a strong coupling of charge carriers to spin fluctuations in doped iron-pnictide $BaFe_2As_2$ superconductors. *Phys. Rev. B*, 82(14):144519, Oct 2010.

[87] D. Wu, G. Chanda, H. S. Jeevan, P. Gegenwart, and M. Dressel. Optical investigations of chemically pressurized $EuFe_2(As_{1-x}P_x)_2$: An *s*-wave superconductor with strong interband interactions. *Phys. Rev. B*, 83(10):100503, Mar 2011.

[88] E. G. Maksimov, A. E. Karakozov, B. P. Gorshunov, A. S. Prokhorov, A. A. Voronkov, E. S. Zhukova, V. S. Nozdrin, S. S. Zhukov, D. Wu, M. Dressel, S. Haindl, K. Iida, and B. Holzapfel. Two-band Bardeen-Cooper-Schrieffer superconducting state of the iron pnictide compound $Ba(Fe_{0.9}Co_{0.1})_2As_2$. *Phys. Rev. B*, 83(14):140502, Apr 2011.

[89] M. Nakajima, S. Ishida, K. Kihou, Y. Tomioka, T. Ito, Y. Yoshida, C. H. Lee, H. Kito, A. Iyo, H. Eisaki, K. M. Kojima, and S. Uchida. Evolution of the optical spectrum with doping in $Ba(Fe_{1-x}Co_x)_2As_2$. *Phys. Rev. B*, 81(10):104528, Mar 2010.

[90] J. Yang, D. Hüvonen, U. Nagel, T. Rõ om, N. Ni, P. C. Canfield, S. L. Bud'ko, J. P. Carbotte, and T. Timusk. Optical Spectroscopy of Superconducting $Ba_{0.55}K_{0.45}Fe_2As_2$: Evidence for Strong Coupling to Low-Energy Bosons. *Phys. Rev. Lett.*, 102(18):187003, May 2009.

[91] A. Charnukha, P. Popovich, Y. Matiks, D. L. Sun, C. T. Lin, A. N. Yaresko, B. Keimer, and A. V. Boris. Superconductivity-induced optical anomaly in an iron arsenide. *Nat Commun*, 2:219, March 2011.

[92] A. V. Boris, N. N. Kovaleva, S. S. A. Seo, J. S. Kim, P. Popovich, Y. Matiks, R. K. Kremer, and B. Keimer. Signatures of Electronic Correlations in Optical Properties of $LaFeAsO_{1-x}F_x$. *Phys. Rev. Lett.*, 102(2):027001, Jan 2009.

[93] Hiroki Takahashi, Kazumi Igawa, Kazunobu Arii, Yoichi Kamihara, Masahiro Hirano, and Hideo Hosono. Superconductivity at 43 K in an iron-based layered compound $LaO_{1-x}F_xFeAs$. *Nature*, 453(7193):376–378, May 2008.

[94] Ren Zhi-An, Lu Wei, Yang Jie, Yi Wei, Shen Xiao-Li, Zheng-Cai, Che Guang-Can, Dong Xiao-Li, Sun Li-Ling, Zhou Fang, and Zhao Zhong-Xian. Superconductivity at 55 K in Iron-Based F-Doped Layered Quaternary Compound $Sm[O_{1-x}F_x]FeAs$. *Chinese Physics Letters*, 25(6):2215, 2008.

[95] Marianne Rotter, Marcus Tegel, and Dirk Johrendt. Superconductivity at 38 K in the Iron Arsenide $Ba_{1-x}K_xFe_2As_2$. *Phys. Rev. Lett.*, 101(10):107006, Sep 2008.

[96] Athena S. Sefat, Rongying Jin, Michael A. McGuire, Brian C. Sales, David J. Singh, and David Mandrus. Superconductivity at 22 K in Co-Doped $BaFe_2As_2$ Crystals. *Phys. Rev. Lett.*, 101(11):117004, Sep 2008.

[97] Joshua H. Tapp, Zhongjia Tang, Bing Lv, Kalyan Sasmal, Bernd Lorenz, Paul C. W. Chu, and Arnold M. Guloy. LiFeAs: An intrinsic FeAs-based superconductor with $T_c = 18$ K . *Phys. Rev. B*, 78(6):060505, Aug 2008.

[98] Dinah R. Parker, Michael J. Pitcher, Peter J. Baker, Isabel Franke, Tom Lancaster, Stephen J. Blundell, and Simon J. Clarke. Structure, antiferromagnetism and superconductivity of the layered iron arsenide NaFeAs. *Chem. Commun.*, 16(16):2189–2191, 2009.

[99] Xiyu Zhu, Fei Han, Gang Mu, Bin Zeng, Peng Cheng, Bing Shen, and Hai-Hu Wen. $Sr_3Sc_2Fe_2As_2O_5$ as a possible parent compound for FeAs-based superconductors. *Phys. Rev. B*, 79:024516, Jan 2009.

[100] Xiyu Zhu, Fei Han, Gang Mu, Peng Cheng, Bing Shen, Bin Zeng, and Hai-Hu Wen. Transition of stoichiometric Sr_2VO_3FeAs to a superconducting state at 37.2 K. *Phys. Rev. B*, 79(22):220512, Jun 2009.

[101] C. W. Chu. High-temperature superconductivity: Alive and kicking. *Nat Phys*, 5(11):787–789, November 2009.

[102] Marianne Rotter, Marcus Tegel, Dirk Johrendt, Inga Schellenberg, Wilfried Hermes, and Rainer Pöttgen. Spin-density-wave anomaly at 140 K in the ternary iron arsenide $BaFe_2As_2$. *Phys. Rev. B*, 78(2):020503, Jul 2008.

[103] D. J. Singh. Electronic structure and doping in $BaFe_2As_2$ and LiFeAs: Density functional calculations. *Phys. Rev. B*, 78(9):094511, Sep 2008.

[104] Gang Xu, Haijun Zhang, Xi Dai, and Zhong Fang. Electron-hole asymmetry and quantum critical point in hole-doped $BaFe_2As_2$. *EPL (Europhysics Letters)*, 84(6):67015, 2008.

[105] M.V. Sadovskii. High ‐ Temperature Superconductivity in Iron Based Layered Compounds. *arXiv*, 0812:0302v1, 2008.

[106] Bing Shen, Huan Yang, Zhao-Sheng Wang, Fei Han, Bin Zeng, Lei Shan, Cong Ren, and Hai-Hu Wen. Transport properties and asymmetric scattering in $Ba_{1-x}K_xFe_2As_2$ single crystals compared to the electron doped counterparts $Ba(Fe_{1-x}Co_x)_2As_2$. *arXiv*, 1106:4256v1, 2011.

[107] L J Li, Y K Luo, Q B Wang, H Chen, Z Ren, Q Tao, Y K Li, X Lin, M He, Z W Zhu, G H Cao, and Z A Xu. Superconductivity induced by Ni doping in $BaFe_2As_2$ single crystals. *New Journal of Physics*, 11(2):025008, 2009.

[108] J. T. Park, D. S. Inosov, Ch. Niedermayer, G. L. Sun, D. Haug, N. B. Christensen, R. Dinnebier, A. V. Boris, A. J. Drew, L. Schulz, T. Shapoval, U. Wolff, V. Neu, Xiaoping Yang, C. T. Lin, B. Keimer, and V. Hinkov. Electronic Phase Separation in the Slightly Underdoped Iron Pnictide Superconductor $Ba_{1-x}K_xFe_2As_2$. *Phys. Rev. Lett.*, 102(11):117006, Mar 2009.

[109] T. Goko, A. A. Aczel, E. Baggio-Saitovitch, S. L. Bud'ko, P. C. Canfield, J. P. Carlo, G. F. Chen, Pengcheng Dai, A. C. Hamann, W. Z. Hu, H. Kageyama, G. M. Luke, J. L. Luo, B. Nachumi, N. Ni, D. Reznik, D. R. Sanchez-Candela, A. T. Savici, K. J. Sikes, N. L. Wang, C. R. Wiebe, T. J. Williams, T. Yamamoto, W. Yu, and Y. J. Uemura. Superconducting state coexisting with a phase-separated static magnetic order in $(Ba,K)Fe_2As_2$, $(Sr,Na)Fe_2As_2$, and $CaFe_2As_2$. *Phys. Rev. B*, 80(2):024508, Jul 2009.

[110] A. A. Aczel, E. Baggio-Saitovitch, S. L. Budko, P. C. Canfield, J. P. Carlo, G. F. Chen, Pengcheng Dai, T. Goko, W. Z. Hu, G. M. Luke, J. L. Luo, N. Ni, D. R. Sanchez-Candela, F. F. Tafti, N. L. Wang, T. J. Williams, W. Yu, and Y. J. Uemura. Muon-spin-relaxation studies of magnetic or-

der and superfluid density in antiferromagnetic NdFeAsO, $BaFe_2As_2$, and superconducting $Ba_{1-x}K_xFe_2As_2$. *Phys. Rev. B*, 78(21):214503, Dec 2008.

[111] F. Massee, Y. Huang, R. Huisman, S. de Jong, J. B. Goedkoop, and M. S. Golden. Nanoscale superconducting-gap variations and lack of phase separation in optimally doped $BaFe_{1.86}Co_{0.14}As_2$. *Phys. Rev. B*, 79(22):220517, Jun 2009.

[112] M.-H. Julien, H. Mayaffre, M. Horvatić, C. Berthier, X. D. Zhang, W. Wu, G. F. Chen, N. L. Wang, and J. L. Luo. Homogeneous vs. inhomogeneous coexistence of magnetic order and superconductivity probed by NMR in Co- and K-doped iron pnictides. *EPL (Europhysics Letters)*, 87(3):37001, 2009.

[113] B. J. Arnold, S. Kasahara, A. I. Coldea, T. Terashima, Y. Matsuda, T. Shibauchi, and A. Carrington. Nesting of electron and hole Fermi surfaces in nonsuperconducting $BaFe_2P_2$. *Phys. Rev. B*, 83:220504, Jun 2011.

[114] H. Shishido, A. F. Bangura, A. I. Coldea, S. Tonegawa, K. Hashimoto, S. Kasahara, P. M. C. Rourke, H. Ikeda, T. Terashima, R. Settai, Y. Ōnuki, D. Vignolles, C. Proust, B. Vignolle, A. McCollam, Y. Matsuda, T. Shibauchi, and A. Carrington. Evolution of the Fermi Surface of $BaFe_2(As_{1-x}\mathbf{P}_x)_2$ on Entering the Superconducting Dome. *Phys. Rev. Lett.*, 104:057008, Feb 2010.

[115] J. G. Analytis, C. M. J. Andrew, A. I. Coldea, A. McCollam, J.-H. Chu, R. D. McDonald, I. R. Fisher, and A. Carrington. Fermi Surface of $SrFe_2\mathbf{P}_2$ Determined by the de Haas˘van Alphen Effect. *Phys. Rev. Lett.*, 103:076401, Aug 2009.

[116] F. Rullier-Albenque, D. Colson, A. Forget, P. Thuéry, and S. Poissonnet. Hole and electron contributions to the transport properties of $Ba(Fe_{1-x}Ru_x)_2As_2$ single crystals. *Phys. Rev. B*, 81:224503, Jun 2010.

[117] F. Rullier-Albenque, D. Colson, A. Forget, and H. Alloul. Hall Effect and Resistivity Study of the Magnetic Transition, Carrier Content, and Fermi-Liquid Behavior in $Ba(Fe_{1-x}Co_x)_2As_2$. *Phys. Rev. Lett.*, 103:057001, Jul 2009.

[118] H. Ding, P. Richard, K. Nakayama, K. Sugawara, T. Arakane, Y. Sekiba, A. Takayama, S. Souma, T. Sato, T. Takahashi, Z. Wang, X. Dai, Z. Fang, G. F. Chen, J. L. Luo, and N. L. Wang. Observation of Fermi-surface-dependent nodeless superconducting gaps in $Ba_{0.6}K_{0.4}Fe_2As_2$. *EPL (Europhysics Letters)*, 83(4):47001, 2008.

[119] Cong Ren, Zhao-Sheng Wang, Hui-Qian Luo, Huan Yang, Lei Shan, and Hai-Hu Wen. Evidence for Two Energy Gaps in Superconducting $Ba_{0.6}K_{0.4}Fe_2As_2$ Single Crystals and the Breakdown of the Uemura Plot. *Phys. Rev. Lett.*, 101(25):257006, Dec 2008.

[120] K. Terashima, Y. Sekiba, J. H. Bowen, K. Nakayama, T. Kawahara, T. Sato, P. Richard, Y. M. Xu, L. J. Li, G. H. Cao, Z. A. Xu, H. Ding, and T. Takahashi. Fermi surface nesting induced strong pairing in iron-based superconductors. *Proc. Natl. Acad. Sci.*, 106:7330, 2009.

[121] M. L. Teague, G. K. Drayna, G. P. Lockhart, P. Cheng, B. Shen, H.-H. Wen, and N.-C. Yeh. Measurement of a Sign-Changing Two-Gap Superconducting Phase in Electron-Doped $Ba(Fe_{1-x}Co_x)_2As_2$ Single Crystals Using Scanning Tunneling Spectroscopy. *Phys. Rev. Lett.*, 106(8):087004, Feb 2011.

[122] Lei Shan, Yong-Lei Wang, Jing Gong, Bing Shen, Yan Huang, Huan Yang, Cong Ren, and Hai-Hu Wen. Evidence of multiple nodeless energy gaps in superconducting $Ba_{0.6}K_{0.4}Fe_2As_2$ single crystals from scanning tunneling spectroscopy. *Phys. Rev. B*, 83(6):060510, Feb 2011.

[123] X. G. Luo, M. A. Tanatar, J.-Ph. Reid, H. Shakeripour, N. Doiron-Leyraud, N. Ni, S. L. Bud'ko, P. C. Canfield, Huiqian Luo, Zhaosheng Wang, Hai-Hu Wen, R. Prozorov, and Louis Taillefer. Quasiparticle heat transport in

single-crystalline $Ba_{1-x}K_xFe_2As_2$: Evidence for a k -dependent superconducting gap without nodes. *Phys. Rev. B*, 80(14):140503, Oct 2009.

[124] J.-Ph. Reid, M. A. Tanatar, X. G. Luo, H. Shakeripour, N. Doiron-Leyraud, N. Ni, S. L. Bud'ko, P. C. Canfield, R. Prozorov, and Louis Taillefer. Nodes in the gap structure of the iron arsenide superconductor $Ba(Fe_{1-x}Co_x)_2As_2$ from c -axis heat transport measurements. *Phys. Rev. B*, 82(6):064501, Aug 2010.

[125] Gang Mu, Huiqian Luo, Zhaosheng Wang, Lei Shan, Cong Ren, and Hai-Hu Wen. Low temperature specific heat of the hole-doped $Ba_{0.6}K_{0.4}Fe_2As_2$ single crystals. *Phys. Rev. B*, 79(17):174501, May 2009.

[126] A. Charnukha, O. V. Dolgov, A. A. Golubov, Y. Matiks, D. L. Sun, C. T. Lin, B. Keimer, and A. V. Boris. Eliashberg approach to superconductivity-induced infrared anomalies in $Ba_{0.68}K_{0.32}Fe_2As_2$. *arXiv*, 1103:0938v1, 2011.

[127] A. D. Christianson, E. A. Goremychkin, R. Osborn, S. Rosenkranz, M. D. Lumsden, C. D. Malliakas, I. S. Todorov, H. Claus, D. Y. Chung, M. G. Kanatzidis, R. I. Bewley, and T. Guidi. Unconventional superconductivity in $Ba_{0.6}K_{0.4}Fe_2As_2$ from inelastic neutron scattering. *Nature*, 456(7224):930–932, December 2008.

[128] Christopher C. Homes, G. Lawrence Carr, Ricardo P. S. M. Lobo, Joseph D. LaVeigne, and David B. Tanner. Silicon beam splitter for far-infrared and terahertz spectroscopy. *Appl. Opt.*, 46(32):7884–7888, Nov 2007.

[129] Geoffry Evans, D. C. Schmadel, A. B. Sushkov, and H. D. Drew. Silicon beamsplitter for Fourier transform spectroscopy at far infrared frequencies. *arXiv*, 0706:4302v2, 2007.

[130] Christopher C. Homes, M. Reedyk, D. A. Cradles, and T. Timusk. Technique for measuring the reflectance of irregular, submillimeter-sized samples. *Applied Optics*, 32:2976, 1993.

[131] Huiqian Luo, Zhaosheng Wang, Huan Yang, Peng Cheng, Xiyu Zhu, and Hai-Hu Wen. Growth and characterization of $A_{1-x}K_xFe_2As_2$ (A = Ba, Sr) single crystals with x = 0 ‑ 0.4. *Superconductor Science and Technology*, 21(12):125014, 2008.

[132] A. F. Kemper, M. M. Korshunov, T. P. Devereaux, J. N. Fry, H-P. Cheng, and P. J. Hirschfeld. Anisotropic quasiparticle lifetimes in Fe-based superconductors. *Phys. Rev. B*, 83:184516, May 2011.

[133] P. Richard, T. Sato, K. Nakayama, S. Souma, T. Takahashi, Y.-M. Xu, G. F. Chen, J. L. Luo, N. L. Wang, and H. Ding. Angle-Resolved Photoemission Spectroscopy of the Fe-Based $Ba_{0.6}K_{0.4}Fe_2As_2$ High Temperature Superconductor: Evidence for an Orbital Selective Electron-Mode Coupling. *Phys. Rev. Lett.*, 102(4):047003, Jan 2009.

[134] R. Akis, J. P. Carbotte, and T. Timusk. Superconducting optical conductivity for arbitrary temperature and mean free path. *Phys. Rev. B*, 43(16):12804–12808, Jun 1991.

[135] K. Nakayama, T. Sato, P. Richard, Y.-M. Xu, Y. Sekiba, S. Souma, G. F. Chen, J. L. Luo, N. L. Wang, H. Ding, and T. Takahashi. Superconducting gap symmetry of $Ba_{0.6}K_{0.4}Fe_2As_2$ studied by angle-resolved photoemission spectroscopy. *EPL (Europhysics Letters)*, 85(6):67002, 2009.

[136] P. Szabó, Z. Pribulová, G. Pristáš, S. L. Bud'ko, P. C. Canfield, and P. Samuely. Evidence for two-gap superconductivity in $Ba_{0.55}K_{0.45}Fe_2As_2$ from directional point-contact Andreev-reflection spectroscopy. *Phys. Rev. B*, 79(1):012503, Jan 2009.

[137] P. Popovich, A. V. Boris, O. V. Dolgov, A. A. Golubov, D. L. Sun, C. T. Lin, R. K. Kremer, and B. Keimer. Specific Heat Measurements of $Ba_{0.68}K_{0.32}Fe_2As_2$ Single Crystals: Evidence for a Multiband Strong-Coupling Superconducting State. *Phys. Rev. Lett.*, 105(2):027003, Jul 2010.

[138] X. H. Zheng and D. G. Walmsley. Temperature-dependent gap edge in strong-coupling superconductors determined using the Eliashberg-Nambu formalism. *Phys. Rev. B*, 77(10):104510, Mar 2008.

[139] F. Carbone, A. B. Kuzmenko, H. J. A. Molegraaf, E. van Heumen, E. Giannini, and D. van der Marel. In-plane optical spectral weight transfer in optimally doped $Bi_2Sr_2Ca_2Cu_3O_{10}$. *Phys. Rev. B*, 74(2):024502, Jul 2006.

[140] J Hwang, T Timusk, and G D Gu. Doping dependent optical properties of $Bi_2Sr_2CaCu_2O_{8+\delta}$. *Journal of Physics: Condensed Matter*, 19(12):125208, 2007.

[141] R. E. Glover and M. Tinkham. Transmission of Superconducting Films at Millimeter-Microwave and Far Infrared Frequencies. *Phys. Rev.*, 104(3):844–845, Nov 1956.

[142] M. V. Klein and G. Blumberg. Effective Mass and Color Change. *Science*, 283(5398):42–43, 1999.

[143] H. J. A. Molegraaf, C. Presura, D. van der Marel, P. H. Kes, and M. Li. Superconductivity-Induced Transfer of In-Plane Spectral Weight in $Bi_2Sr_2CaCu_2O_{8+\delta}$. *Science*, 295(5563):2239–2241, 2002.

[144] A. F. Santander-Syro, R. P. S. M. Lobo, N. Bontemps, Z. Konstantinovic, Z. Z. Li, and H. Raffy. Pairing in cuprates from high-energy electronic states. *EPL (Europhysics Letters)*, 62(4):568, 2003.

[145] F. Carbone, A. B. Kuzmenko, H. J. A. Molegraaf, E. van Heumen, V. Lukovac, F. Marsiglio, D. van der Marel, K. Haule, G. Kotliar, H. Berger, S. Courjault, P. H. Kes, and M. Li. Doping dependence of the redistribution of optical spectral weight in $Bi_2Sr_2CaCu_2O_{8+\delta}$. *Phys. Rev. B*, 74(6):064510, Aug 2006.

[146] S. V. Dordevic, E. J. Singley, D. N. Basov, Seiki Komiya, Yoichi Ando, E. Bucher, C. C. Homes, and M. Strongin. Global trends in the interplane

penetration depth of layered superconductors. *Phys. Rev. B*, 65(13):134511, Mar 2002.

[147] T. Fischer, A. V. Pronin, J. Wosnitza, K. Iida, F. Kurth, S. Haindl, L. Schultz, B. Holzapfel, and E. Schachinger. Highly anisotropic energy gap in superconducting $Ba(Fe_{0.9}Co_{0.1})_2As_2$ from optical conductivity measurements. *Phys. Rev. B*, 82(22):224507, Dec 2010.

[148] R. Valdés Aguilar, L. S. Bilbro, S. Lee, C. W. Bark, J. Jiang, J. D. Weiss, E. E. Hellstrom, D. C. Larbalestier, C. B. Eom, and N. P. Armitage. Pair-breaking effects and coherence peak in the terahertz conductivity of superconducting $BaFe_{2-2x}Co_{2x}As_2$ thin films. *Phys. Rev. B*, 82(18):180514, Nov 2010.

[149] V. Mishra, G. Boyd, S. Graser, T. Maier, P. J. Hirschfeld, and D. J. Scalapino. Lifting of nodes by disorder in extended-s-state superconductors: Application to ferropnictides. *Phys. Rev. B*, 79:094512, Mar 2009.

[150] J. P. Carbotte and E. Schachinger. Optical conductivity in ferropnictides with and without gap nodes. *Phys. Rev. B*, 81:104510, Mar 2010.

[151] B. Muschler, W. Prestel, R. Hackl, T. P. Devereaux, J. G. Analytis, Jiun-Haw Chu, and I. R. Fisher. Band- and momentum-dependent electron dynamics in superconducting $Ba(Fe_{1-x}Co_x)_2As_2$ as seen via electronic Raman scattering. *Phys. Rev. B*, 80:180510, Nov 2009.

[152] E. Schachinger and J. P. Carbotte. Quasiparticle density of states in superconducting alloys with localized states within the gap. *Phys. Rev. B*, 29:165–171, Jan 1984.

[153] A. B. Vorontsov, M. G. Vavilov, and A. V. Chubukov. Superfluid density and penetration depth in the iron pnictides. *Phys. Rev. B*, 79(14):140507, Apr 2009.

[154] E. J. Nicol and J. P. Carbotte. Effect of pair breaking on the optical conductivity in the clean limit. *Phys. Rev. B*, 45:10519–10526, May 1992.

[155] Gang MU, Bin ZENG, Peng CHENG, Zhao-Sheng WANG, Lei FANG, Bing SHEN, Lei SHAN, Cong REN, and Hai-Hu WEN. Sizable Residual Quasiparticle Density of States Induced by Impurity Scattering Effect in $Ba(Fe_{1-x}Co_x)_2As_2$ Single Crystals. *CHIN. PHYS. LETT.*, 27:037402, 2010.

[156] R. T. Gordon, H. Kim, M. A. Tanatar, R. Prozorov, and V. G. Kogan. London penetration depth and strong pair breaking in iron-based superconductors. *Phys. Rev. B*, 81:180501, May 2010.

[157] L. B. Ioffe and A. J. Millis. Superconductivity and the c Axis Spectral Weight of High-Tc Superconductors. *Science*, 285(5431):1241–1244, 1999.

[158] L. B. Ioffe and A. J. Millis. Quantum fluctuations and the c-axis optical conductivity of high-T_c superconductors. *Phys. Rev. B*, 61(13):9077–9087, Apr 2000.

Publications

[1] M. Li, Z. C. Wen, J. X. Fu, X. Fang, **Y. M. Dai**, R. J. Liu, X. F. Han and X. G. Qiu. Composite metamaterials with dual-band magnetic resonances in the terahertz frequency regime. Journal of Physics D - Applied Physics 42, 115420 (2009)

[2] R. P. S. M. Lobo, **Y. M. Dai**, U. Nagel, T. Rõõm, J. P. Carbotte, T. Timusk, A. Forget and D. Colson. Optical signature of subgap absorption in the superconducting state of $Ba(Fe_{1-x}Co_x)_2As_2$. Phys. Rev. B 82, 100506(R), (2010)

[3] **Y. M. Dai**, B. Xu, B. Shen, H. H. Wen, X. G. Qiu and R. P. S. M. Lobo. Effects of in-plane and out-of-plane doping in the infrared conductivity gap of $BaFe_2As_2$ superconductors. (Submitted 2011)

[4] **Y. M. Dai**, B. Xu, P. Cheng, H. Q. Luo, H. H. Wen, X. G. Qiu and R. P. S. M. Lobo. Doping evolution of the optical scattering rate and effective mass of $Bi_2Sr_{2-x}La_xCuO_6$. (Submitted 2011)

[5] **Y. M. Dai**, B. Xu, B. Shen, H. H. Wen, X. G. Qiu and R. P. S. M. Lobo. Observation of a pseudogap in the optical conductivity of underdoped $Ba_{1-x}K_xFe_2As_2$. (Submitted 2012)

[6] **Y. M. Dai**, B. Xu, B. Shen, H. H. Wen, X. G. Qiu and R. P. S. M. Lobo. A hidden non Fermi liquid behavior in $Ba_{0.6}K_{0.4}Fe_2As_2$ as revealed by optical spectroscopy. (in preparation)

[7] **Y. M. Dai**, B. Xu, B. Shen, H. H. Wen, X. G. Qiu and R. P. S. M. Lobo. Temperature dependence of the optical spectral spectrum and spectral weight redistribution in $Ba_{0.6}K_{0.4}Fe_2As_2$. (in preparation)

[8] **Y. M. Dai**, A. Forget, D. Colson, X. G. Qiu and R. P. S. M. Lobo. The doping evolution of the spin density wave of $Ba(Fe_{1-x}Co_x)_2As_2$ probed by optical spectroscopy. (in preparation)

[9] **Y. M. Dai**, B. Xu, P. Cheng, H. Q. Luo, H. H. Wen, X. G. Qiu and R. P. S. M. Lobo. Optical phase diagram of single layered cuprate Bi2201: the evolution of the optical conductivity from the pseudo-gap state to a Fermi liquid. (in preparation)